Introduction to special section on Recent Advances in the Study of Optical Variability in the Near-Surface and Upper Ocean

Introduction to special section on Recent Advances in the Study of Optical Variability in the Near-Surface and Upper Ocean

T. Dickey,[1] M. L. Banner,[2,3] P. Bhandari,[4] T. Boyd,[5,6] L. Carvalho,[7] G. Chang,[8] Y. Chao,[9] H. Czerski,[10] M. Darecki,[11] C. Dong,[12] D. Farmer,[13] S. Freeman,[14] J. Gemmrich,[15] P. Gernez,[16] N. Hall-Patch,[17] B. Holt,[18] S. Jiang,[1] C. Jones,[19] G. Kattawar,[20] D. LeBel,[21] L. Lenain,[22] M. Lewis,[23] Y. Liu,[24] L. Logan,[25] D. Manov,[1] W. K. Melville,[22] M. A. Moline,[26] R. Morison,[3] F. Nencioli,[27] W. S. Pegau,[28] B. Reineman,[22] I. Robbins,[26] R. Röttgers,[29] H. Schultz,[30] L. Shen,[31] M. Shinki,[32] M. Slivkoff,[33] M. Sokólski,[11] F. Spada,[8] N. Statom,[22,34] D. Stramski,[35] P. Sutherland,[22] M. Twardowski,[36] S. Vagle,[17] R. Van Dommelen,[37] K. Voss,[4] L. Washburn,[38] J. Wei,[23] H. Wijesekera,[39] O. Wurl,[40] D. Yang,[31] S. Yildiz,[35] Y. You,[20,41] D. K. P. Yue,[42] R. Zaneveld,[43] and C. J. Zappa[21]

Received 7 February 2012; revised 18 April 2012; accepted 20 April 2012; published 30 June 2012.

[1] Optical variability occurs in the near-surface and upper ocean on very short time and space scales (e.g., milliseconds and millimeters and less) as well as greater scales. This variability is caused by solar, meteorological, and other physical forcing as well as biological and chemical processes that affect optical properties and their distributions, which in turn control the propagation of light across the air-sea interface and within the

[1]Ocean Physics Laboratory, Department of Geography, University of California, Santa Barbara, California, USA.
[2]ISDGM, Venice, Italy.
[3]School of Mathematics and Statistics, University of New South Wales, Sydney, Australia.
[4]Department of Physics, University of Miami, Coral Gables, Florida, USA.
[5]College of Oceanic and Atmospheric Sciences, Oregon State University, Corvallis, Oregon, USA.
[6]Now at Scottish Association for Marine Science, Scottish Marine Institute, Oban, UK.
[7]Department of Geography, University of California, Santa Barbara, California, USA.
[8]Sea Engineering, Santa Cruz, California, USA.
[9]Remote Sensing Solutions, Incorporated, Pasadena, California, USA.
[10]Institute of Sound and Vibration Research, University of Southampton, Southampton, UK.
[11]Institute of Oceanology, Polish Academy of Sciences, Sopot, Poland.
[12]IGPP, UCLA, Los Angeles, California, USA.
[13]Graduate School of Oceanography, University of Rhode Island, Narragansett, Rhode Island, USA.
[14]NASA Goddard Space Flight Space Center, Science Systems and Applications, Incorporated, Greenbelt, Maryland, USA.
[15]Physics and Astronomy, University of Victoria, Victoria, British Columbia, Canada.
[16]Mer Molécules, Facultés des Sciences et Techniques, Université de Nantes, Nantes, France.
[17]Institute of Ocean Sciences, Fisheries and Oceans Canada, Sidney, British Columbia, Canada.
[18]Jet Propulsion Laboratory, California Institute of Technology, Pasadena, California, USA.
[19]Earth Research Institute, University of California, Santa Barbara, California, USA.
[20]Department of Physics and Astronomy, Texas A&M University, College Station, Texas, USA.
[21]Lamont Doherty Earth Observatory, Columbia University, Palisades, New York, USA.
[22]Scripps Institution of Oceanography, University of California, San Diego, La Jolla, California, USA.
[23]Department of Oceanography, Dalhousie University, Halifax, Nova Scotia, Canada.
[24]Department of Mechanical Engineering, Center for Ocean Engineering, Massachusetts Institute of Technology, Cambridge, Massachusetts, USA.
[25]Physics Department, University of Miami, Miami, Florida, USA.
[26]Biological Sciences Department, California Polytechnic State University, San Luis Obispo, California, USA.
[27]Mediterranean Institute of Oceanography, Université d'Aix-Marseille, Marseille, France.
[28]Oil Spill Recovery Institute, Cordova, Arkansas, USA.
[29]Centre for Materials and Coastal Research, Helmholtz-Zentrum Geesthacht, Geesthacht, Germany.
[30]Department of Computer Science, University of Massachusetts, Amherst, Massachussets, USA.
[31]Department of Civil Engineering, Johns Hopkins University, Baltimore, Maryland, USA.
[32]CRI-Middleware, Tokyo, Japan.
[33]In-Situ Marine Optics P/L, Bibra Lake, Western Australia, Australia.
[34]Mechanical and Aerospace Engineering, University of California, San Diego, La Jolla, California, USA.
[35]Marine Physical Laboratory, Scripps Institution of Oceanography, University of California, San Diego, La Jolla, California, USA.
[36]WET Labs, Incorporated, Narragansett, Rhode Island, USA.
[37]Satlantic LP, Halifax, Nova Scotia, Canada.
[38]Marine Science Institute and Department of Geography, University of California, Santa Barbara, California, USA.
[39]Naval Research Laboratory, Stennis Space Center, Mississippi, USA.
[40]Department of Ocean, Earth and Atmospheric Sciences, Old Dominion University, Norfolk, Virginia, USA.
[41]Now at WesternGeco, Houston, Texas, USA.
[42]Massachusetts Institute of Technology, Cambridge, Massachusetts, USA.
[43]WET Labs, Incorporated, Philomath, Oregon, USA.

Corresponding author: T. Dickey, Ocean Physics Laboratory, Department of Geography, University of California, Santa Barbara, CA 93106, USA. (tommy.dickey@opl.ucsb.edu)

0148-0227/12/2012JC007964

upper ocean. Recent developments in several technologies and modeling capabilities have enabled the investigation of a variety of fundamental and applied problems related to upper ocean physics, chemistry, and light propagation and utilization in the dynamic near-surface ocean. The purpose here is to provide background for and an introduction to a collection of papers devoted to new technologies and observational results as well as model simulations, which are facilitating new insights into optical variability and light propagation in the ocean as they are affected by changing atmospheric and oceanic conditions.

Citation: Dickey, T., et al. (2012), Introduction to special section on Recent Advances in the Study of Optical Variability in the Near-Surface and Upper Ocean, *J. Geophys. Res.*, *117*, C00H20, doi:10.1029/2012JC007964.

1. Introduction

[2] Many of the papers in this special section were stimulated by research conducted during the Radiance in a Dynamic Ocean (RaDyO) program [*Dickey et al.*, 2011] while others are from related studies. One of the primary goals of RaDyO was to study the problem of underwater visibility and imaging of objects across the air-sea interface and of objects residing within the upper ocean as affected by a broad range of environmental conditions [e.g., *Duntley*, 1963; *Mullamaa*, 1975; *Preisendorfer*, 1976; *Davies-Colley*, 1988; *Schippnick*, 1988; *McLean and Freeman*, 1996; *Jaffe et al.*, 2001; *Zaneveld and Pegau*, 2003; *Dolin et al.*, 2006; *Doron et al.*, 2007; *Dolin and Luchinin*, 2008; *Levin et al.*, 2008]. This specific problem and other related problems, as described below, involve meteorological, physical, optical, biological, and chemical processes acting over time and space scales as short as milliseconds and millimeters. For example, atmospheric conditions involving clouds, fog, aerosols, and sun angle affect incident solar radiation impinging on the ocean's surface. The initial fate of the impinging light is controlled by the air-sea interface's topography, as modulated by surface capillary and gravity waves, and internal gravity waves [e.g., *Schenck*, 1957; *Snyder and Dera*, 1970; *Dera and Olszewski*, 1978; *Stramski and Dera*, 1988; *Dera*, 1992; *Dera and Stramski*, 1993; *McLean and Freeman*, 1996; *Stramska and Dickey*, 1998; *Zaneveld et al.*, 2001a, 2001b; *Wijesekera et al.*, 2005; *You et al.*, 2009, 2010], and as affected by the presence of surfactants [e.g., *Wurl et al.*, 2009] and bubbles [e.g., *Stramski*, 1994; *Zhang et al.*, 1998; *Stramski and Tegowski*, 2001; *Terrill et al.*, 2001; *Wolk et al.*, 2002; *Terrill and Lewis*, 2004; *Zhang et al.*, 2011]. Light propagation within and exiting the upper ocean is also affected by organisms, particulate and dissolved materials including colored dissolved organic matter, physical, chemical,and biological processes, inherent optical properties (IOPs), and apparent optical properties (AOPs) along with characteristics of the molecular and turbulent boundary layers on both sides of the air-sea interface. These layers are dynamic and affected by wind-forcing, waves, stratification, chemical and particulate composition of seawater, optical properties, bubbles, foam, and whitecaps (W. K. Melville et al., The impact of surface wave breaking on imaging through the ocean surface, manuscript in preparation, 2012).

[3] There are several other relevant problems that relate to this research and require similar data sets and modeling approaches. These include the fundamental problem of radiative transfer (e.g., light propagation across the air-sea interface and within the upper layer [e.g., *Kattawar et al.*, 1976; *Shifrin*, 1988; *Kattawar and Adams*, 1989; *Dera*, 1992; *Kirk*, 1994; *Mobley*, 1994; *Walker*, 1994; *Thomas and Stamnes*, 1999; *Zhai et al.*, 2008a, 2008b]); marine animal vision [e.g., *McFarland and Loew*, 1983], phytoplankton responses to fluctuating light fields [e.g., *Frechette and Legendre*, 1978; *Walsh and Legendre*, 1983; *Legendre et al.*, 1986; *Queguiner and Legendre*, 1986; *Stramski et al.*, 1993; *Kirk*, 1994], air-sea exchanges of momentum, heat, and gases [e.g., *Thorpe*, 1982; *Wanninkhof*, 1992; *Woolf*, 1997, 2005; *Weller et al.*, 1998; *Wanninkhof and McGillis*, 1999; *Wanninkhof et al.*, 2004; *Yu and Weller*, 2007; *Berry and Kent*, 2009; *Brooks et al.*, 2009], and the interpretation of radiometric data collected in the ocean from various platforms including imagers mounted on aircraft and satellites [e.g., *Fraser et al.*, 1980; *McLean and Freeman*, 1996; *Zaneveld et al.*, 2001a, 2001b; *Zibordi et al.*, 2004; *Twardowski et al.*, 2007a; *Zaneveld et al.*, 2005; *Lewis*, 2008; *Gernez and Antoine*, 2009].

[4] Fluctuations in the underwater light field caused by surface waves have been a subject of earlier theoretical and experimental research. The models of *Schenck* [1957] and *Snyder and Dera* [1970] identified mechanisms for producing flashing light, which are associated with fluctuations in sea surface topography, namely its elevation, surface slope, and surface curvature. These physical processes are highly complex and can invalidate simplifying assumptions; thus, the solution of the theoretical problem is challenging. Light fluctuations just beneath the ocean surface are most intense under sunny skies accompanied by relatively weak winds and low sea states when wave focusing of direct solar rays dominates. The intensity and high-frequency content of these fluctuations decrease rapidly with depth within the top several meters of the ocean [e.g., *Dera and Gordon*, 1968; *Snyder and Dera*, 1970; *Fraser et al.*, 1980; *Dera and Stramski*, 1986].

[5] Specially designed radiometers and sampling strategies are required to fully resolve the maximum focusing at near-surface depths (down to about 5–10 m in clear waters), because these effects are often characterized by the presence of light pulses of very high amplitude and short duration [*Dera and Olszewski*, 1978; *Dera and Stramski*, 1986; *Gernez et al.*, 2011; *Darecki et al.*, 2011]. Most experimental work on underwater light fluctuations to date has been best suited to examine weaker fluctuations of light that occur at depths below the top few meters of the ocean. At these depths, even under sunny conditions, the fluctuations in instantaneous irradiance generally do not exceed the mean

irradiance by more than 50%, and are often within 10–20% of the mean irradiance level. The book by *Walker* [1994] reviews early relevant studies, including several from the former Soviet Union. Examples of more recent work include *Stramska and Dickey* [1998] and *Gernez and Antoine* [2009], who noted that if skies are overcast and surface illumination is diffuse, underwater light fluctuations are weak throughout the entire water column [see also *Dera and Olszewski*, 1967; *Stramski et al.*, 1992]. These fluctuations consist primarily of low-frequency components due to surface displacements associated with significant surface waves and/or swell.

[6] Interacting processes necessitate novel methods and models for imaging and other applications. A major obstacle to this line of research has been the inability of sampling and computational methods and hardware to sufficiently resolve high temporal and spatial scale variabilities, which can have very large dynamic ranges (up to at least 6 to 8 orders of magnitude) for such a diverse set of physical and optical variables. Several previous studies have used instrumentation designed specifically to measure the fast fluctuations and associated strongest wave focusing effects occurring at near-surface depths under sunny conditions [*Dera and Olszewski*, 1978; *Dera and Stramski*, 1986; *Stramski*, 1986; *Dera and Stramski*, 1993]. However, this work has been mostly limited to a single light wavelength, typically selected for maximum transparency in water. Focusing has been found to be most pronounced under weak winds (2–5 m/s) and thus slightly undulating sea surfaces, clear atmospheres with low surface irradiance diffuseness of less than 40%, and relatively high sun elevation with solar zenith angle generally less than 40° [*Dera and Stramski*, 1986; *Stramski*, 1986]. Under such conditions, high-amplitude pulses of focused light, exceeding the mean level of irradiance by more than 50%, have been shown to occur at frequencies higher than 100 per minute at near-surface depths. These strong focusing events, referred to as light flashes, have short durations on the order of 10 ms. Reviews of general features of wave-induced light fluctuations are provided in papers by *Stramski et al.* [1992], *Gernez and Antoine* [2009], *Gernez et al.* [2011], and *Darecki et al.* [2011].

[7] Previous work on light fluctuations has been unable to include some of the more important physical variables in sufficient detail, especially wave characteristics. RaDyO researchers are beginning to report significant advances in terms of linking light fluctuations to surface waves, because specially designed instrumentation and experiments have been utilized recently to obtain relevant data sets for developing and parameterizing more realistic models that couple radiative transfer, surface waves, and other physical dynamics.

[8] It should be noted that there has been an increased awareness of the multiplicity of interdisciplinary processes that must be considered in studying problems such as optical variability of the ocean. For example, bubbles, which are ubiquitous in the world ocean, play important roles for a host of processes. The problem of estimating the number of bubbles and their size distributions is daunting. *MacIntyre* [1972] forwarded an estimate that some 10^{18} to 10^{20} white cap bubbles break (and form) per second over the world ocean. More recently, *Bird et al.* [2010] have suggested that the number of bubbles may be even greater based on their work on daughter bubble cascades (creations of toroidal rings of small bubbles upon rupture). The importance of bubbles for optics of the ocean has been recognized by a few investigators [e.g., *Stramski*, 1994; *Zhang et al.*, 1998; *Stramski and Tegowski*, 2001; *Terrill et al.*, 2001; *Terrill and Lewis*, 2004; *Zhang et al.*, 2011]. In fact, it has been suggested that a large portion of upwelled radiance from the ocean surface may be attributed to bubbles and that ocean color shifts (toward green wavelengths) can affect ocean remote sensing algorithms for chlorophyll *a* [e.g., *Zhang et al.*, 1998]. Bubble size distributions and organic coatings of bubbles play important roles as well [e.g., *Zhang et al.*, 1998; *Stramski and Tegowski*, 2001; *Zhang et al.*, 2011]. The recognition of the potential optical effects of bubbles has led to the development of new optical and acoustical instrumentation with the expressed purposes of quantifying bubble effects on light in the ocean; some of these are described in this special section [*Czerski et al.*, 2011; *Vagle et al.*, 2012; *Twardowski et al.*, 2012]. Importantly, overall sampling of ocean optical variability has been advanced by the utilization of multiple platforms [e.g., *Dickey and Bidigare*, 2005; *Dickey et al.*, 2006], which facilitate the concurrent collection of a plethora of interdisciplinary data sets on unprecedented time and space scales. The RaDyO program was also devoted to modeling optical variability of the surface boundary layer and upper ocean, likewise on unprecedented time and space scales. Some of this modeling work is introduced in section 5.

[9] This paper concludes by briefly introducing contributions to this special section categorically as follows: (1) observational papers based primarily on results from the RaDyO program, (2) modeling papers done in conjunction with RaDyO, and (3) papers relevant to the theme of the special section that were submitted by authors independently of RaDyO. Finally, interested readers are directed to a recent survey article by *Dickey et al.* [2011], which briefly provides historical, introductory, and summary information relevant to this special section.

2. Overview of the RaDyO Observational Program

2.1. Sites of RaDyO Observations

[10] Fulfillment of the objectives of RaDyO required that a wide range of environmental conditions be observed for the development of models that would be useful for diverse optical, meteorological, and physical situations [*Dickey et al.*, 2011]. The first RaDyO experiment was conducted using the Scripps Institution of Oceanography (SIO) pier 6–28 January 2008. This work was primarily intended to test new instrumentation in a setting with good access to shore-based technical support and to develop integration of the diverse methodologies. However, some scientific results have been produced from this experiment as well. The second experiment was conducted in the Santa Barbara Channel (SBC) during the period of September 3–25, 2008. This setting was selected because it was expected to provide a relatively benign wind-wave regime and easy access to shore since several new or prototype instrumentation systems were being utilized. The third and final RaDyO experiment took place south of the Big Island of Hawaii from 24 August

Figure 1. Photographs of the R/V *Kilo Moana*, *Lil KM*, R/P *FLIP*, *Odyssey* AUV, and *REMUS* AUV.

through September 15, 2009. This location was selected because of its climatologically high, persistent wind speeds and relatively large sea states, its optically clear waters, and its open ocean character with good access to the deep-water port of Honolulu. The specific area of operations, which lies in the North Equatorial Current (NEC), is characterized by relatively modest mesoscale eddy activity and minor island effects as compared with areas directly in the wind wake of the Hawaiian archipelago [e.g., see *Dickey et al.*, 2008]. The field experiments are described in more detail below and on the Website http://www.opl.ucsb.edu/radyo/.

2.2. Platforms

[11] The multifaceted, multiscale nature of RaDyO problems necessitated a multiple platform, multidisciplinary sampling approach as has been discussed in detail in earlier references. The primary platforms used for the RaDyO Santa Barbara Channel experiment included: R/P *FLIP*, R/V *Kilo Moana*, an *Odyssey* autonomous underwater vehicle (AUV) [*Moline et al.*, 2012] (Figure 1), a *REMUS* AUV [*Moline et al.*, 2005, 2007, 2010, 2012; *Robbins et al.*, 2006], and a surfactant skimmer called the *Lil KM* (Figure 1). Also, a small aircraft equipped with lidar instrumentation made measurements over the site [*Reineman et al.*, 2009]. Because of anticipated greater sea states, the *Odyssey* AUV and the *Lil KM* were not utilized and the *REMUS* AUV was deployed on only a limited basis for the Hawaiian experiment. In addition, satellite-deployed sensors were utilized to obtain wind, sea surface temperature, color, and surface roughness (SAR for Santa Barbara experiment only) data. The platforms used for the field experiments are briefly described below.

2.2.1. R/P *FLIP*

[12] R/P *FLIP* (Floating Instrument Platform, Figure 2), originally launched on 2 June 1962, was designed to be a highly stable platform for oceanographic research in the areas of acoustics, seismic waves, ocean waves, and marine biology [*Fisher and Spiess*, 1963]. However, it has since been used for a variety of meteorological, air-sea interaction, and physical oceanographic experiments [e.g., *Siegel and Dickey*, 1986; *Smith et al.*, 1987; *Pinkel et al.*, 1991; *Plueddemann et al.*, 1996; *Smith*, 1998; *Friehe et al.*, 2001; *Rainville and Pinkel*, 2006] and for optical measurements in 1982 [*Siegel and Dickey*, 1987; *Dickey*, 1991]. R/P *FLIP* is essentially a large manned spar buoy when oriented vertically (note that it is towed horizontally to experiment sites). R/P *FLIP* measures approximately 108 m in length with ~90 m of its hull extending below the water line when on station. The diameter of R/P *FLIP*'s hull is 6.5 m from the 49 to 91 m depth; the hull tapers to 4 m at the 20 m depth (see schematic in Figure 3 of *Fisher and Spiess* [1963]). This design allows R/P *FLIP*, in free drift mode, to be minimally responsive to wave motion (<10% of surface motion, resonant period is ~25 s and thus displaced away from the spectral window of greatest wave motion (about 5–18 s)) as documented by *Fisher and Spiess* [1963], *Rudnick* [1967], *Rudnick and Hasse* [1971], and *Smith and Rieder* [1997]. For example, in ten meter waves R/P *FLIP*'s total vertical motion has been recorded to be less than 1 m (see http://www.mpl.ucsd.edu/resources/flip.intro.html for a bibliography and details concerning R/P *FLIP*).

[13] For the Santa Barbara Channel RaDyO experiment, R/P *FLIP* (Figure 2a) was moored in place at 34.2053° N, 119.6288° W in water of 168 m depth using a 3-point mooring [e.g., see *Bronson*, 1971]. Some tilting of R/P *FLIP* was apparent due to currents and winds. These conditions were apparently accompanied by a measurable oscillation in R/P *FLIP*'s heading and depth with an approximately 2 min period. Instruments were deployed from R/P *FLIP*'s booms to minimize the influence of flow distortion and superstructure interference with measurement devices which were either profiled or deployed at or mounted at specific depths. Booms with trolleys were used to deploy instrumentation. Also, R/P *FLIP* necessarily discharged wastewaters periodically and the times of these discharges were noted for possible contamination of optical and chemical data sets. For

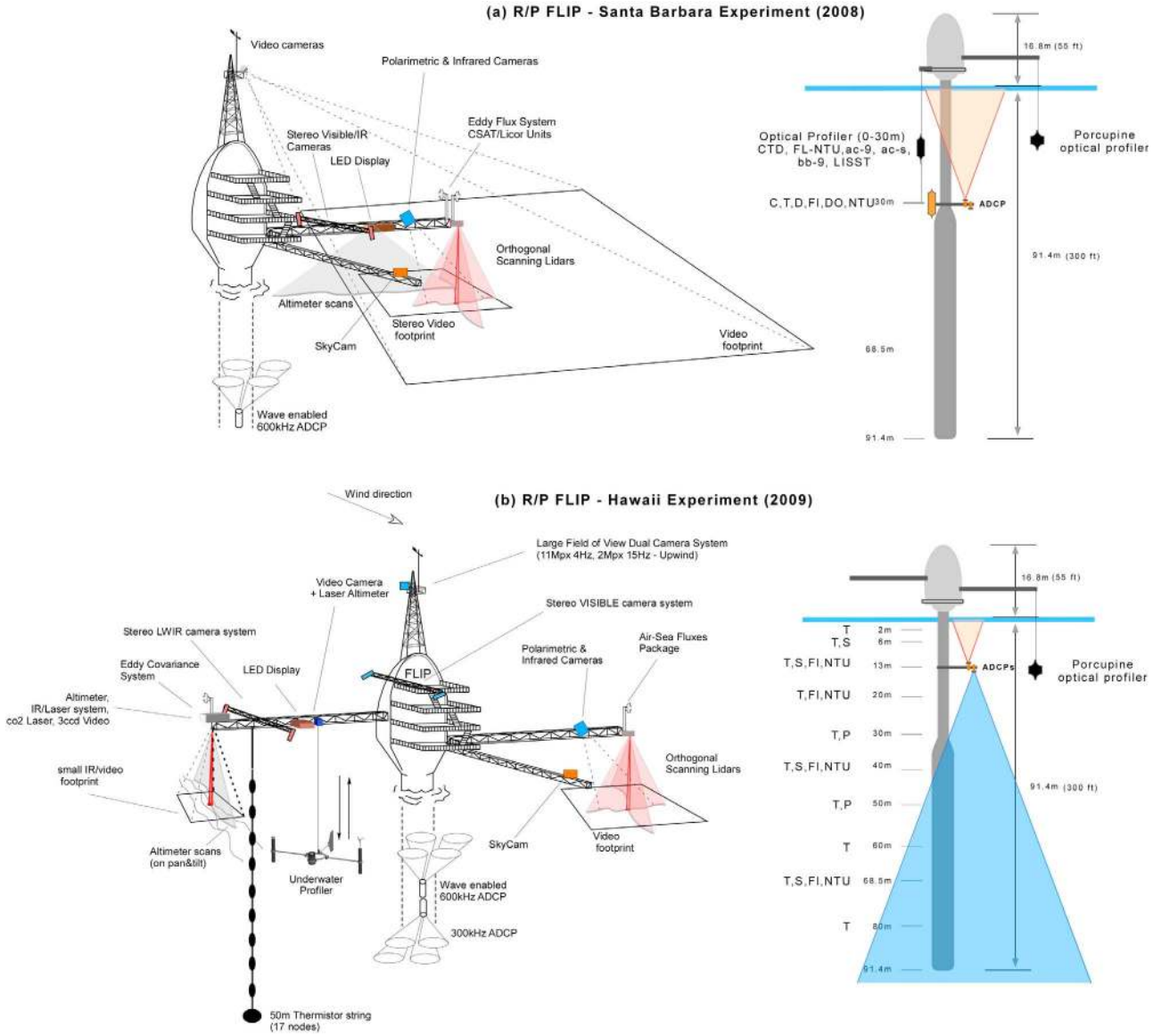

Figure 2. Instrumentation deployed on R/P *FLIP* during the (a) Santa Barbara and (b) Hawaii experiments in September 2008 and 2009, respectively. (c) R/P *FLIP* starboard boom during the Hawaii Experiment in September 2009. The air-sea flux package, orthogonal scanning laser altimeters, polarimetric and infrared cameras are shown in the upper right insert. The acoustic resonators and sonar float [*Vagle et al.*, 2012] are highlighted in the lower insert. (d) Corresponding instrumented R/P *FLIP* port boom, showing a suite of air-sea interaction and subsurface electro-optical sensors used to characterize the influence of breaking at the ocean surface on oceanic radiance and imaging (Melville et al., manuscript in preparation, 2012): eddy covariance meteorological system, stereo infrared and visible cameras, scanning and single-point laser altimeters, LED downward looking display for imaging through the surface with an underwater upward looking color camera at various depths. This subsurface profiler is also equipped with a Nortek HR Profiler and ADV for current and turbulence measurements.

reference, R/V *Kilo Moana* sampled on station about 2 km north of R/P *FLIP* during the SBC experiment except during evening treks away from the site to discharge its tanks.

[14] The *Odyssey* and *REMUS* AUVs conducted their mapping surveys between R/P *FLIP* and R/V *Kilo Moana* as well as in their vicinities in patterns described by *Moline et al.* [2012]. Finally, it should be noted that R/P *FLIP* (Figure 2b) was allowed to drift in response to winds and currents during the Hawaii RaDyO experiment because mooring it in deep water was not feasible for our experiment. Furthermore, tilt effects were minimal in this case. The R/V *Kilo Moana* again sampled as close to R/P *FLIP* as safely allowable (generally within 2 km) and the *REMUS* AUV was occasionally used for spatial sampling.

2.2.2. R/V *Kilo Moana*

[15] The R/V *Kilo Moana* is a Small Waterplane Area Twin Hull (SWATH) vessel of 56.7 m length and with a beam of 26.8 and a draft of 7.0–7.6 m [see http://www.soest.

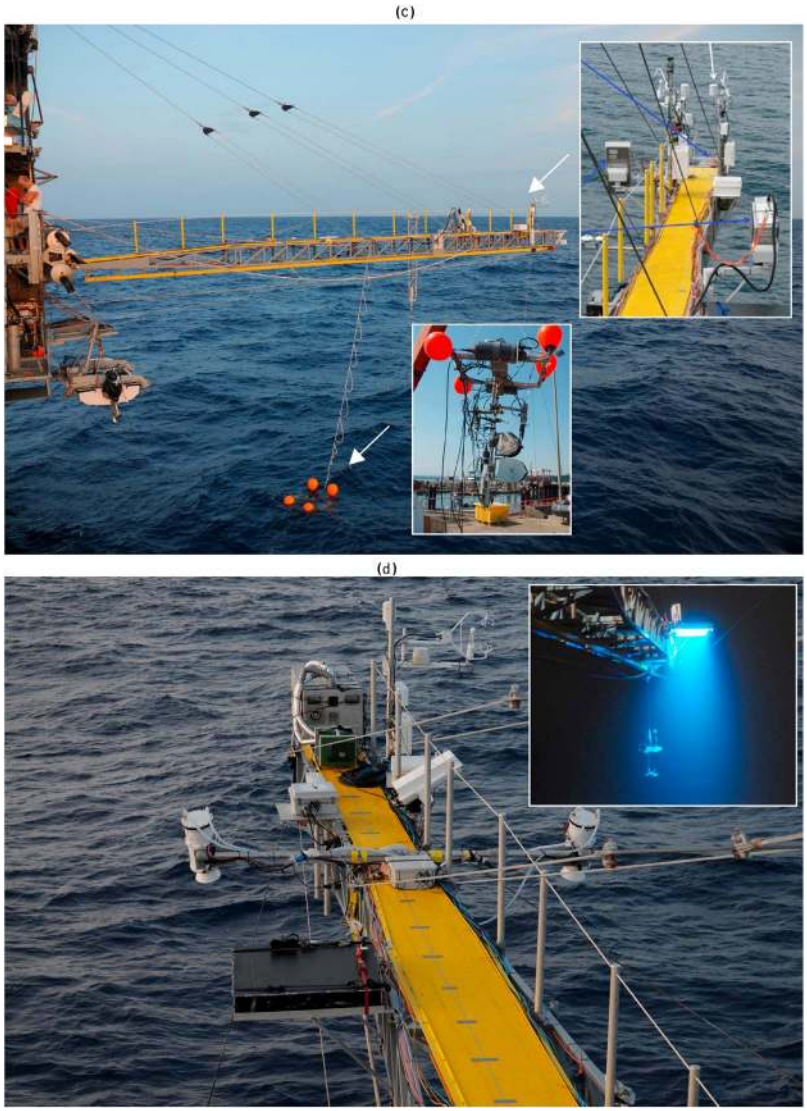

Figure 2. (continued)

hawaii.edu/UMC/KiloMoana.htm for details]. The R/V *Kilo Moana*, which was designed to minimize adverse motions via its design and motion compensation system in moderate to high sea states, was used for a variety of RaDyO measurements. In sea state 5 with significant wave heights of 2.5–4.0 m, R/V *Kilo Moana* 's maximum pitch is 9.2 deg, maximum heave is 8.2 m and maximum roll is 15.2 deg (all measured at the vessel's center of gravity). The instrumentation deployed from R/P *FLIP* and the R/V *Kilo Moana* is introduced below and discussed in more detail in other papers in this special section.

2.3. Measurement Systems

[16] Several standard and new technologies were critical for meeting the objectives of RaDyO. Some of the novel technologies included: (1) optical imaging systems capable of sampling at several Hertz and with spatial resolutions down to a few mm, (2) new imaging systems with high scene dynamic ranges to image both direct and diffuse radiance fields, (3) polarigraphic optical measurements, (4) underwater radiometric systems consisting of numerous radiance and irradiance sensors for fast sampling of wave-induced light fluctuations at 1 kHz frequency, (5) optical instruments for measuring absorption and scattering (some at multiple scattering angles) at multiple wavelengths in the visible spectrum, (6) meteorological instruments for directly measuring momentum and heat fluxes, (7) a small surface skimming vessel, *Lil KM*, for collection of microlayer surfactants and physical and optical measurements in the upper 1.7 m of the water column, and (8) two autonomous underwater vehicles for sampling physical and optical variability.

[17] For convenience, the general descriptions of RaDyO measurements are subdivided first by platform and then by disciplinary type. Most of the systems were similar for the SBC and Hawaii experiments, however significant differences are noted below for completeness. Readers interested in more detailed technical information and the names of investigators who were responsible for specific measurements are directed to the Website www.opl.ucsb.edu/radyo/ and other papers in this special section.

2.3.1. R/V *Kilo Moana* Measurements

[18] Observations were made from the R/V *Kilo Moana* using instrumentation provided by the University of Hawaii's instrumentation pool and by RaDyO research groups. During each cruise, the R/V *Kilo Moana*'s underway measurement system collected a variety of data at 1 to 10 s intervals depending on the variable and final processed data were averaged on time scales from 1 s to 5 min. The measurement systems deployed from the R/V *Kilo Moana* during RaDyO are summarized below, on the RaDyO website, and at http://www.soest.hawaii.edu/UMC/KM/scienceequipment.htm.

2.3.1.1. Meteorological Measurements

[19] The R/V *Kilo Moana*'s meteorological sensors were located at 20.7 m above the sea surface and data were collected through the ship's underway sampling system. Variables included: GPS position, meteorological variables of barometric pressure (Vaisala), wind speed and direction (RM Young), relative humidity (MP101A-C), precipitation (Rotronics), air temperature, shortwave and longwave radiation (Eppley PSP and PIR), and surface photosynthetically available radiation (PAR).

2.3.1.2. Physical Measurements

[20] Underway data were collected through the ship's intake, which was located 8 m below the sea surface, for obtaining uncontaminated seawater. These included: temperature and salinity (Sea-Bird SBE21), and the partial pressure of carbon dioxide (pCO_2; General Oceanics). The ship's CTD system (Sea-Bird 9/11+) included sensors for measuring pressure, temperature (dual sensors), conductivity (dual sensors), and dissolved oxygen (dual sensors) at 24 Hz. Data were processed into 1 m vertical bins. The CTD data were used on site for identifying features including the depths of the mixed layer, deep chlorophyll maximum layer, and particle maximum layer.

[21] The physical context of the specialized optical package called the MASCOT (Multi-Angle SCattering Optical Tool), which is described below, was quantified using an SBE49 CTD that was integrated into the MASCOT package [*Twardowski et al.*, 2012]. The physical data collected from the R/V *Kilo Moana*'s CTD and the MASCOT were consistent with each other. Thus, some of the R/V *Kilo Moana* and MASCOT profiles have been synthesized for plots shown in this paper. In addition, a CTD (Applied Microsystems) was deployed as part of the HyperPro optical profiling system by *Lewis et al.* [2011].

[22] One of the RaDyO program's goals was to resolve and model the dynamics of bubbles, their size distributions, and their effects on the subsurface optical fields. For this application, an acoustic resonator was attached for some of the MASCOT deployments to obtain simultaneous optical and acoustic data to ascertain the optical and acoustical effects of different bubble size distributions [*Farmer et al.*, 1998; *Czerski et al.*, 2011; *Vagle et al.*, 2012; *Twardowski et al.*, 2012]. One of the challenges of this work was to extend the frequency range of the acoustic resonator to be able to measure bubbles of radius less than about 20 microns and to invert attenuation data to obtain bubble numbers. In addition, the effort included a goal of simultaneously measuring bubbles with the acoustic resonator and an optical volume scattering instrument [*Czerski et al.*, 2011; *Vagle et al.*, 2012; *Twardowski et al.*, 2012] to determine their correspondence in overlapping bubble size ranges.

[23] Vertical profiles of currents were provided by the R/V *Kilo Moana*'s 38 kHz and 300 kHz ADCP systems (RDI) whose transducers were mounted at 8 m depth. The 38 kHz system obtained data downward from about 10 m for our study and the 300 kHz system obtained data from about 10 m to about 100 m. Data were recorded as 5 min averages and vertical binning of data was accomplished after the cruise. A scanning laser wave height (lidar) measurement system was deployed from a boom connected between the bows of the R/V *Kilo Moana*'s twin hulls [*Zappa et al.*, 2012]. The lidar altimeter was used to measure large-scale wave geometry (height and slope) by scanning downward toward the sea surface at 75 Hz from $\sim$9 m above the mean water level resulting in a sampling footprint of about 10 cm diameter with height accuracy of about $\pm$5 mm (rms).

2.3.1.3. Optical Measurements

[24] The R/V *Kilo Moana*'s underway sampling system measured chlorophyll *a* fluorescence (Turner 10-AU-005) as part of the data stream for the physical parameters. The ship's CTD system was also used to measure optical beam transmission (WET Labs C-Star), optical backscatter (WET Labs LSS 6000), chlorophyll *a* fluorescence (Seapoint), and PAR (Biospherical Instruments) at 24 Hz with binning at 1 m vertical intervals. An optical scattering instrument (LISST 100X, Sequoia) was also mounted on the CTD to measure near forward scattering with 32 ring detectors within the angular range of 0.08 to 13.5° at a wavelength of 532 nm. This instrument was also used in bench top mode to analyze discrete water samples. Water samples were collected using the CTD's 24-bottle rosette for analyses of absorption and scattering properties, particle size distributions, and the concentrations of particulate organic carbon, chlorophyll *a*, and total dry mass of suspended particulate matter. A Point-Source Integrating Cavity Absorption Meter, multiple path length, liquid core waveguide (MPLCW) absorption system, LISST 100X, and Coulter counter (Multisizer III, Beckman-Coulter) were used for some of this work. Similar analyses were made using water from the surface microlayer collected from a glass plate using a small boat launched from the R/V *Kilo Moana* [*Wurl et al.*, 2011].

[25] One of the objectives of RaDyO was to obtain high-fidelity inherent optical property (IOP) data, including the volume scattering function, in order to compute time-dependent radiance fields from incident light fields, which are modulated by the surface topography and its transmissive characteristics, using IOP data and radiative transfer models. To satisfy this objective, *Twardowski et al.* [2012] developed a special optical sampling system called MASCOT. Briefly, MASCOT uses a 658 nm laser light source and measures the volume scattering function (VSF or β) at 17 different angles from 10 to 170° with respect to the incident beam of light at 10° intervals with a sampling rate of 20 Hz. A linear polarizer was also used to obtain polarized VSF measurements in order to increase the information content concerning the particles' characteristics and size distributions. Other scattering measurements were obtained using an ECO-VSF (WET Labs) instrument for angles of 100, 125, and 150° at 650 nm, an ECO-BB3 (WET Labs) instrument for an angle of 117° at wavelengths of 462, 530, and 657 nm [see *Sullivan et al.* [2005] and *Twardowski et al.*

[2007b] for methodological details), and a LISST-100X Type B (Sequoia) for near forward scattering in 32 log-spaced angular increments from 0.08 to 13° at a wavelength of 650 nm. Light absorption coefficient, a, and total beam attenuation coefficient, c, (with total scattering coefficient, b, computed as the difference, b = c – a) measurements were made using WET Labs ac-9 and ac-s instruments [*Twardowski et al.*, 1999]. These instruments sampled at 6 Hz, with the former measuring at 9 wavelengths and the latter at 87 wavelengths in the visible.

[26] In addition, an acoustic resonator, which was described earlier [*Czerski et al.*, 2011; *Vagle et al.*, 2012], and a radiance camera (RadCam, described next and by *Lewis et al.* [2011]) were deployed with MASCOT for some measurements. Good agreement between the optical and acoustic attenuation measurements of bubble events was obtained [*Twardowski et al.*, 2012; *Czerski et al.*, 2011].

[27] *Lewis et al.* [2011] deployed new instruments capable of measuring the full radiance distribution above and below the water surface. The first of these, the HyperPro (or HyperProbe, Satlantic Inc.), is a profiling device that is deployed as a free-fall vehicle. The HyperPro, which sends data to the surface for real-time data processing, measured the following: downwelling (and uplooking) hyperspectral (124 wavelengths from 350 to 700 nm with 3 nm between bands) planar irradiance, upwelling (and downlooking) hyperspectral radiance with spectral characteristics as described for the downwelling sensors and with a half-maximum acceptance angle of 10° (half-angle of Field-of-View). A CTD (Applied Microsystems), chlorophyll *a* fluorometer and CDOM fluorometer (WET Labs), 2-channel backscatter sensors (470 and 670 nm), a GPS position and time system, and 2-axis tilt and roll sensors were also included in the HyperPro instrument package. This system was profiled to a depth of 60 m and also operated at a fixed depth of 10 m to obtain different spatial and temporal statistics. A Tethered Spectro-Radiometer Buoy (TSRB), which is essentially the same measurement device as the HyperPro, was tethered to a surface buoy [*Lewis et al.*, 2011]. The difference being that the downwelling irradiance sensor is inverted to measure upwelling irradiance. This system was floated away from the ship as data were collected to avoid ship shadowing and reflecting effects.

[28] The Radiance Camera (RadCam, Satlantic Inc.) is a new camera designed to measure spatial radiance distributions both at the ocean surface from the ship's deck and at depth [*Lewis et al.*, 2011]. A surface RadCam instrument was used as a reference camera for measuring incident downwelling radiance distributions (sky radiance). The subsurface RadCam, whose characteristics match those of the deck-mounted instrument, includes a fish-eye lens and measured downwelling radiance distributions as a function of depth, time, and wavelength or $L_d(z, \theta, \phi, \lambda, t)$ and $L_u(z, \theta, \phi, \lambda, t)$ where z is depth, θ is the zenith angle, ϕ is the azimuthal angle, λ is the wavelength of light, and t is time. The RadCam measured radiation at 555 nm (20 nm band-pass filter) over upward looking and downward looking hemispheres with an angular resolution of less than 1°, sampling rate of 7 Hz, and a dynamic measurement range of 10^6. These data are used to compute (via integration over appropriate solid angles) planar irradiance, scalar irradiance, reflectance, and average cosine, and inherent optical properties including the absorption coefficient and scattering phase function.

[29] The RadCam used for in-water profiling was a tethered free-fall system, designed to minimize the perturbing effects of ship shadowing and reflections. The profiling system also included sensors for measuring downwelling planar irradiance, E_d, and upwelling nadir radiance, $L_u(\theta = 180°)$, both at wavelengths of 412, 443, 490, and 555 nm, beam attenuation coefficient (25 cm path length at 532 nm (WET Labs), a CTD (Falmouth Scientific), and a tilt-heading sensor. This system was profiled and operated at fixed depths of 2 to7 m. Another self-contained RadCam was deployed from the *Odyssey* AUV described later.

[30] The R/V *Kilo Moana* was also used to launch a surface skimming sampler (*Lil KM*) and two autonomous underwater vehicles (AUVs). These platforms are described along with their measurement systems in the following subsections.

2.3.2. *Lil KM*

[31] Small-scale, near-surface physical, chemical, and optical data were collected using a specially designed microlayer skimmer, dubbed *Lil KM* (Figure 1), during the SBC experiment only and with the R/V *Kilo Moana*'s small boat during both experiments [*Wurl et al.*, 2011]. The microlayer skimmer is a self-contained remotely operated double-hulled vessel 1.5 m long and 1.4 m wide and with a draft of approximately 0.1 m. The skimmer uses 10 rotating glass disks equipped with Teflon wipers, a collection manifold, and a peristaltic pump to collect microlayer samples from eight pairs of individually controllable 250 ml plastic bottles for further analyses in the laboratory. The duration of each mission was typically between 1 and 2 h.

2.3.2.1. Physical Measurements

[32] During the SBC experiment, the *Lil KM* skimmer was equipped with an additional 1.7 m vertical 'mast' suspended below the two hulls to make measurements of temperature at 2–5 depths between 0.05 m and 1.68 m below the mean surface.

2.3.2.2. Optical Measurements

[33] The skimmer also measured chlorophyll *a*, colored dissolved organic material or chromophoric dissolved organic matter (CDOM), and 660 nm scattering at 1.68 m depth using WET Labs ECO triplet sensors mounted on the subsurface mast.

2.3.2.3. Chemical Measurements

[34] Surface-active substances modulate the microlayer of the near-surface light field. Importantly, compounds contributing to CDOM are often enriched in the sea-surface microlayer (SML). These substances absorb ultraviolet and other short-wavelength light energy [*Wurl et al.*, 2009] and are thus important for RaDyO. *Lil KM*, which was used for microlayer sampling as well as other measurements, was deployed during the SBC experiment six times from September 14–22, 2008 for periods of about 60–90 min, typically around 1530 UTC [*Wurl et al.*, 2011]. Microlayer and bulk water samples were also collected from the R/V *Kilo Moana*'s small boat using a glass plate and a small peristaltic pump [*Wurl et al.*, 2009], and from the R/V *Kilo Moana*'s CTD/rosette system. Some of the SBC data were collected within visible surface slicks and near R/P *FLIP* (i.e., September 21, 2008) over the 2 week sampling period.

The samples were analyzed either onboard the ship or taken back to a land-based laboratory for analyses.

[35] Particle size distributions and optical absorption and scattering by particles were measured to characterize particle properties within the microlayer in collaboration with Stramski and coworkers. Analyses were also done for dissolved carbohydrates, surface-active substances (SAS, e.g., surfactants), and surface active gel-particles (transparent exopolymers, TEP) [*Wurl et al.*, 2009]. *Wurl et al.* [2011] also studied the removal of CDOM from the SML via photochemical transformation and degradation as well as its enrichment in the SML via rising bubbles which scavenge organic material and carry it into the SML. Because of more adverse wind and wave conditions off Hawaii, *Lil KM* was not deployed. However, boat-based measurements similar to those done during the SBC experiment were made.

2.3.3. *Odyssey* Autonomous Underwater Vehicle

[36] An *Odyssey* autonomous underwater vehicle (AUV; hereafter called *Odyssey*) [*Moline et al.*, 2012, Figure 1] was deployed with physical and optical instrumentation during the SBC experiment to obtain spatial variability data in the vicinity of the R/P *FLIP* and the R/V *Kilo Moana.* One of the advantages of AUV's is that they can collect data away from ship's influence (e.g., shading and reflections). Because of anticipated adverse wind and sea states, the *Odyssey* AUV was not deployed during the Hawaii experiment. The vehicle is a free-flood, modular, midsized platform that is 0.5 m in diameter and 3.2 m long as configured for this experiment. The *Odyssey* can sample for 10 h with operating speeds between ~1.5 and 2 m/sec. Pitch and roll near the surface is about 2°.

[37] During the SBC experiment, the *Odyssey* AUV was operated in saw-tooth patterns with 10° pitch and level (along isobars) flights as well as vertical profiling mode. A 10° pitch can produce quasi-vertical profiles in the upper 30 m for every 170 m horizontal distance. Level flights provide horizontal spatial scales of physical and optical fields, while saw-tooth or profiling flights also provide vertical scale and gradient information.

2.3.3.1. Physical Measurements

[38] The *Odyssey* was equipped with a pumped CTD instrument, downward looking 300 kHz ADCP, microstructure sensing package, and optical sensors. Turbulence measurements were made with a microstructure package, which consisted of two fast response temperature sensors, two shear probes, pressure sensor, and three-axis linear accelerometer. High sampling rates were needed to achieve small spatial-scale irradiance measurements. In particular, turbulence variables and irradiance were sampled at 512 Hz and pressure was sample at 32 Hz.

2.3.3.2. Optical Measurements

[39] A nine-channel absorption and beam attenuation meter (WET Labs AC-9) was mounted in the midbody payload section of the *Odyssey*, which sampled water pumped from the same location as the CTD. An upward looking 7-channel irradiance sensor, two irradiance sensors, and a downward looking optical scattering sensor were also mounted in the payload section. To achieve high-resolution irradiance measurements, two single wavelength irradiance sensors (490 nm and 532 nm) were integrated into the RSI microstructure package. Sampling rates of the AC-9, 7-channel irradiance sensor, and backscattering sensor were 8 Hz. In addition, a RadCam (described above) was mounted on the top of the *Odyssey* to collect radiance data. By flying the AUV along isobars, it was possible to compute power spectra and other statistics of irradiance fluctuations.

2.3.4. *REMUS* Autonomous Underwater Vehicle

[40] A *REMUS* AUV [*Moline et al.*, 2012] (Figure 1) was deployed with physical and optical instrumentation during both the SBC and Hawaii experiments to obtain spatial data in the vicinity of the R/P *FLIP* and the R/V *Kilo Moana.* The vehicle uses a single pressure hull modular design and is 0.2 m in diameter and approximately 2 m long. The vehicle can sample at 1.5 m/sec for 10 h in the temperature environment of the study sites.

[41] During the SBC and Hawaii experiments, the *REMUS* AUV was operated in both fixed-level stepwise flight and saw-tooth mode with a similar pitch as the *Odyssey.* Level flights provided horizontal spatial scales of physical and optical fields, while saw-tooth or profiling flights also provided vertical scales and gradients.

2.3.4.1. Physics

[42] The *REMUS* AUV was equipped with a CTD and upward and downward looking 1200 kHz ADCPs. The CTD sensors, which were mounted in the nose of the vehicle, sampled at 12 Hz and were able to sample vertical gradients in the physical parameters at resolutions better than 2 cm.

2.3.4.2. Optics

[43] Also mounted in the nose section of the *REMUS* AUV with the CTD sensor were a 7-channel downward irradiance meter and sensors for measuring upward radiance, chlorophyll *a*, optical backscatter, and CDOM.

2.3.5. R/P *FLIP*

[44] For the SBC experiment, R/P *FLIP* was used for data collection from September 11 until September 22, 2008 at 34.2053° N, 119.6288° ^{0}W. For the Hawaii experiment south and southwest of the island of Hawaii, the free drifting R/P *FLIP* sampled from September 1 until September 14, 2009.

2.3.5.1. Meteorological Measurements

[45] Two separate, but similar, sets of meteorological data were collected during both of the RaDyO field experiments by *Zappa et al.* [2012] and Melville et al. (manuscript in preparation, 2012). Measurements included: near-surface barometric pressure, wind speed and direction, relative and specific humidity, air temperature, fast response water vapor, CO_2, and temperature sensors for heat flux measurements, longwave radiative downwelling flux, and shortwave downwelling irradiance (Kipp and Zonen pyrgeometer). All sensors were mounted at 10 m above sea level. Postprocessing of data allowed determinations of momentum flux (wind stress), turbulent latent and sensible heat fluxes, and net heat flux.

2.3.5.2. Physical Measurements

[46] R/P *FLIP* was used by the UCSB group for several physical and optical profiling and fixed-depth measurements. During the SBC experiment, a UCSB optical-physical profiling system was deployed to depths of 15 or 30 m. The profiling system included a CTD along with several optical sensors described in the next section. The physical and optical data were depth-binned to 10 cm and time-binned to 1 Hz. A total of 30 casts were made during the field experiment: 15 profiles down to a depth of 30 m, and 15 10 min long time series at a depth of 2 m. During the

vertical profiling, the package was left at 30 m for 5 min and was brought back to the surface at a rate of 1 m/min. Measurements were done from September 11 until September 14. Two vertical profiles were taken each day, one between 1200 and 1300 and another between 1530 and 1630; whereas the time series at 2 m were collected every hour, usually from 900 to 1700. Deep profiles were made at 1200, 1330, and 1500 local time on September 17 and at 1000, 1200, 1400, 1600, and 1800 on September 20.

[47] No profile measurements were made with the UCSB profiling system during the Hawaii experiment. However, several UCSB physical and optical sensors were mounted on R/P *FLIP*'s hull. Specifically, 22 temperature, 4 salinity, and 2 pressure sensors made measurements in the upper 85 m with these instruments (Figure 2).

[48] Vertical profiles of currents and wave directional spectra were obtained by a 600 kHz wave-enabled upward looking 600 kHz RDI ADCP mounted on R/P FLIP's hull at 30m water depth during the SBC experiment, and wave-enabled upward looking 600 kHz and downward looking 300 kHz RDI ADCPs mounted at 14 m water depth during the Hawaii experiment (Figure 2) were deployed by Melville et al. (manuscript in preparation, 2012).

[49] *Vagle et al.* [2012] deployed a CTD package mounted at 30 m on R/P *FLIP* to collect data every 10 min throughout the experimental periods. The package also included a dissolved oxygen sensor and a gas tension device. These data were used for interpretation of their bubble measurements as well as upper ocean physics. In addition, hull-mounted internally recording thermistors were deployed at depths of 3, 7, 15, 31, and 63 m.

[50] Surface roughness variability, small-scale waves, and wave breaking events were observed using suites of instruments measuring on scales down to millimeters from R/P *FLIP* during both field experiments by two wave-surface roughness groups: *Zappa et al.* [2012] and Melville et al. (manuscript in preparation, 2012). These data sets were collected to examine: (1) wave height and slope, (2) small-scale sea-slope field topography, and (3) microbreaker and whitecap crest length spectral density of breaker propagation speed as functions of wind speed, wind stress, and dominant sea states.

[51] *Zappa et al.* [2012] deployed a moderate field-of-view CEDIP infrared (IR) camera, three digital video cameras, and a Riegl laser altimeter as a system from R/P *FLIP*'s starboard boom. The IR camera measured thermal radiation at wavelengths of 7.7–9.3 μm emitted by the ocean surface using a 320 by 240 MCT focal-plane array with 14-bit digitization sampled at 60 Hz. Resulting temperature resolution was 0.02°C and calibration was better than 0.05°C. The three digital visible CCD cameras recorded images sampling at 20 Hz, two at 1250 $\times$ 1360 resolution and 12-bit digitization depth, and one at 1000 $\times$ 1000 resolution with 12-bit digitization depth. The laser altimeter, which operated at a wavelength of 0.905 μm, measured the distance to the surface. The IR and visible camera images were postprocessed to compute statistics on the scale, frequency, and speed of microbreaking and whitecapping events from scales of order 0.1 m s^{-1} up to scales of order 10 m s^{-1}. In particular, these data were used for determining breaking crest length spectral density distributions and their higher moments.

[52] The laser altimeter data were used to obtain wave spectra and other wave statistics including significant wave height and wave frequency. In addition, a synchronous orthogonal 75 Hz linear scanning laser altimeter system was used to provide spatiotemporal properties (interlaced x-z and y-z scans) of the wave height field resolved to the order of 0.5 m wavelengths. These measurements also provide phase of polarimeter images (described below) of surface microstructure needed for quantifying short wave modulation. This system was also located at 10 m height. The system scanned in two dimensions (using Cartesian coordinates) and the sampling footprint was about 10 cm. The accuracy of the measured height was about $\pm$5 mm (rms). The three cameras were used to observe wave breaking, foam, and whitecapping over fields of 10 $\times$ 15 m (2 cameras) and 100 $\times$ 200 m (1 camera), respectively. The former cameras were mounted near the fixed and scanning lidar system close to the end of a boom (10 m height) to measure intermediate scale breakers while the other was mounted on R/P *FLIP*'s crow's nest at about 26 m above water level for a broader viewing angle to record larger-scale breaking events. The sampling rates for all cameras were either 10 or 20 frames per sec. Data were generally collected for 20 min every hour; however, data were recorded more often during periods of more frequent wave breaking events.

[53] The phase-resolved, spatial-temporal history of small waves was measured using the shape-from-polarimetry (SFP) technique first described in *Zappa et al.* [2008]. The SFP technique relates the change in polarization of skylight reflecting from water to infer the orientation of the water surface at the point of reflection.

[54] With funding from an Office of Naval Research DURIP award, and in cooperation with Polaris Sensor Technologies, an imaging polarimeter was specifically designed and built for oceanographic applications by *Zappa et al.* [2012]. The imaging polarimeter collected 782 $\times$ 582 pixel 10-bit monochrome images at 60 Hz. The instrument was equipped with a $\sim$3.5 deg field-of-view lens, which resulted in a surface footprint of approximately 1 $\times$ 1 m. The design and results are described in more detail in *Zappa et al.* [2012].

[55] The imaging polarimeter was deployed in a water resistant housing from the starboard boom 9 m above the surface. The sensor was oriented so that it observed the ocean surface at a 37 deg incidence angle. The housing contained the imaging polarimeter, an attitude heading and reference system with a dual GPS antenna for collecting heading data, a Camera Link to fiber optic interface, and a temperature sensor. The raw noncompressed image data and orientation data were tagged with GPS time and recorded in real-time using an IO Industries frame grabber and SAS RAIS system.

[56] Melville et al. (manuscript in preparation, 2012) deployed a set of **e**lectro-optical sensors from the starboard (for SBC) and port (for Hawaii) booms of R/P *FLIP* to characterize the influence of wave breaking at the ocean surface on oceanic radiance and imaging. These included a Riegl Q240i scanning laser altimeter for surface displacement and slope measurements, stereo visible and infrared cameras (JaiPulnix TM4100CL 4Mpx visible cameras and FLIR SC6000 LWIR infrared cameras (640 $\times$ 512px) sampled at 10 Hz and 40 Hz respectively) for 3D surface

reconstruction, wave kinematics and breaking characteristics estimation, dual 11 megapixel, 12 bit digital cameras mounted on the crow's nest of R/P *FLIP* (Figure 2) for whitecap statistics and kinematics. In addition, an electro-optical package was deployed at the very end of the port boom during the Hawaii deployment. [This instrument was not deployed during the SBC experiment after the failure of the port boom, subsequently replaced prior to the Hawaii deployment.] For this experiment we upgraded the midwave infrared (MWIR) digital camera to an Indigo Phoenix camera (320 × 256px, 50 Hz frame rate), and replaced the video camera by a JaiPulnix 3CCD color camera (CV-M9CL, 1360 × 1024px, up to 50 Hz sampling rate). The system also includes a 60-W air-cooled CO_2 laser (Synrad Firestar T60) equipped with an industrial marking head (Synrad FH index) with two computer controlled scanning mirrors and a laser altimeter (Riegl LD90–3100-EHS). To characterize the light transmission across the water surface, this group also deployed a downward looking LED screen (Figure 2) used to display preprogrammed targets, imaged through the water surface by an upward looking color camera (Prosilica GC1380C) mounted on a small underwater profiler fitted with additional subsurface instruments to characterize turbulence and bubble injection below the surface (Nortek HR profiler and Vector ADV). Instruments were sampling continuously, except the scanning lidar and imaging systems that were recording for 20 min per hour.

[57] Information concerning upper ocean bubble structure was obtained by *Czerski et al.* [2011] and *Vagle et al.* [2012]. Data were obtained within a radial distance of about 250 m of R/P *FLIP* using a Doppler sonar system consisting of four 100 kHz side scan transducers oriented orthogonally, 15° up from the horizontal plane, at a depth of 30 m. A horizontally mounted 300 kHz acoustic Doppler current profiler (ADCP) was also mounted at 30 m depth and operated throughout the experiment. A CTD package described earlier was mounted at 30 m to collect temperature, conductivity, and pressure data at 30 m every 10 min. A dissolved oxygen sensor and a gas tension device (GTD) were included in the CTD package for measurements of the total pressure of all dissolved gases. Since air is mostly made up of the biologically active oxygen (O_2) and the practically inert nitrogen (N_2), the GTD measurements combined with O_2 measurements allow for estimating N_2 concentrations, which are needed for proper interpretation of the bubble measurements.

[58] For in situ near-surface measurements of optically active properties of the upper ocean, a small (1.5 m by 1.5 m) wave-following float (Figure 2c) was also deployed between the booms of R/P *FLIP* by *Vagle et al.* [2012]. The float was equipped with two acoustical resonators for in situ measurements of the bubble size distributions at two depths (0.5 and 1.5 m), three 2 MHz Doppler sonars (Dopbeams) for measuring backscatter and near-surface turbulence along 1 m paths, conductivity-temperature packages at 0.35 and 1.8 m, an inductive conductivity sensor used to measure high air fractions in breaking waves, and a sensor package with a pressure sensor, plus heading and tilt sensors. In addition, *Zappa et al.* [2012] deployed a side-looking high-resolution Aquadopp, which was mounted at 2 m depth to measure backscatter and near-surface turbulence along 1 m paths. Attached at 5 m below the float was an upward looking 200 kHz short pulse (250 μs) backscatter sonar system used to map the larger-scale bubble field in the vicinity of the float. Finally, two black and white video cameras collected images in the vicinity of the float to ascertain the presence or absence of wave breaking over the float and to indicate the presence or absence of surface foam lines associated with Langmuir circulation.

2.3.5.3. Optical Measurements

[59] The UCSB profiling CTD system, which was used only for the SBC experiment, also included a hyperspectral absorption-attenuation instrument for measuring optical absorption and attenuation, a and c (ac-s, 87 wavelengths), another absorption-attenuation instrument (WET Labs AC-9) for measuring a and c with a filter on the a-tube for CDOM (Nucleopore 0.2 μm pore size filter, 9 wavelengths in the visible), an optical backscatter instrument for measuring b_b at 9 wavelengths in the visible, a fluorometer-turbidity instrument for measuring chlorophyll fluorescence (470 nm ex/695 nm em) and turbidity (700 nm), and a near forward scattering instrument for measuring particle size distributions (characteristics similar to those of the LISST instruments described earlier).

[60] Fixed-depth time series measurements were also made with UCSB systems during the SBC experiment using another measurement system that was mounted on the hull of R/P *FLIP* at a depth of 2 m. This system, called the WQM (WET Labs [*Janzen et al.*, 2008]), included a combined CTD/dissolved oxygen system, and a combined chlorophyll *a* fluorometer and turbidity sensor. For the Hawaii experiment, UCSB R/P *FLIP* hull-mounted optical measurements were made using WQM instruments as described above for fluorescence and turbidity at four depths (13, 20, 40, and 68.5 m).

[61] Another suite of specialized optical measurements was utilized during both the SBC and Hawaii experiments. Radiometric measurements of wave-induced light fluctuations were made with the Underwater Porcupine Radiometer System [*Darecki et al.*, 2011]. The Porcupine is a new instrument developed specially for the RaDyO project. It has a unique design and capability to sample rapid fluctuations in both radiance and irradiance fields at 1 kHz. The Porcupine was equipped with 7 radiometric sensors to measure downwelling plane irradiance, E_d, at wavelengths of 365, 410, 443, 488, 532, 610, and 670 nm. The cosine collectors were 2.5 mm in diameter. In addition, the Porcupine included 16 radiance sensors to measure downwelling radiance, L_d, at 532 nm at different zenith angles within two orthogonal azimuthal planes.

[62] Other radiometric measurements were made with several Ramses (TriOS GmbH) hyperspectral radiometers [*Darecki et al.*, 2011], which provided time-averaged light field characteristics (averaging times typically from about 0.5 s to a few seconds). The measurements with these radiometers provide, for example, hyperspectral average cosine data for the underwater light field, an apparent optical property characterizing the angular distribution of the light field. The Ramses radiometers attached to the Porcupine measured in-water hyperspectral (190 channels within the wavelength range 320–950 nm; 3.3 nm resolution) downwelling plane irradiance, E_d, downwelling scalar irradiance, E_{od}, downwelling radiance (0 deg, zenith radiance), L_d, and chlorophyll fluorescence. A radiometer mounted on a

surface float was used to measure hyperspectral (320–950 nm) upwelling radiance, L_u, just below the sea surface (180 deg; nadir radiance), and two deck radiometers measured hyperspectral E_d and E_{od} incident on the sea surface.

[63] *Bhandari et al.* [2011] used cameras designed for measurements of polarized radiance distributions for deployments from R/P *FLIP* above the surface (SKY CAM) and in the water (DPOL, Downwelling POL camera system) for both the SBC and Hawaii RaDyO experiments. The DPOL system allows measurements of one hemisphere of the polarized radiance distribution at 5 wavelengths (442, 488, 520, 550, 589 nm) and can be deployed for either downwelling or upwelling radiance distributions. For the downwelling radiance distribution, the DPOL was deployed below several of the wave measurement systems whereas for the upwelling radiance distribution, the system was deployed using floats away from the R/P *FLIP*. By using a combination of four simultaneously acquired images, the four Stokes parameters I, Q, U, and V can be acquired at a given wavelength. When measuring the downwelling radiance distribution, depths were varied from 0.5 to 40 m in the SBC and 1 to 70 m during the Hawaii experiment, with sampling at each depth for approximately 30 min.

[64] The SKY CAM measured the surface downwelling spectral radiance distribution at 8 wavelengths (442, 488, 520, 550, 589, 650, 766, and 855 nm). This system is a newer version of an older SKY CAM system [*Voss and Liu*, 1997]. This system was deployed from an R/P *FLIP* boom and the camera was placed in a gyroscopically stabilized mount with azimuthal control. This system typically collected data at each wavelength every 15 min throughout the day. With this system, 3 sequential images are combined to obtain three of the polarization Stokes vectors (I, Q, and U), since in the atmosphere the Stokes vector V is very small. Aerosol optical depth (AOD) was also measured simultaneously with DPOL and SKY CAM observations with a handheld Sun photometer (Microtops). During the Hawaii experiment, a RADCAM [*Lewis et al.*, 2011] was also deployed from R/P *FLIP*.

2.3.6. National Data Buoy Center – Buoy 46053

[65] During the SBC experiment, meteorological and oceanographic data were routinely collected by NOAA's National Data Buoy Center (NDBC) from NDBC buoy 46053. The 3 m disc buoy was located in the SBC about 22.2 km (12 nmi) southwest of Santa Barbara at 34.25 N 119.84 W in water of depth 450 m or about 22 km generally west of the RaDyO SBC study site (Figure 4). Data of interest for our experiment were collected 1 September to 1 October 2008.

2.3.6.1. Meteorological Measurements

[66] Time series data collected from the NDBC buoy included wind speed and direction at 5 m height above the sea surface, wind gust, air temperature, barometric pressure, and pressure tendency at sea level.

2.3.6.2. Physical Measurements

[67] NDBC buoy 46053 oceanographic time series data included: ocean temperature at a depth of 0.6 m, mean wave height, significant wave height, swell height, direction and period, mean wave direction, average wave period, and dominant wave period with the maximum wave energy. More information on these measurements can be found at http://www.ndbc.noaa.gov/station_page.php?station=46053.

2.3.7. Shore-Based High-Frequency Surface Current Observations

[68] Near-surface currents in the Santa Barbara Channel have been measured since 1997 using a shore-based array of high-frequency (HF) radars along the mainland coast and on Santa Cruz Island. Several SBC studies have used these radars previously [e.g., *Nishimoto and Washburn*, 2002; *Beckenbach and Washburn*, 2004; *Emery et al.*, 2004; *Bassin et al.*, 2005; *Anderson et al.*, 2006, 2008]. The HF radars used in this study operated at 12–13 MHz and measured currents over the upper 1 m of the water column. The radial components of current velocity were measured every 10 min and spatial resolution of radial currents was 1.5 km in range and 5° in azimuth. Averages of 1 h were used for the plots shown in this paper. Daily plots were computed as 25 h averages to minimize effects of tidal flows. Surface current vectors were interpolated onto a 2 km square grid based on all radial currents within 3 km of each grid point using a least square fit. An eddy tracking algorithm developed by *Nencioli et al.* [2010] was applied to the HF radar data collected during the experiment and results are described by *Dong et al.* [2012].

2.3.8. Aircraft Operations

[69] The airborne scanning LIDAR system developed by *Reineman et al.* [2009] was installed in the cabin of a Twin Piper Comanche aircraft to measure the spatial evolution of the wavefield in the vicinity of R/P FLIP and R/V Kilo Moana during the Santa Barbara Channel Experiment on 16 and 19 September 2008 (Melville et al., manuscript in preparation, 2012).

2.3.9. Satellites

[70] In order to characterize the general setting and larger-scale variability of the SBC and Hawaii RaDyO experimental regions, satellite-based wind, sea surface temperature, and ocean color were obtained. Surface roughness (synthetic aperture radar (SAR)) measurements were collected for the SBC experiment only. Satellite-derived SST and chlorophyll *a* imagery were at times not useful due to cloud cover.

2.3.9.1. Wind Measurements

[71] For regional surface wind speeds and directions, NASA's QuikSCAT scatterometer was utilized. QuikSCAT, which is a polar orbiting satellite, provided wind data over an 1800 km wide swath for our two study regions (see QuikSCAT website: www.podaac.jpl.nasa.gov/quikscat). The retrievals of wind speed and direction from QuikSCAT gave twice-daily data with spatial resolution of 25 km × 25 km on the Earth's surface.

2.3.9.2. Sea Surface Temperature Measurements

[72] NASA's MODIS sea surface temperature (SST) imagery data (9 km pixel resolution) were obtained. The MODIS Aqua satellite images the full earth every 1–2 days, therefore the daily composites usually provided coverage over our study areas every other day. Eight day averages over 9 × 9 km areas were used for our analyses. The preceding data were level 3 products obtained from podaac.jpl.nasa.gov.

2.3.9.3. Color Measurements

[73] NASA's MODIS ocean color data were used to determine average near-surface chlorophyll *a* concentrations over 8 days and areas of 9 × 9 km (data obtained from oceans.gsfc.nasa.gov). The MODIS imagery had 9 km

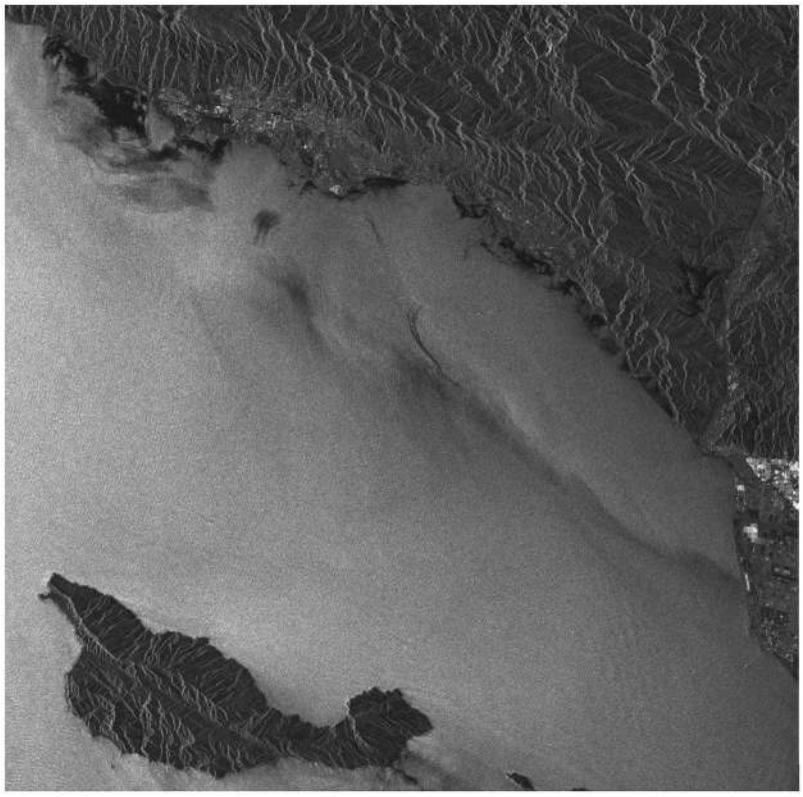

Figure 3. Satellite SAR image from Envisat ASAR (copyright ESA) obtained 20 September 2008, at 05:45 UTC. At the time of acquisition, the nearby NOAA buoy 46053 measured a wind speed of 9.4 m/s with a direction of 280°, wave height of 1.3 m, wave direction of 284° and dominant wave period of 13.8 s. The high winds account for the overall bright/high radar backscatter returns. Swell with refraction patterns around Santa Cruz Island are detectable. Atmospheric frontal patterns are discernible at the east end of Santa Cruz and in the northerly midchannel. Closer to the coast, natural seeps appear as dark, thin, curvilinear features, including a pair of seeps emanating near a pair of drilling platforms. Dark wind shadows are seen close to the coastline from west of Santa Barbara southward toward Ventura.

ground pixel resolution with chlorophyll *a* concentrations being calculated using standard NASA data processing routines and algorithms (see http://oceancolor.gsfc.nasa.gov/PRODUCTS/).

2.3.9.4. Surface Roughness–Synthetic Aperture Radar Measurements

[74] For the SBC experiment, satellite synthetic aperture radar (SAR) imagery was obtained by Ben Holt (JPL) from the European Space Agency's Envisat and ERS-2 satellites with ASAR and SAR sensors, respectively. Envisat ASAR data were primarily obtained with each beam having 25 m pixel resolution and 100 km swath width. The ERS-2 SAR provided data with 25 m resolution and 100 km swath width. Imagery was obtained on the following dates: 4, 7, 10, 20, 23, and 26 September in 2008. These data sets are useful for detecting surface features such as slicks and estimating wave direction and wavelength, wind speed, and current patterns [*DiGiacomo and Holt*, 2001: *DiGiacomo et al.*, 2004]. A sample SAR image frame is shown in Figure 3.

3. Background for the Santa Barbara Channel RaDyO Study

[75] The Santa Barbara Channel (SBC) is approximately 40 by 100 km in size and reaches a maximum depth of about 600 m near the center of the basin (bathymetry shown in Figure 4). The SBC is bordered by the Santa Ynez Mountain Range (reaching over 1200 m in elevation) to the north and the Santa Barbara Channel Islands to the south. The SBC is a relatively well-defined and delimited oceanic water body as shown in Figure 4. Local topography and coastline geometry significantly influence the local meteorological conditions [e.g., *Carvalho et al.*, 2012].

[76] The Radiance in a Dynamic Ocean (RaDyO) program conducted its second field experiment in the SBC (Figure 4). Observational platforms including the R/V *Kilo Moana*, R/P *FLIP*, two autonomous underwater vehicles (AUVs), a surfactant skimmer, and a small aircraft (see Figure 1 for all except the aircraft) were used to collect data during the period of 3–25 September 2008 in the vicinity of 34.2053° N, 119.6288° in waters of depth of about 170 m. These platforms collectively obtained high temporal and spatial resolution data sets. During the RaDyO Santa Barbara Channel experiment, the R/V *Kilo Moana* operated within about 2 km (generally north) of R/P *FLIP* (Figure 4) during daylight hours, but had to leave the area during a few hours in the evenings. R/P *FLIP* began sampling on 10 September 2008 and finished on 25 September 2008 whereas R/V *Kilo Moana* began measurements on 9 September 2008 and

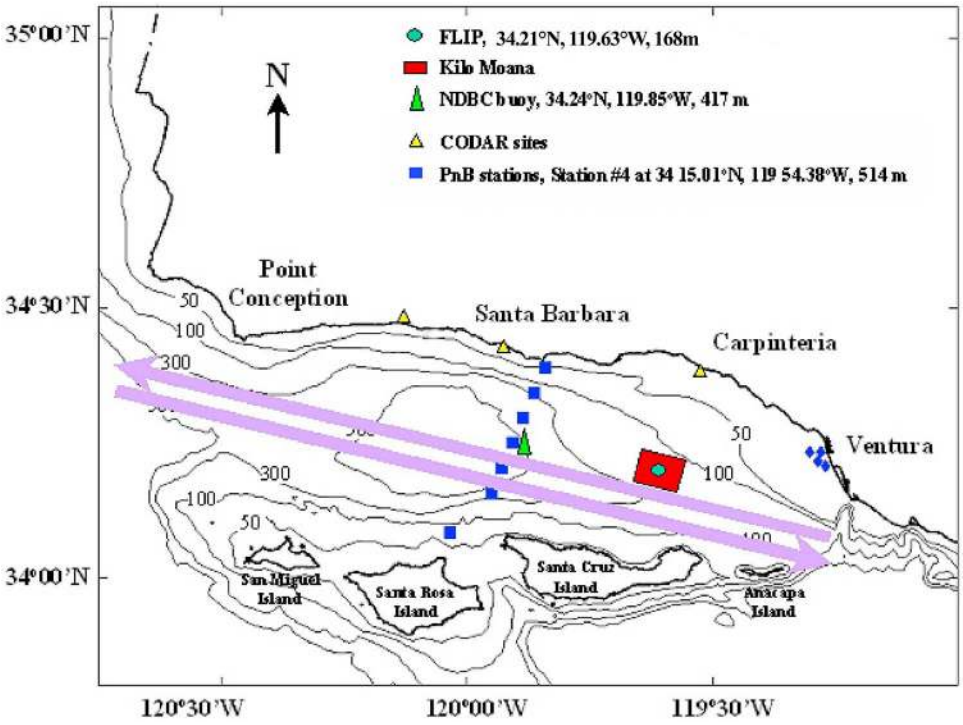

Figure 4. Geographic and bathymetric map of region of the RaDyO field experiment conducted in September 2008 in the Santa Barbara Channel. The main site of the RaDyO SBC experiment is indicated by the red box and complementary measurement and instrumentation locations are described in the key.

terminated them on 22 September 2008. Again, complementary in situ, aircraft, satellite and shore-based data sets have been analyzed to allow broader-scale interpretation of the dedicated RaDyO data sets.

3.1. Results for the Santa Barbara Channel Experiment

[77] General atmospheric and oceanographic conditions existing in the region of the Santa Barbara Channel (SBC) for September 2008 are described next to provide the broad context of the RaDyO observations made in the eastern portion of the SBC from 3–25 September 2008 in the vicinity of 34.2053° N, 119.6288°. Please note that throughout the paper times are given as UTC and use the year day definition (i.e., 1 January, noon = year day 1.5). More detailed papers in this section and elsewhere present more specific results of the experiment.

3.1.1. Wind Stress Patterns and Variability

[78] Many different factors, which vary on a broad range of spatiotemporal scales, must be considered to understand and quantify the SBC's meteorology, which is complex and thus demanding of numerical model simulations [see *Carvalho et al.*, 2012]. The purpose of this section is to summarize the wind patterns and their variability as the wind-forcing conditions for the SBC RaDyO experiment. First, climatological wind stress analyses for coastal California were examined and satellite wind stress data (QuikSCAT) were used to document the wind fields over the waters offshore of central and southern California (Figure 5). Time series meteorological and atmospheric flux records were obtained from the R/V *Kilo Moana*, R/P *FLIP*, and the NDBC buoy.

[79] The wind pattern based on QuikSCAT satellite wind stress data from 5 to 28 September were quite regular with winds persistently directed southeastward along the California coast and thus almost always upwelling favorable (Figure 5). This wind pattern, caused by relatively high atmospheric pressure (anticyclone) in the eastern North Pacific and relatively low (thermally induced) pressure over the southwest U.S. in the late summer and early autumn [e.g., *Dorman and Winant*, 1995; *Winant and Dorman*, 1997], varies on the synoptic scale with strengthening and weakening of the pressure systems and shifts in their position. No major low-pressure systems passed through the site during the experimental period, which is consistent with seasonal climatology [*Winant and Dorman*, 1997].

[80] Unfortunately, no satellite wind data are available within the SBC because of nearness to land and limited spatial resolution. However, wind data collected in the SBC from R/V *Kilo Moana*, R/P *FLIP*, and the NDBC buoy show that the winds are generally directed toward the east at the study site (Figure 6) [*Zappa et al.*, 2012; *Carvalho et al.*, 2012.]. The meteorological data collected from R/V *Kilo Moana* and R/P *FLIP* were virtually identical when the platforms were near each other. The observed change in direction of the wind from generally southeastward to eastward in the vicinity of Point Conception is well documented and winds roughly follow the coastline [see *Dorman et al.*, 1999; *Skyllingstad et al.*, 2001]. While there is a strong diurnal signal in the westerly wind speed in the SBC, only very brief wind reversals were observed at the RaDyO site during the period of 21–23 September (YD 265–267) as indicated in Figure 6. These reversals may be indicative of

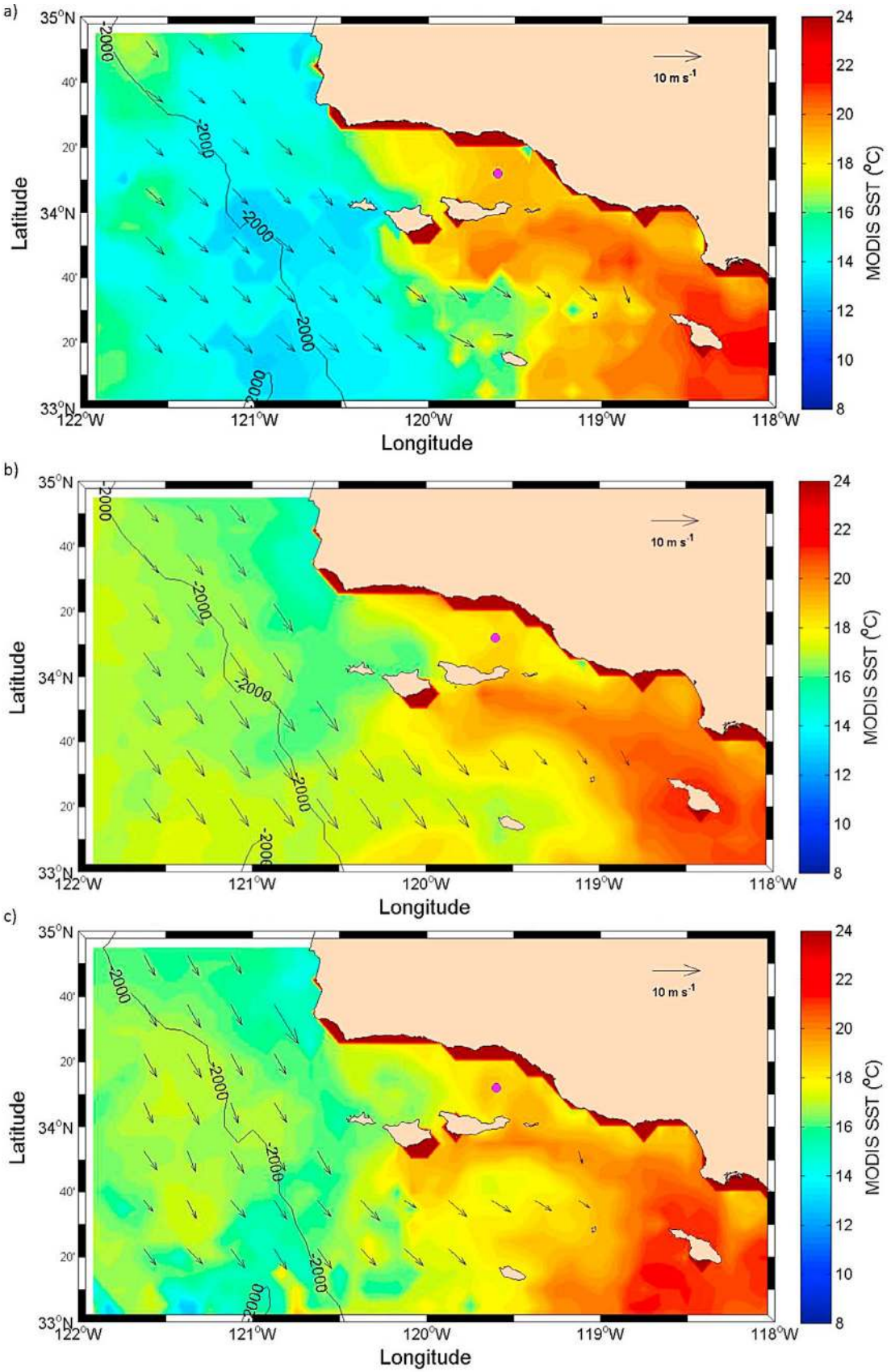

Figure 5. Satellite wind vectors (from QuikScat) and sea surface temperature (from MODIS, daytime) images for the periods of (a) 6–12 September 2008 (YD 249–256), (b) 13–20 September 2008 (YD 257–264), and (c) 21–28 September 2008 (YD 265–272).

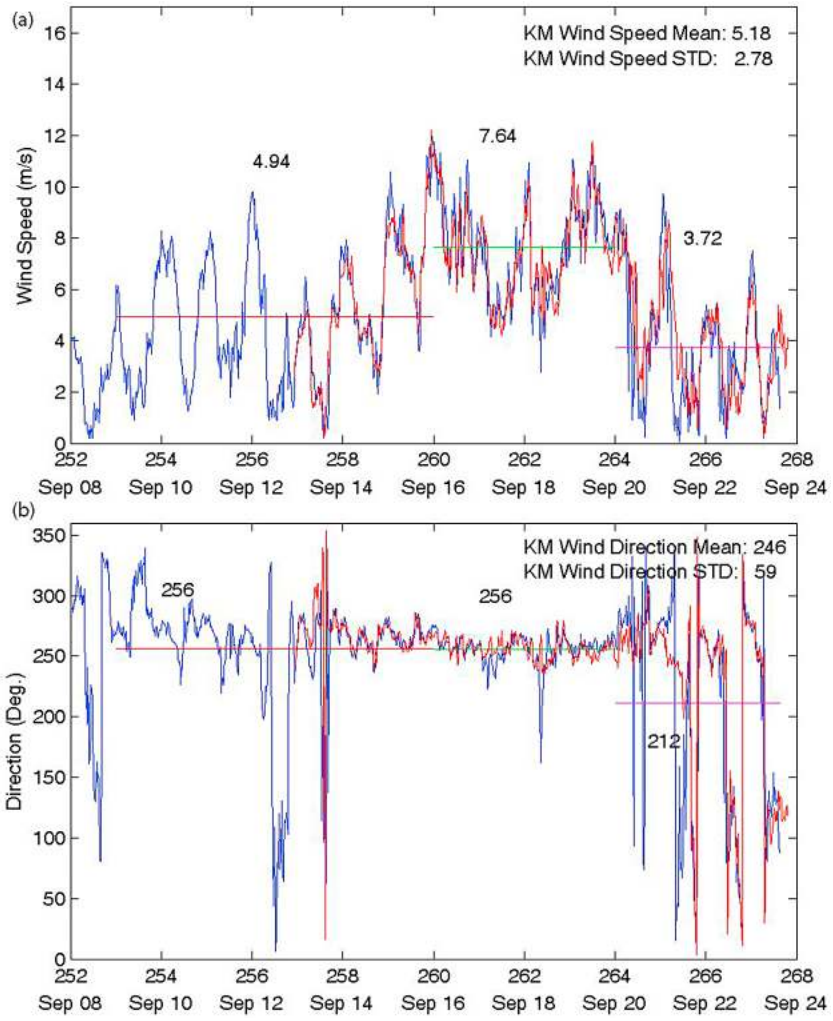

Figure 6. (a) Wind speed time series data obtained from the R/V *Kilo Moana* (blue) and R/P *FLIP* (red). Mean and standard deviations were computed using R/V *Kilo Moana* data. (b) Similar figure for wind direction with same color coding.

atmospheric eddies which sometimes set up over the region or may possibly be associated with atmospheric Kelvin waves [e.g., *Kessler and Douglas*, 1991; *Dorman and Winant*, 1995, 2000]. The atmospheric modeling work of *Carvalho et al.* [2012] provides more insights into the atmospheric dynamics.

[81] As indicated by time series of wind speed data shown in Figure 6a, three fairly well-defined periods of mid-to-high-to-low wind speeds occurred during the RaDyO SBC experiment with average wind speeds (1) for 9–15 September (YD 253–259) of 4.9 m/sec, (2) for 16–19 September (YD 260–263) of 7.6 m/sec, and (3) for 20–23 September (YD 264–267) of 3.7 m/sec (Figure 6a). These three periods, which are associated with the relative strengthening and weakening of the larger-scale atmospheric pressure systems over the Pacific and southwest U.S., motivate further inspection of the oceanographic responses. The greatest wind speeds (~12 m/sec) for the study occurred during the afternoon of 16 September (YD 260). Diurnal variations in wind speed are clearly evident in the time series shown in Figures 6a with peak winds typically occurring in the early afternoons. Figure 7 shows the summary of the atmospheric conditions for the Santa Barbara Channel experiment. The strong diurnal cycle in the wind speeds and wave height throughout the experiment is confirmed in the spectra of the wind speed, U_{10}, and significant wave height, H_s, shown in Figure 8. The mean wind speed for the experiment was 5.2 m/sec with a standard deviation of 2.8 m/sec, typical for this time of year [e.g., *Winant and Dorman*, 1997; *Dorman and Winant*, 2000]. The data reported here have been used by *Carvalho et al.* [2012] for comparison with their atmospheric model simulations, which elucidate the dominant regional atmospheric processes for the RaDyO experiment.

3.1.2. Oceanographic Conditions

[82] The Santa Barbara Channel RaDyO field experiment focused on a relatively small geographical region since the scales of interest were primarily on order of a few hundred meters in the horizontal scale and up to a few weeks in duration. However, it was important to characterize larger-scale phenomena that affect the smaller-scale processes as well. In addition, the more localized RaDyO observations have been used to test atmospheric and oceanographic models devoted to the larger scales [*Carvalho et al.*, 2012; *Dong et al.*, 2012]. With this motivation, we provide a brief

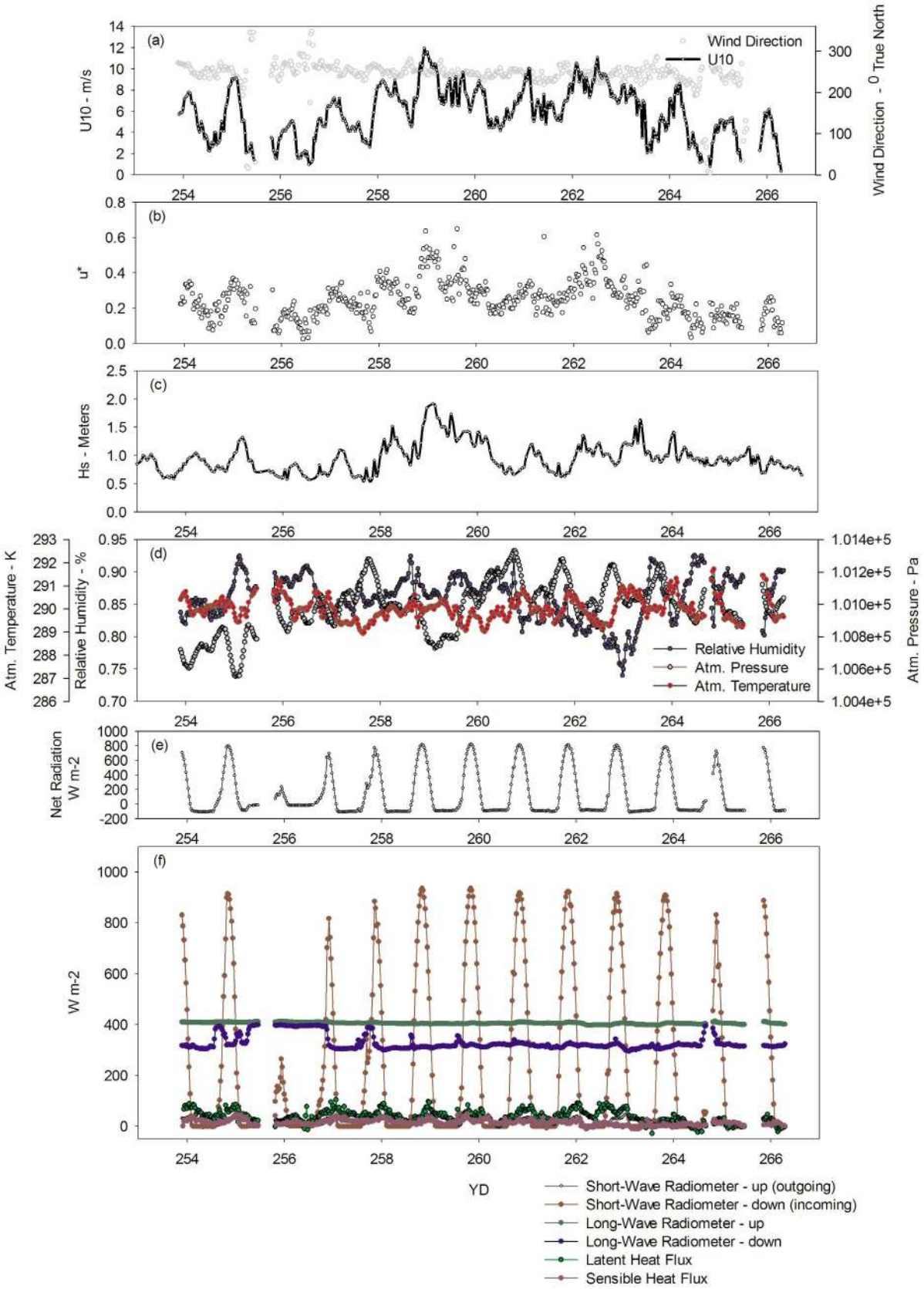

Figure 7. Environmental conditions during the Santa Barbara Channel Experiment, September 2008, recorded from R/P *FLIP* (Melville et al., manuscript in preparation, 2012). Note the strong diurnal cycle in the wind speed and wave height while the wind direction remains relatively fixed with only a few episodes of changing direction.

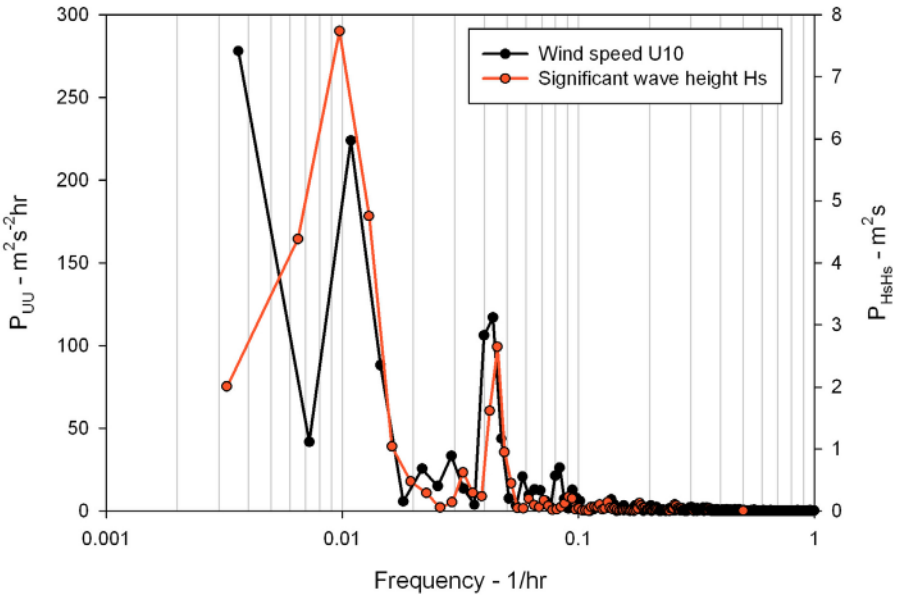

Figure 8. Spectra of 30 min averaged wind speed U_{10} and significant wave height H_s for the entire Santa Barbara Channel experiment record, in September 2008, showing a clear diurnal cycle (Melville et al., manuscript in preparation, 2012).

summary of the oceanographic conditions for the period of the SBC RaDyO experiment in the context of the three meteorological forcing regimes.

3.1.2.1. Currents

[83] Horizontal current data for the SBC experiment were derived from three sources: high-frequency (HF) radar using stations located along the coast for near-surface, channel-wide currents, ADCP data collected from R/P *FLIP*, R/V *Kilo Moana*, and two AUVs (Figure 4). The high-frequency radar surface current data (Figure 9) characterize the evolving spatial patterns of near-surface currents (averaged over ~1 m depth), which are important for determining advection of substances in surfactants and organic and inorganic particulate and dissolved matter, all of which affect optical properties. In addition, the surface wavefields are affected by the regional surface currents and vice versa. The uplooking ADCP data collected from R/P *FLIP* (~1–25 m) provide high-resolution current data at depths of primary interest for the experiment. Finally, the R/V *Kilo Moana* ADCP data (~10–200 m) complete the current records for the upper ocean. There are a few time gaps in the R/P *FLIP* data as seen in Figure 10. Evening gaps in the reported R/V *Kilo Moana* ADCP data arose from necessary excursions of more than 1.5 km from the R/P *FLIP* mooring site. These are the most problematic because of severe aliasing of current data accentuated primarily by the diurnal wind-forcing and secondarily the tides. For these reasons, the subsurface current records need to be interpreted with these deficiencies in mind.

[84] We begin the discussion with the HF radar current maps shown in Figure 9, which are a subset (12, 19, and 23 September; YD 256, 263, and 267) of the entire record. Data shown in these figures are centered on the time periods of the three wind-forcing regimes (Figure 6) of daily HF radar current maps, which are available on the Website http://www.icess.ucsb.edu/iog/archive/25_hr_means_menu.php. Currents using HF data were computed using 25 h averages to minimize tidal effects. It is worth noting that currents measured at depths of even a few meters by ADCP current profilers can be quite different from HF-measured (~1 m) surface currents [e.g., *Siegel and Lohrmann*, 2010]. These differences are not unexpected considering near-surface veering due to Ekman veering effects as well as differences in methodologies, fundamental sampling and averaging schemes, and the lack of perfect colocation of all instruments. Overlapping ADCP current data collected by the R/P *FLIP* and the R/V *Kilo Moana* were generally consistent when the R/V *Kilo Moana* was stationed within about 1.5 km of the moored R/P *FLIP*. Throughout the experiment, near-surface and upper ocean currents have a large diurnal component associated with the diurnal wind-forcing. The mean currents for each of the three designated periods are usually several times smaller than peak currents associated with the diurnal wind-forcing. The flow pattern for the period of 9–15 September (YD 253–259) is characterized by a cyclonic eddy centered near the deepest portion of the SBC (Figure 9a showing YD 256 or 12 September). The eddy extended nearly across the Channel (over 20 km north-south and east-west). Eastward flow was seen north of Santa Rosa and Santa Cruz Islands. The mean surface currents at the RaDyO site for the first period were 3.3 cm/sec eastward and 4.1 cm/sec southward. Currents in the upper 20 m indicate some shifting of directions as shown in Figure 10 (note transition from generally northward to southward around YD 257). The currents of the upper 20 m were fairly coherent with depth, although some vertical shear of horizontal currents was evident.

[85] The greatest wind-forcing for the experiment occurred during the next period (16–19 September; YD 260–263). The eddy over the proximate center of the basin (somewhat to the west of the geometric center at 34.25 N, 120.1W) remained during the period; however, the flow to

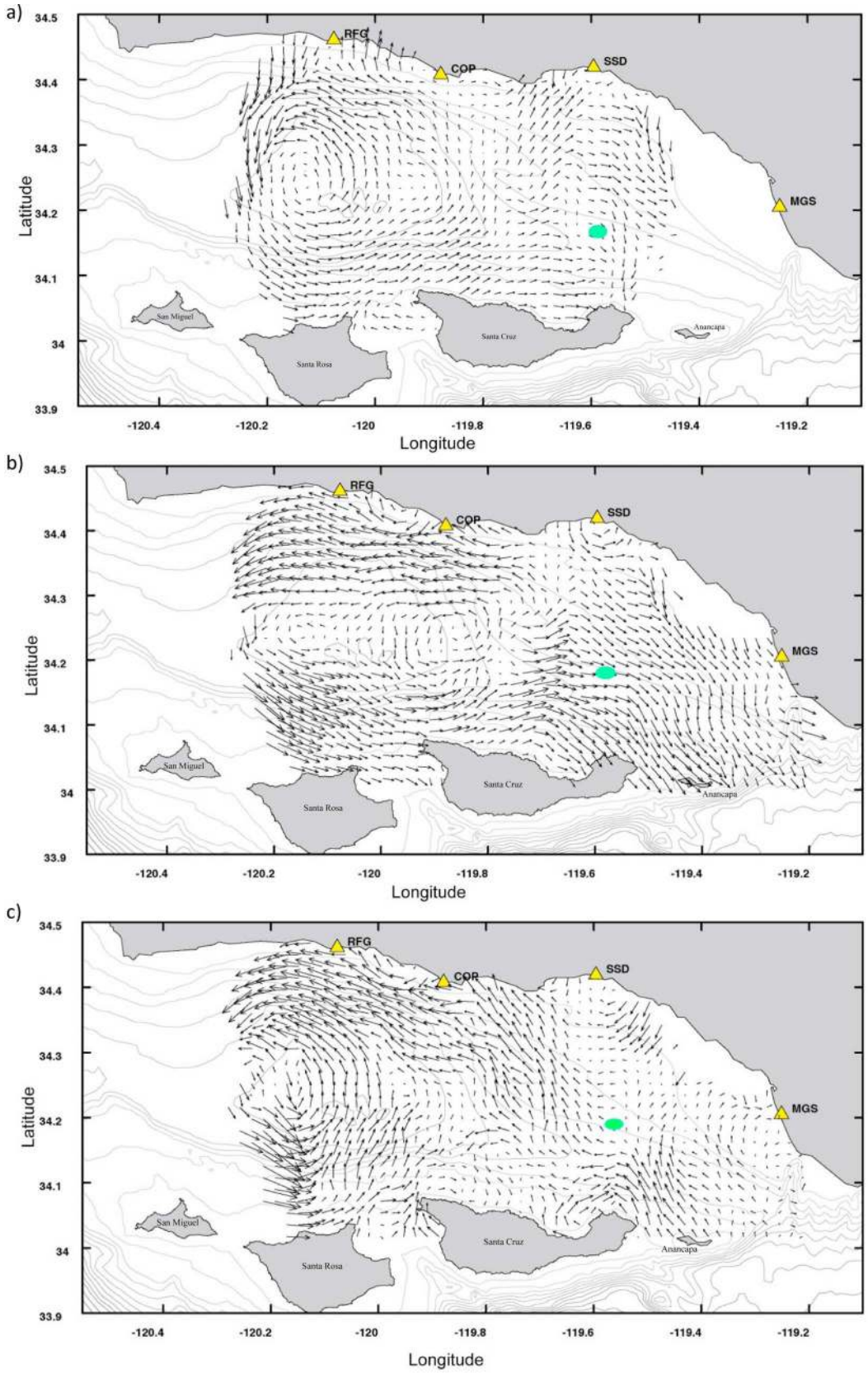

Figure 9. HF surface current data sequence. Only data collected on (a) 12 September 2008 (YD 256), (b) 19 September 2008 (YD 262), and (c) 23 September 2008 (YD 266) are shown here. Complete daily sequence may be viewed on website www.opl.ucsb.edu/radyo. The green symbol marks the location of R/P *FLIP* during the experiment and the yellow triangles indicate the locations of HF radar sites.

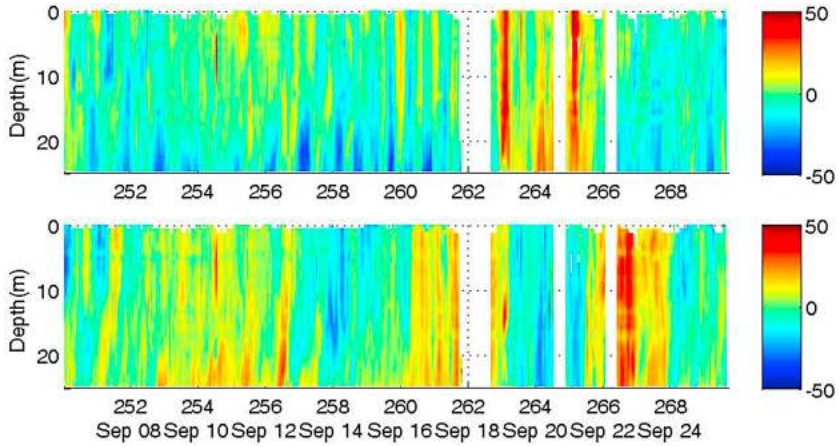

Figure 10. Contour plots of currents: (top) U and (bottom) V, both in cm/sec for depths of ~1–25 m using the SIO uplooking ADCP.

the north of Santa Rosa and Santa Cruz Islands intensified (Figure 9b). The mean surface currents were 9.3 cm eastward and 2.2 cm/sec northward. The increased mean speeds and directional shifts may have been caused by the significant increase of wind speeds. Unfortunately, there is a data gap in the R/P *FLIP* ADCP record on 18 September (YD 262). However, currents in the upper 20 m appear to be fairly coherent with depth.

[86] The final period of the experiment, 20–23 September (YD 264–267) was marked by the weakest wind-forcing. The surface current patterns suggested a transitional flow regime as the flow changed direction from generally eastward to westward through the east end of the SBC (Figure 9c). The flow pattern in the vicinity of the experimental site on 22 September (YD 266) shows very weak surface currents; however fairly strong northward surface currents developed to the east of the site. Inspection of the complete sequence of current images suggests the possibility of a submesocale eddy developing and propagating westward in the eastern portion of the SBC. The mean surface currents at the site for the final period were 2.5 cm/sec eastward and 4.4 cm/sec northward, consistent with the flow pattern of Figure 9c. Perhaps because of the transitory surface currents, the directions of currents at the RaDyO site were highly variable: southward on 20 September (YD 264), near zero on 21 September (YD 265), strong toward the north on 22 September (YD 266), and strong toward the north-northeast on 23 September (YD 267). Again, the R/P *FLIP* ADCP data indicate coherent current structure with depth (Figure 10). R/P FLIP and other ADCP data agree at 17 m.

[87] As explained by *Harms and Winant* [1998], the observed surface currents of the SBC are thought to result from the additive effects of a larger-than-SBC scale flow and a cyclonic circulation within the SBC itself. They presented synoptic views of SBC circulation to include the following regimes: upwelling, relaxation, cyclonic, propagating cyclones, flood east, and flood west. The HF radar data collected for our experiment appear to best conform to the cyclonic model and perhaps the propagating cyclones model toward the end of the experiment. Finally, the strong diurnal (land-sea breeze) forcing and tides played significant roles in the current variability within the SBC and at the site as well. More details concerning the circulation within the SBC are presented by *Dong et al.* [2012].

3.1.2.2. Distributions and Evolutions of Physical and Optical Properties

[88] The distributions of physical and optical properties and their evolution during the SBC experiment are considered next by examining available satellite images and the R/V *Kilo Moana* and R/P *FLIP* data collected at the SBC RaDyO site. One of the challenges is to distinguish the variability at the site according to localized forcing versus advection. Thus, meteorological and current data are needed to assist in interpretation. Clearly, fully 3-dimensional modeling of the SBC for the experiment will enable more detailed testing of hypotheses and identifying the most relevant processes and quantifying their scales [e.g., *Dong et al.*, 2012].

[89] As discussed earlier, the large-scale forcing and oceanographic response along the northern and central California coast during our experiment was dominated to a large degree by generally along-coast (generally toward the southeast) upwelling favorable winds. This is evident in the MODIS sea surface temperature and QuikSCAT wind satellite data shown in Figure 5. Wind shadowing by landmass extends southeastward of Point Conception and explains much of the variability in the sea surface temperature maps with warmer waters extending along the California coast south and east of the SBC. In fact, the SBC is a transitional region where cool upwelled waters often enter the west end of the SBC and warm waters move into it from the east end. Consequently, the SBC is typically characterized by complicated flows and hydrography as well as optical property distributions with the occurrence of eddies and fronts of varying scales as discussed in the previous section.

[90] The site of RaDyO, which is in the eastern portion of the SBC, appears to have been in a relatively quiescent location with respect to currents. However, about one third of the way through the experiment, local peak daily winds roughly doubled. Examination of the HF radar surface current maps (Figure 9) also suggests a change in the flow regime at the site with apparent intensification of a current north of the Channel Islands. Again, this flow appears to

have extended to the RaDyO site and may partially explain some of the observed changes in physical and optical properties described below.

[91] Time-depth contours of temperature, salinity, density (σ_t), and stratification are shown in Figure 11. The upper layer temperatures were relatively warm and the mixed layer depth was around 15 m through about 17 September (YD 260). There was significant diurnal variation in the mixed layer depth (MLD) as forced primarily by a strong land-sea breeze signal and secondarily the daily cycle of surface heating and cooling. The thermocline extended downward from the base of the mixed layer by about 15–20 m for the first period of wind-forcing. The strong winds initiated around 16 September (YD 260) appear to have resulted in deepening of the mixed layer to about 25 m, cooling of the surface layer waters, and sharpening of the thermocline and pycnocline for about 2 days after which the mixed layer shoaled to values of ~10 m, even less than those observed at the beginning of the experiment.

[92] The general optical properties of the SBC have been reviewed and analyzed in considerable detail by *Toole and Siegel* [2001] and *Kostadinov et al.* [2007]. Optical properties of the SBC, which are affected by chlorophyll *a*, are correlated to a large extent with eastward advection of upwelled (cooler (Figure 5), nutrient rich) waters from off Point Conception as suggested by the satellite color images (MODIS) shown in Figure 12. South and east of the Southern California Bight (SBC) and generally within the more wind-sheltered portion of the SCB, much lower values of chlorophyll *a* and warmer waters prevail, so when flow through the SBC is influenced more by westward flow, the chlorophyll *a* levels decrease. The SBC is in essence a biological as well as physical transition region between cooler, more nutrient rich, and more biologically productive waters coming from the Point Conception area to the west and the warmer, less productive waters of the SCB to the south and east. There are often east–west and north–south gradients in chlorophyll *a* and temperature because of the prevailing current patterns. Although the spatial resolution of the satellite color images shown here is not great, there do appear to be larger concentrations of surface chlorophyll *a* within the eddy centered near the deepest portion of the SBC and to the west of the RaDyO study site (Figure 12). Similar observations of higher chlorophyll *a* levels associated with such basin-scale eddies that can extend to at least 200 m depth have been reported by *Nishimoto and Washburn* [2002], *Anderson et al.* [2006], and *Anderson et al.* [2008]. It is thought that these eddies are convergent and lead to high levels of chlorophyll *a* and fish stocks. There appear to be submesoscale eddies within the SBC as well [*Beckenbach and Washburn*, 2004; *Dong et al.*, 2012] and these too may have a major influence on chlorophyll *a* distributions and optical properties in general [e.g., *Bassin et al.*, 2005].

[93] Time series of dissolved oxygen, chlorophyll *a*, and beam attenuation coefficient are displayed as functions of depth in Figure 11. Dissolved oxygen is relatively uniform in the upper 40–65 m with some apparent influence by the increased winds during the period of 16–20 September (YD 260–264). The maximum vertical gradient in dissolved oxygen lags that of the MLD by about 1 day. The chlorophyll *a* maximum layer generally resides just below the mixed layer, but there are some significant departures. The most impressive feature occurs between depths of about 10 and 40 m around 20–22 September (YD 264–266). The origin of this high chlorophyll *a* feature is not certain. It is possible that it may have resulted from advection as there was a change in current patterns around this time. However, another possibility is that the prior wind event may have been sufficient to cause entrainment of some of the subsurface chlorophyll *a* maximum waters and more nutrient rich waters from depth, thus possibly stimulating a phytoplankton bloom with a time lag of a couple of days.

[94] The beam attenuation coefficient data show higher values within and just below the mixed layer, but these fall off quickly below for the first two periods of the experiment. However, similar changes as those noted for chlorophyll *a* occur around 20–22 September (YD 264–266). In this case, the beam attenuation coefficient maximum lies very near the base of the MLD whereas the chlorophyll *a* maximum was deeper by about 10 m. Whether this feature was caused locally or resulted from advection will be explored by analyzing data collected by the *Odyssey* AUV and the *REMUS* AUV [*Moline et al.*, 2012] and by using general circulation models [e.g., *Dong et al.*, 2012].

4. Background for the Hawaiian RaDyO Study

[95] The Hawaiian RaDyO study region lies in the subtropical North Pacific gyre. The clockwise wind pattern of the subtropical North Pacific gyre has been documented in several studies [e.g., *Hellerman and Rosenstein*, 1983]. The specific region of the Hawaiian RaDyO study was approximately 17.5 to 18.0 N, 155.5 to 160.0 W (Figure 13). The wind patterns here generally vary from northeasterly to easterly (Figure 14) and display some seasonality with maximum trade winds occurring in summer months and more moderate winds during winter.

[96] The clockwise circulating oceanic gyre is driven by these winds. The wind stress curl is particularly important for the ocean circulation as demonstrated by *Munk* [1950]. The wind-driven currents in the RaDyO study region lie on the southern side of this gyre and are part of the North Equatorial Current (NEC). The surface currents of the NEC are directed predominantly from east to west in latitudes of roughly 10 to 20 N and thus through the RaDyO study site (~17.5–18 N).

[97] The starting point for the RaDyO time series observations from R/P *FLIP* and the accompanying R/V *Kilo Moana* was almost due south of the southernmost tip of the Big Island. R/P *FLIP* was allowed to drift for over 500 km (generally westward) in response to both winds and currents to avoid difficulties in mooring it in deep waters (Figures 13 and 14). The water depth was nominally 4500 to 5000 m. The choice of this study region was based upon desires (1) to do observations in open ocean conditions with strong, persistent winds and long-fetch surface gravity waves, (2) for sampling in clear (Case 1) waters, and (3) for relatively short transit times to the study region for research vessels originating from a major port (i.e., Honolulu). The R/V *Kilo Moana* generally operated within about 1.5 km of R/P *FLIP* once the R/P *FLIP* reached the experimental starting location shown in Figure 13; periodic excursions away from R/P *FLIP* (few kilometers) were required for disposal purposes. The R/V *Kilo Moana* began sampling at R/P *FLIP*'s

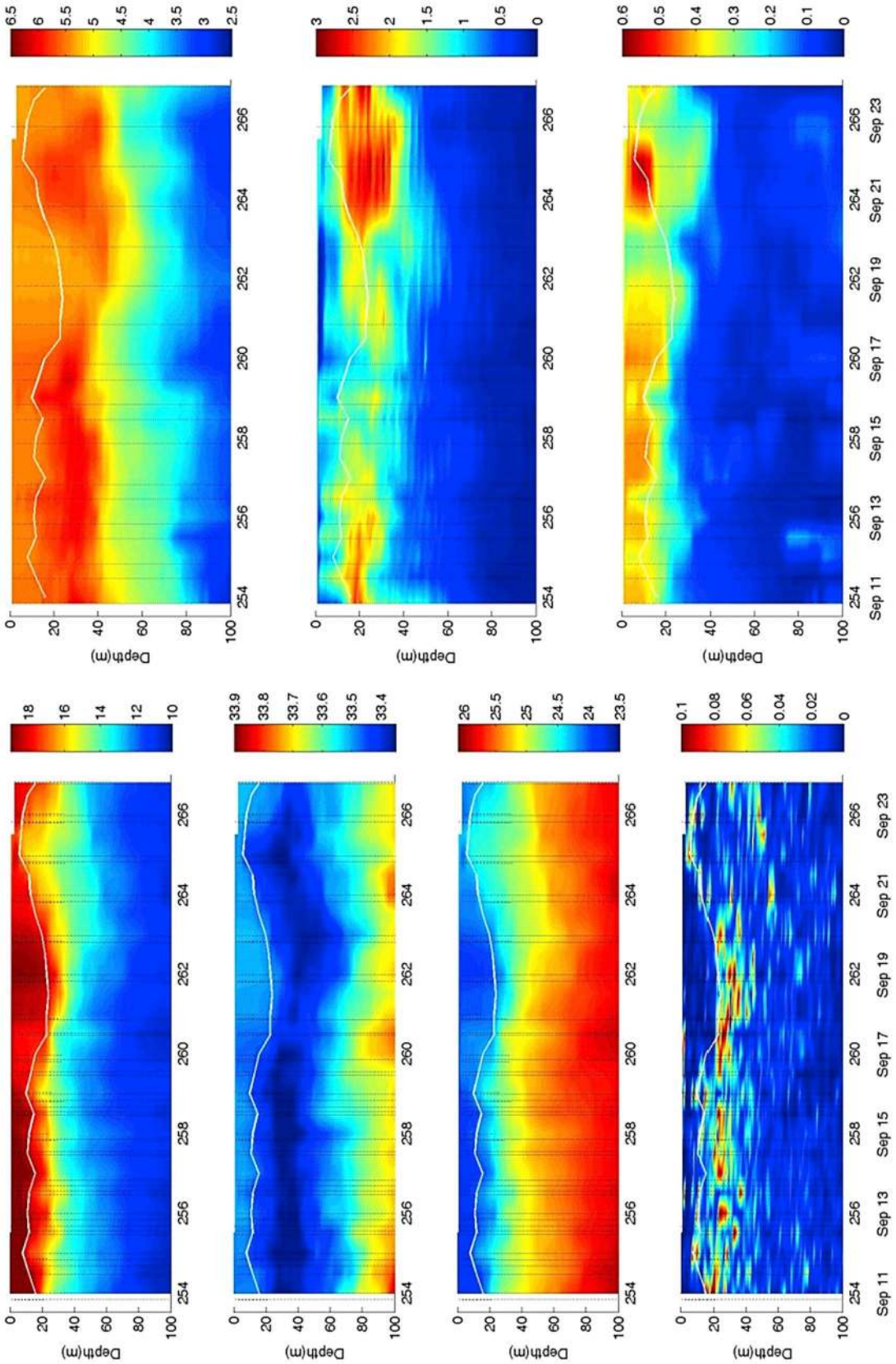

Figure 11. (left) Time-depth contour plots of temperature, salinity, σ_t, and stratification using data collected with the R/V *Kilo Moana* and MASCOT CTDs to 100 m depth. Depth of the mixed layer based on a 0.5°C criterion is also displayed in white curves. (right) Same as Figure 11, left, for dissolved oxygen in ml/l, chlorophyll *a* in mg/m^3, and beam c_{pg} (at 650 nm) in m^{-1} to 100 m depth.

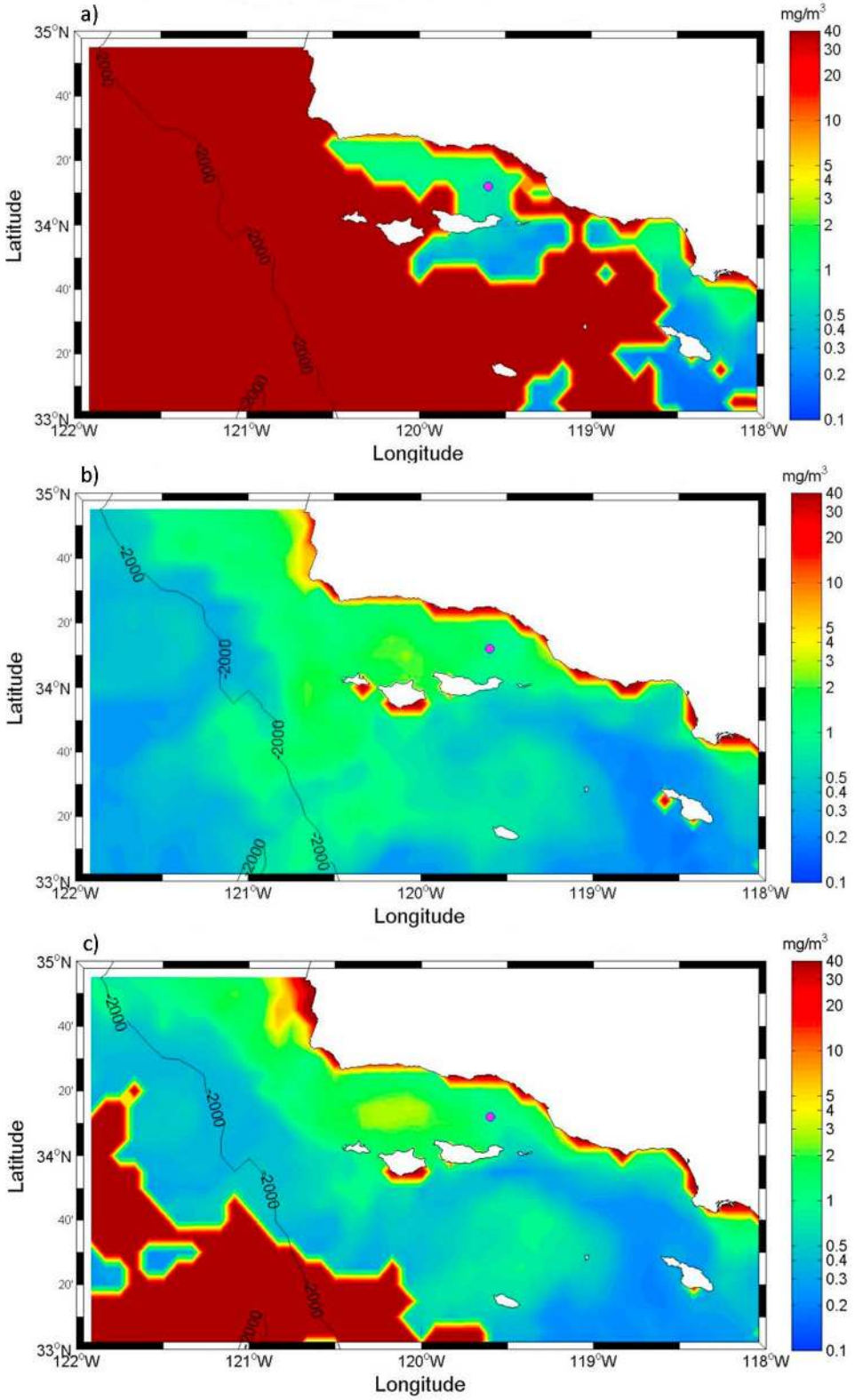

Figure 12. Satellite color images indicating surface distributions of chlorophyll *a* from north of Point Conception and within the Southern California Bight for the periods of (a) 5–12 September 2008 (YD 249–256), (b) 13–21 September (YD 257–264), and (c) 22–29 September (YD 265–272).

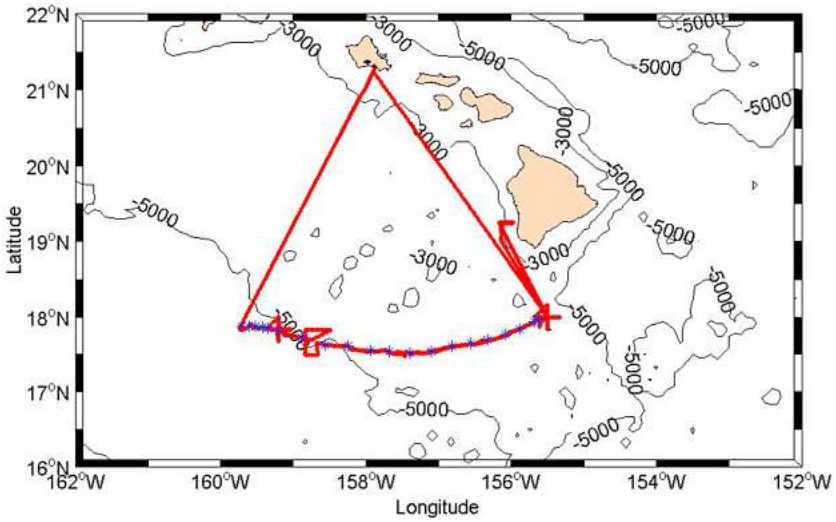

Figure 13. Map showing positions of the R/P *FLIP* and R/V *Kilo Moana* during the Hawaii RaDyO experiment from 30 August to 15 September 2009 (YD 242–258). R/P *FLIP* was allowed to drift and the R/V *Kilo Moana* was positioned near R/P *FLIP* for most of the experiment.

approximate starting point (where it was flipped into vertical position) on YD 242 (30 August 2009) and its sampling ended on YD 258 (15 September 2009). R/V *Kilo Moana* measurements made before YD 242 (30 August 2009) were done in transit or during a diversion for measurements at a location in the lee of the Big Island. Primary R/P *FLIP* time series span the period of approximately YD 244 (1 September 2009) through YD 257 (14 September 2009). The *REMUS* AUV was also deployed from the R/V *Kilo Moana* on YD 243, 247, and 248 (31 August and 4 and 5 September 2009) in order to obtain horizontal spatial variability data as well as to obtain a unique view of the ocean environment [*Moline et al.*, 2012]. Satellite wind, sea surface temperature (Figure 15) and ocean color data (Figure 20) provided regional atmospheric and oceanographic context for the study.

4.1. Results for the Hawaiian RaDyO Study

4.1.1. Atmospheric Conditions

[98] The atmospheric conditions for the Hawaii experiment were documented using satellite and in situ measurements from the R/V *Kilo Moana* and the R/P *FLIP* in a similar fashion to that of the SBC experiment and with the same general motivations and objectives. First, we focus only on the wind conditions for context as details concerning other meteorological observations are presented in *Zappa et al.* [2012] and Melville et al. (manuscript in preparation, 2012).

[99] The well-documented, steady trade winds of the region prevailed during the Hawaii RaDyO experiment as evidenced by satellite QuikSCAT data for the periods of YD 241–248, 249–256, and 257–264 (29 August to 21 September 2009; Figure 15). Wind direction time series data collected from the R/V *Kilo Moana* (Figure 16) and R/P *FLIP* (Figure 17) also confirm the trade wind pattern with winds generally from the east (shown in Figure 16 as toward the west with a mean of 261 deg). Interestingly, the direction of drift of R/P *FLIP* began generally eastward with a modest component to the south (Figures 13 and 14). About halfway through the drifting portion of the experiment, it took a course still to the east, but with a slight northward component (Figures 13 and 14). Careful inspection of the QuikSCAT images (Figure 15) shows that there was some spatial

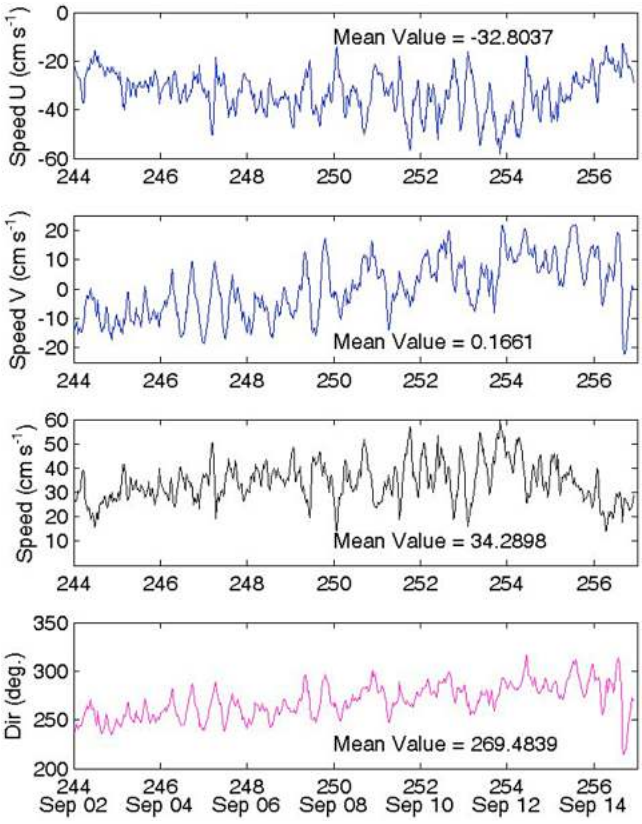

Figure 14. (top to bottom) Time series of the R/P *FLIP* drift speed by components (U and V), magnitude, and direction during the Hawaii experiment. 30 min averages were used.

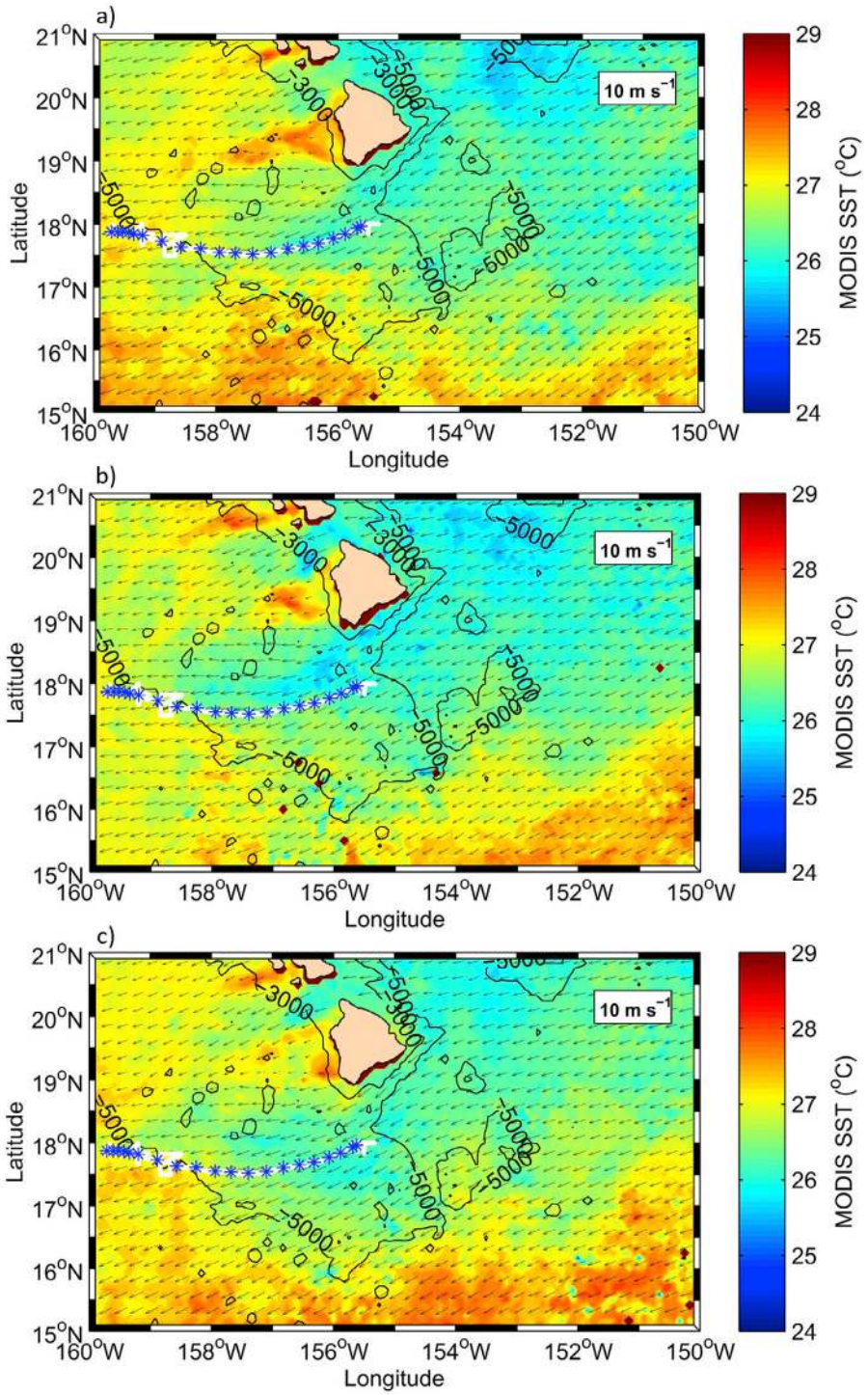

Figure 15. Satellite wind vectors (QuikScat) and sea surface temperature (MODIS) images for the periods of (a) 28 August to 5 September (YD 241–248), (b) 6–13 September (YD 249–256), and (c) 14–21 September (YD 257–264). The westward trajectory of R/P *FLIP* during the experiment is indicated by the white line and blue asterisks.

variability in the wind field over the drift region, which may account at least in part for the R/P *FLIP*'s slight change in direction as R/P *FLIP*'s drift is controlled by both winds and currents. The mean direction of R/P *FLIP*'s drift was toward 269 deg, which is very close to the mean wind speed direction toward 261 deg.

[100] Time series of wind speed collected by R/V *Kilo Moana* while in the lee of the Big Island and before its rendezvous with R/P *FLIP* clearly showed the island shadowing effect as did the QuikSCAT wind data. The time series of wind speed and direction data collected from R/V

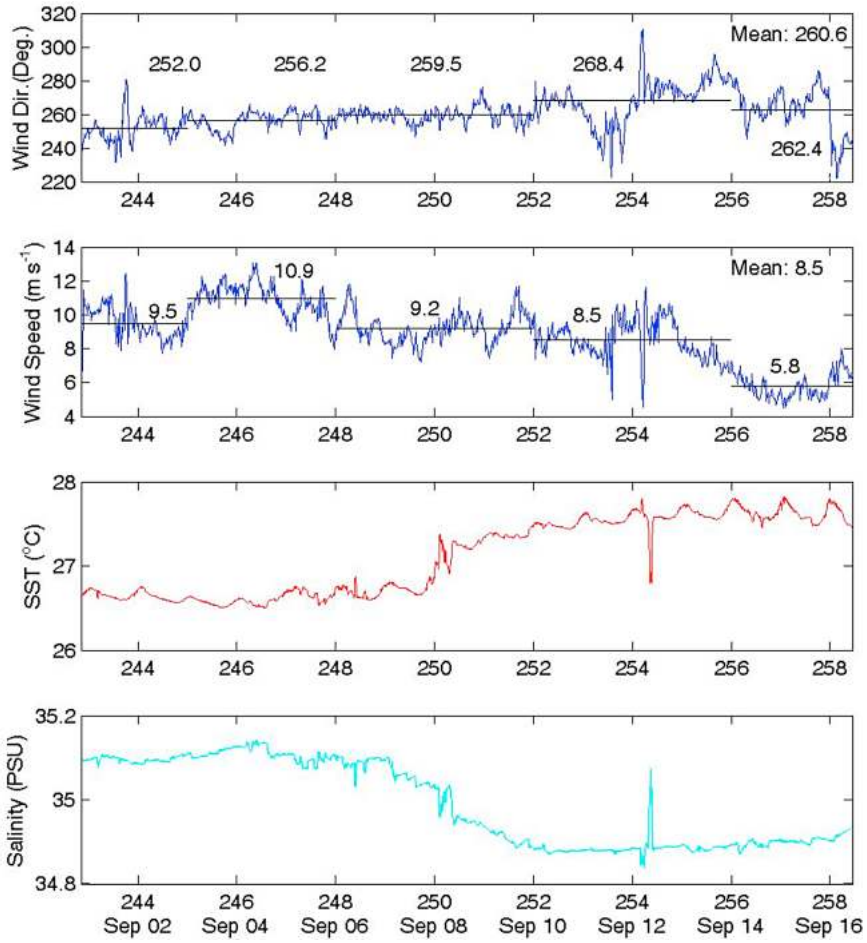

Figure 16. (top to bottom) Time series of R/V *Kilo Moana* wind direction (winds 'toward' convention is used) and wind speed, surface temperature, and surface salinity. Means for wind direction and speed are shown for five time periods and for the entire experiment.

Kilo Moana and R/P *FLIP* during the concurrent sampling programs show that although the direction is quite steady (generally out of the east and toward the west), there is considerable variability in wind speed with peak winds of about 12 m/sec occurring during YD 246 (3 September) as seen in Figure 16. For convenience, we have computed average wind speeds for five periods: YD 243–245 (31 August to 2 September): 9.5 m/sec; YD 245–248 (2–5 September): 10.9 m/sec; YD 248–252 (5–9 September): 9.2 m/sec; YD 252–256 (9–13 September): 8.5 m/sec, and YD 256–258 (13–15 September): 5.8 m/sec (Figure 16). The average wind speed for the entire record was 8.5 m/sec with a standard deviation of 2.6 m/sec. After the first few days, wind speed increased and leveled off before decreasing and generally leveling off again. Interestingly, the peak wind speeds for the Hawaiian experiment were very similar to those observed during the SBC experiment (compare wind speed data in Figure 16 with those in Figure 6). However, the experimental period wind speed average for the Hawaii experiment was 3.3 m/sec greater than that of the SBC experiment. Both display diurnal signals, though considerably less so for the Hawaiian experiment. Figure 17 shows the summary of the atmospheric conditions for the Hawaiian experiment. Diurnal cycles in the wind speeds and wave heights are evident for the duration of the experiment. More detailed meteorological discussions may be found in *Zappa et al.* [2012] and Melville et al. (manuscript in preparation, 2012).

4.1.2. Oceanographic Conditions

[101] The principal scales of interest for the Hawaiian experiment were within approximately 1.5 km radial distance of the R/P *FLIP*. Next, we describe the general oceanographic conditions in the study area from approximately YD 242 through YD 258 (30 August to 15 September 2009). First, the current results are presented and then the physical and optical data are reported.

4.1.2.1. Currents

[102] Again, R/P *FLIP* drifts in response to wind and current forcing. The relative contributions of the two factors cannot be directly determined. However, for the present experimental region, the winds and currents historically are generally directed toward the west. R/P *FLIP*'s drift followed a westward course close to that of the mean winds (Figures 13, 14, 15, and 16). R/P *FLIP*'s drift speed by components, magnitude, and direction are shown in Figure 14. About halfway through the experiment, there is a shift from a slight southward component to a modest northward component with an experimental mean northward

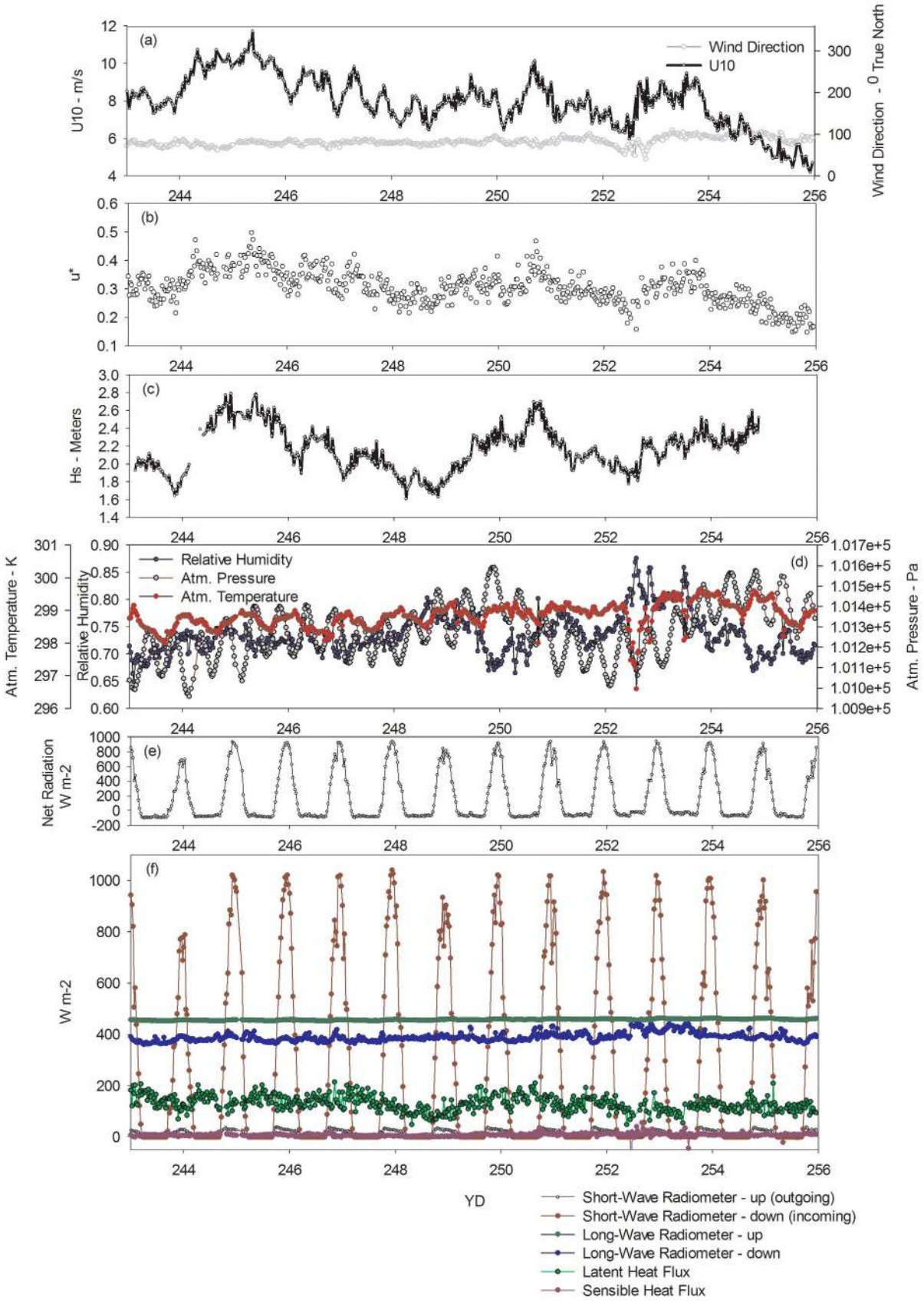

Figure 17. Environmental conditions during the Hawaii Experiment, September 2009, recorded from R/P *FLIP* (Melville et al., manuscript in preparation, 2012). Note the correlation between the wind speed, friction velocity from the eddy flux measurements, and the wave height over the course of the experiment.

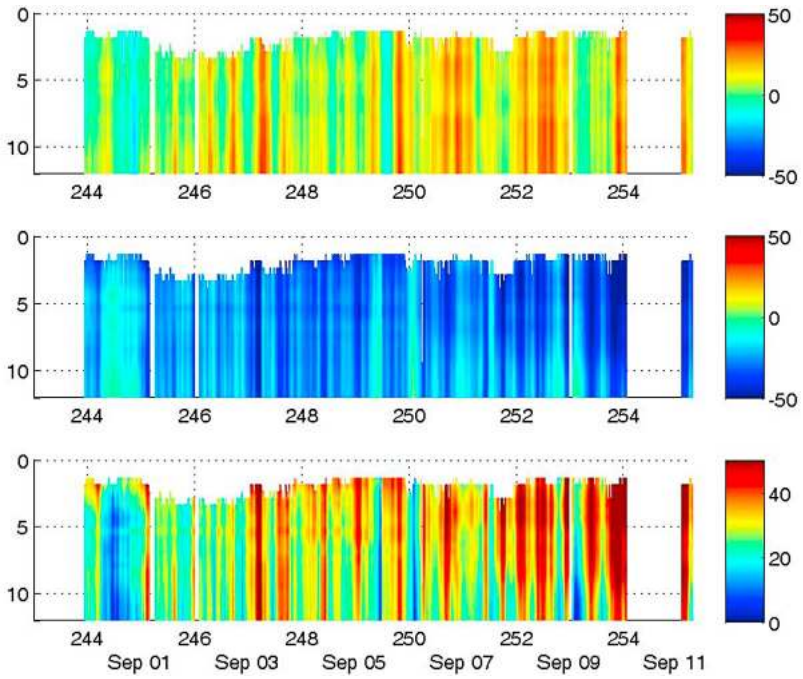

Figure 18. Contour time series of R/P *FLIP* ADCP velocity data ((top to bottom) U-component, V-component, and speed) in the upper 12 m. All velocities are in cm/sec.

component of less than 0.2 cm/sec. The mean drift speed for the experiment is 34.3 cm/sec toward 269 deg.. This speed is somewhat greater than historical reports of mean flow, probably because of the added effect of wind on FLIP.

[103] Subsurface currents were obtained from an uplooking ADCP mounted at 25 m on the R/P *FLIP* and a downlooking ADCP mounted on the hull of the R/V *Kilo Moana.* Platform drift is included in the computation of the reported currents for both. The R/P *FLIP* data span approximately the upper 12 m of the water column. Current time series for depths of 5 and 10 m are directed generally westward with some north-south oscillations associated with tidal (primarily semidiurnal) and possibly near inertial motions. Upper ocean current speeds generally increased by a factor of roughly 1.5 to 2.0 during the experiment. The current direction was quite consistently toward the west, but with some variability related to tides as was the case for the R/P *FLIP* drift. The currents in the upper 12 m were generally uniform in speed and direction as suggested by data shown in Figure 18.

[104] R/V *Kilo Moana*'s 300 kHz ADCP current data indicated some vertical shear in the horizontal currents appears near the base of the mixed layer and oscillations associated with tides (Figure 19). The currents measured during our experiment are consistent with those reported by previously investigators, though slightly stronger than those simulated using various numerical models. The most interesting aspect is the shift in currents about midway through the experiment, which may result from a combination of variations in wind-forcing and the movement of our platforms into a different water mass (described below) with a differing current regime.

4.1.2.2. Distributions and Evolutions of Physical and Optical Properties

[105] The spatial variability of sea surface temperature of the region (roughly 17.5–18.0 N, 155.5–160.0 W) of the Hawaiian experiment is illustrated in the MODIS satellite SST data displayed in Figure 15. These maps indicate horizontal spatial variability with SST's roughly in the range of 26–27°C and with slightly warmer (by ~1°C) waters generally lying to the west of approximately 157 W and to the south of the study region. Satellite-based (MODIS) chlorophyll *a* concentration distributions are shown for approximately the same periods in Figure 20. There was considerable cloud cover negating observations of large areas, however the influence of the archipelago is evident with higher chlorophyll *a* concentrations in the wind lee of the islands as expected based on earlier experiments including E-FLUX. These satellite data reflect only near-surface conditions and subsurface spatial distributions likely differ.

[106] Diurnal oscillations in near-surface temperature of about 0.1–0.2°C (peak-to-peak) are evident by inspecting time series temperature records from R/P *FLIP* (Figures 16 and 21). These records also show relatively steady SST's of about 26.3°C from YD 242 (30 August) until YD 250 (7 September), increasing SST's from this point until about YD 253 (10 September) when SST's reach about 27.3°C, with only modest change until the end of the experiment on about YD 258 (15 September). The shift appears to be caused by regional water mass variability, as based on the satellite SST map data, opposed to local forcing at the drifting R/P *FLIP* although the greatest wind-forcing of the experiment occurred prior to YD 250 (7 September) on YD 246 (3 September). Water mass change is also supported by salinity data obtained from the R/V *Kilo Moana* as

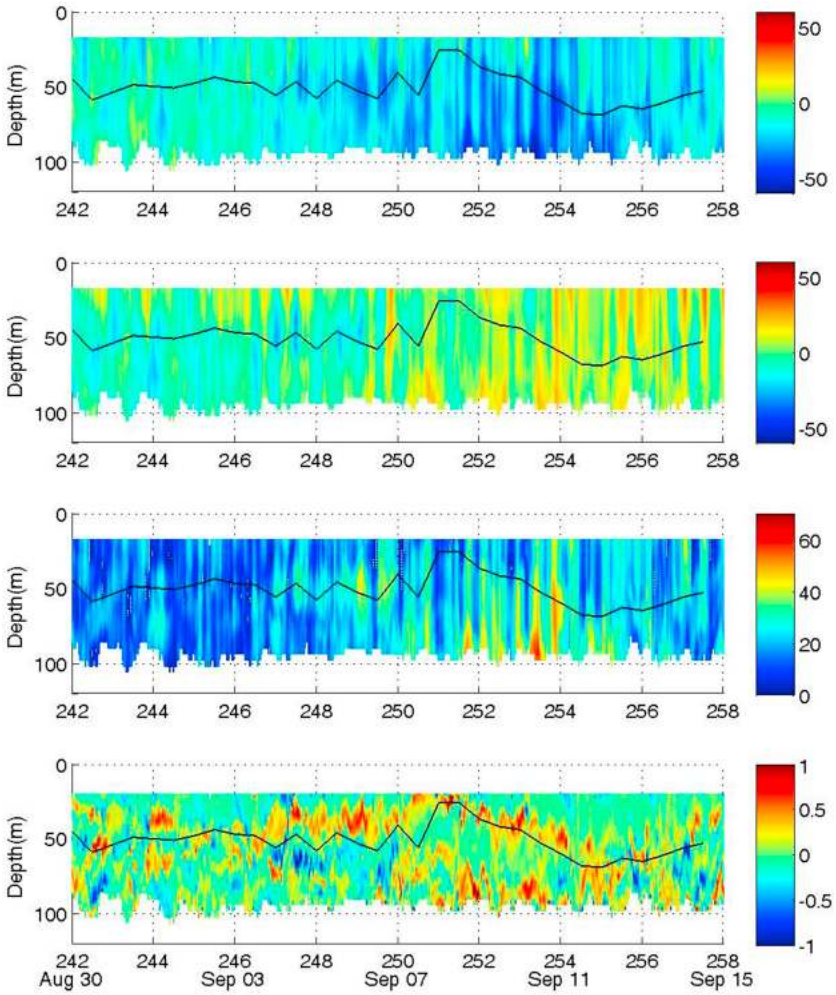

Figure 19. R/V *Kilo Moana* ADCP data from 17 to 100 m. (top to bottom) U-component, V-component, speed, and shear in units of cm/sec/m. The mixed layer depth is indicated with a white line.

salinity makes a transition to lower values (from about 35.10 psu to 34.85 psu at 13 m depth) as temperature increases (Figure 16). Perhaps the most compelling evidence for the water mass transition hypothesis is the TS diagram (for depths of 0–200 m) shown in Figure 22. This figure clearly shows the transition from cooler saltier water masses to warmer fresher water masses from YD 242–250 (30 August to 7 September) to YD 253–258 (10–15 September). Future model simulations should help to sort out the advective versus local effects.

[107] The temperature stack plot (Figure 21) of time series of temperature obtained from sensors mounted on R/P *FLIP* from the surface to 85 m indicates increased stratification from YD 250–253 (7–10 September) as well as some variability at depth, likely related to semidiurnal internal tides, which would be consistent with the semidiurnal variability noted in the current records. Time-depth contour plots of the physical and optical data are illustrated in Figure 23. These plots show some variability with interesting subsurface transitions occurring around YD 250–253 (7–10 September) with a shoaling of the mixed layer followed by deepening. Changes in the structures and magnitudes of subsurface chlorophyll *a* and beam attenuation coefficient are also evident. Since the water mass differences are readily apparent before and after the transition period of YD 250–253 (7–10 September), we have also plotted in Figure 24 the vertical structure of temperature, salinity, density, chlorophyll fluorescence, beam attenuation coefficient, and dissolved oxygen as average profiles for the periods of YD 242–250 (30 August to 7 September) and YD 253–258 (10–15 September). This figure provides a means of summarizing the apparent water mass transition in the upper 200 m as follows: (1) increases in temperature, (2) decreases in salinity, (3) decreases in density, (4) increases in stratification, (5) decreases in chlorophyll *a* to about 150 m, (6) decreases in beam attenuation coefficient from about 20 to 80 m and modest increases from about 150–200 m, and (7) a downward shift in the depth of the dissolved oxygen maximum layer.

5. Preview of Papers in the Special Section

[108] Contributions to this special section are introduced categorically for convenience as follows: (1) observational papers based primarily on results from the RaDyO program, (2) modeling papers done in conjunction with RaDyO, and

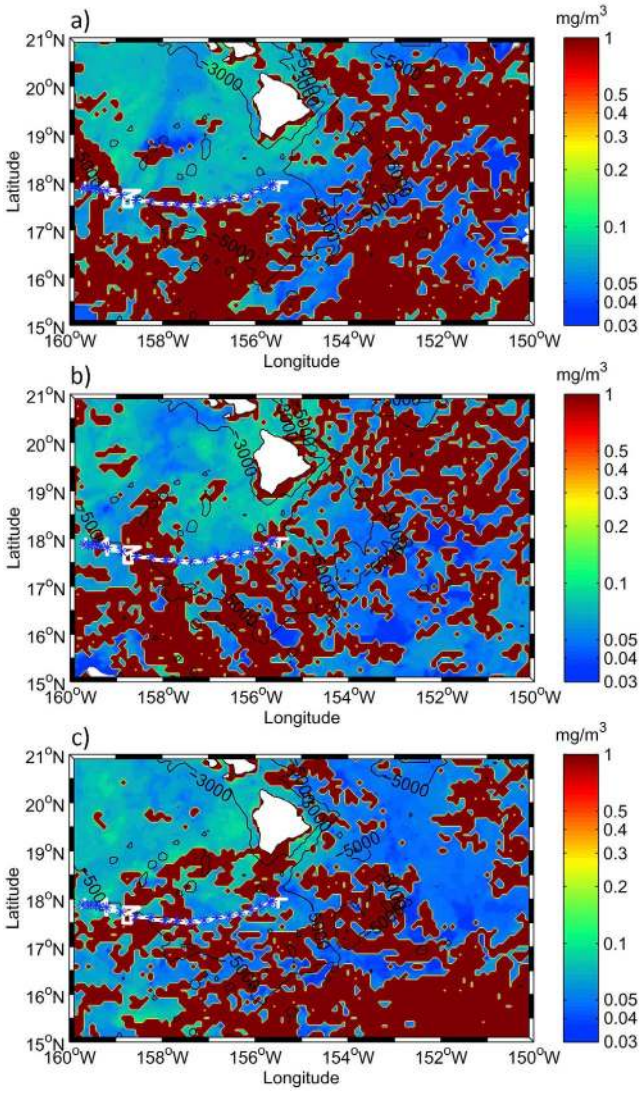

Figure 20. Satellite color images (MODIS) indicating surface distributions of chlorophyll for the Hawaiian study region for the periods of (a) 28 August to 5 September (YD 241–248), (b) 6–13 September (YD 249–256), and (c) 14–21 September (YD 257–264). The westward trajectory of R/P *FLIP* during the experiment is indicated by the white line and blue asterisks.

(3) papers relevant to the theme of the special section that were submitted by authors independently of RaDyO.

5.1. RaDyO Observational Papers

[109] One of the goals of RaDyO was to comprehensively observe and document the environmental conditions under which RaDyO optical observations were made as described above. Such observations are necessitated in part by the desire to model radiative transfer across the air-sea boundary. To do so requires the detailed characterization of the sea surface roughness and sea surface slopes on the microscale. To this end, specialized atmospheric and sea state observations including air-sea fluxes and surface topography (including slopes) for the RaDyO field experiments in the Santa Barbara Channel and in the open ocean waters south of Hawaii are described by *Zappa et al.* [2012] and Melville et al. (manuscript in preparation, 2012). *Zappa et al.* [2012] have described and utilized new measurement capabilities for surface roughness and report physical data pertinent to basic optical distortion processes related to the air-sea interface. Highlights of their work include the application of a new polarimetric imaging camera; this technique has revealed a complex interaction of wind and surface currents affecting surface roughness. Additionally, they have reported that breaking crest length spectral density is modulated by the development of the wavefield (i.e., wave age) as well as the alignment of wind and surface currents at the scale of wave breaking. Melville et al. (manuscript in preparation, 2012) describe the impact of wave breaking and near-surface turbulence on imaging through the ocean surface, finding that laboratory simulations of these processes are representative of field data from the three field experiments.

[110] RaDyO investigators report several advances in capabilities to observe optical variability as affected by diverse factors and quantified through several variables on fine space and time scales as well as spectral resolution. Several examples of these advances and their application to near-surface optical variability follow.

[111] *Twardowski et al.* [2012] utilized their recently developed MASCOT system to measure the effects of particles and bubbles on the optical volume scattering function (VSF) in the surf zone off Scripps Pier during the initial RaDyO field exercise. They report how the optical phase function was affected by passing suspended sediment plumes and wave-injected bubble plumes. Measured VSFs were used to determine particle size distributions and compositions. Their inversion method results for these data sets showed qualitative agreement with concurrent acoustical measurements of bubbles and aggregate particle size distributions.

[112] Unique measurements of bubble size distributions using simultaneous acoustical and optical instrumentation are further described by *Czerski et al.* [2011]. While acoustical measurements of larger bubbles have been made during many studies, much less work has been done to measure bubbles with radii smaller than about 30 μm. These are thought to be extremely important for optical properties and radiative transfer in the upper ocean, but it is not straightforward to extend acoustical measurements to these smaller sizes. To our knowledge, *Czerski et al.* [2011] report the first use of simultaneous acoustical and optical observations to constrain bubble coating parameters. Their principal findings are that organic coatings of the bubbles are relevant for both acoustical and optical measurements and that the inferred bubble coatings (with a thickness of around 10 nm) are important for optical inversions.

[113] With growing interest in bubble influences on ocean optics, RaDyO investigators studied the interplay between upper ocean turbulence and varying bubble size distributions. In particular, *Vagle et al.* [2012] conducted simultaneous measurements of upper ocean heat fluxes, turbulence, and bubble size distributions from R/P *FLIP* south of Hawaii. They found that turbulent dissipation rates were reduced by up to a factor of ten during times of large downward heat fluxes (>400 W m^{-2}). *Vagle et al.* [2012] conclude that such reductions can cause decreased concentrations of large

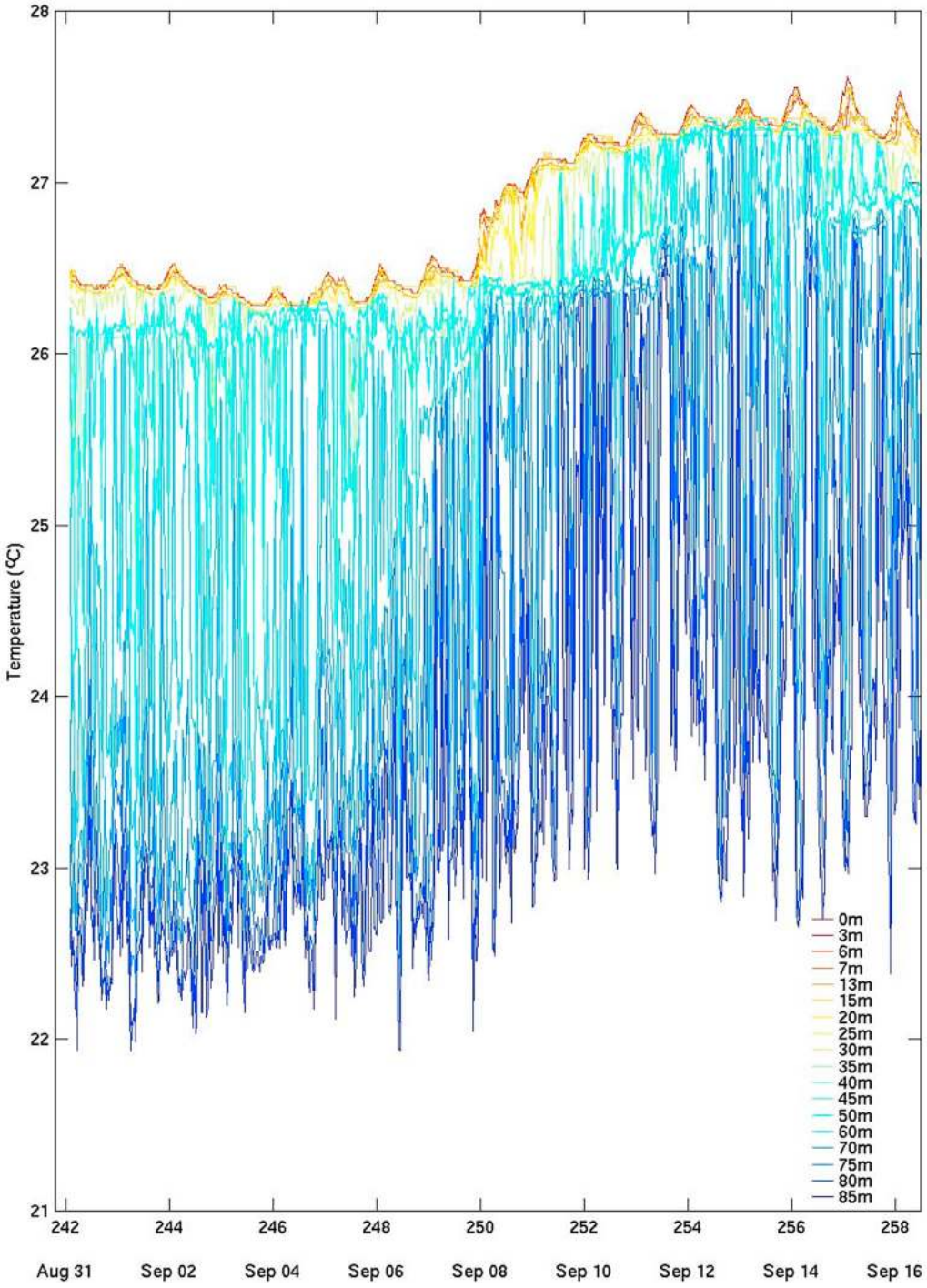

Figure 21. Temperature time series for data collected from R/P *FLIP* sensors placed at 18 depths between the surface and 85 m.

bubbles and decreases of the effect of the bubble field on optical reflectance by up to a factor of ten.

[114] The sea-surface microlayer (SML) has been studied intensively by *Wurl et al.* [2011] in diverse oceanic environments. They have specifically examined the production and fate of transparent exopolymer particles (TEP), which have been shown to have significant influences on light propagation near the air-sea interface. Their work reinforces consensus on the gelatinous nature of the SML, which influences microbial life, surface wave properties, and light propagation. Finally, they describe a conceptual model of TEP cycling, which suggests the importance of abiotic particle aggregation for TEP production in the ocean and that the SML plays a major role in the marine carbon cycle.

[115] High-frequency measurements of the underwater light field from theUnderwater Porcupine Radiometer System are reported by *Darecki et al.* [2011]. This system, which measures downwelling light at up to 1 KHz using an

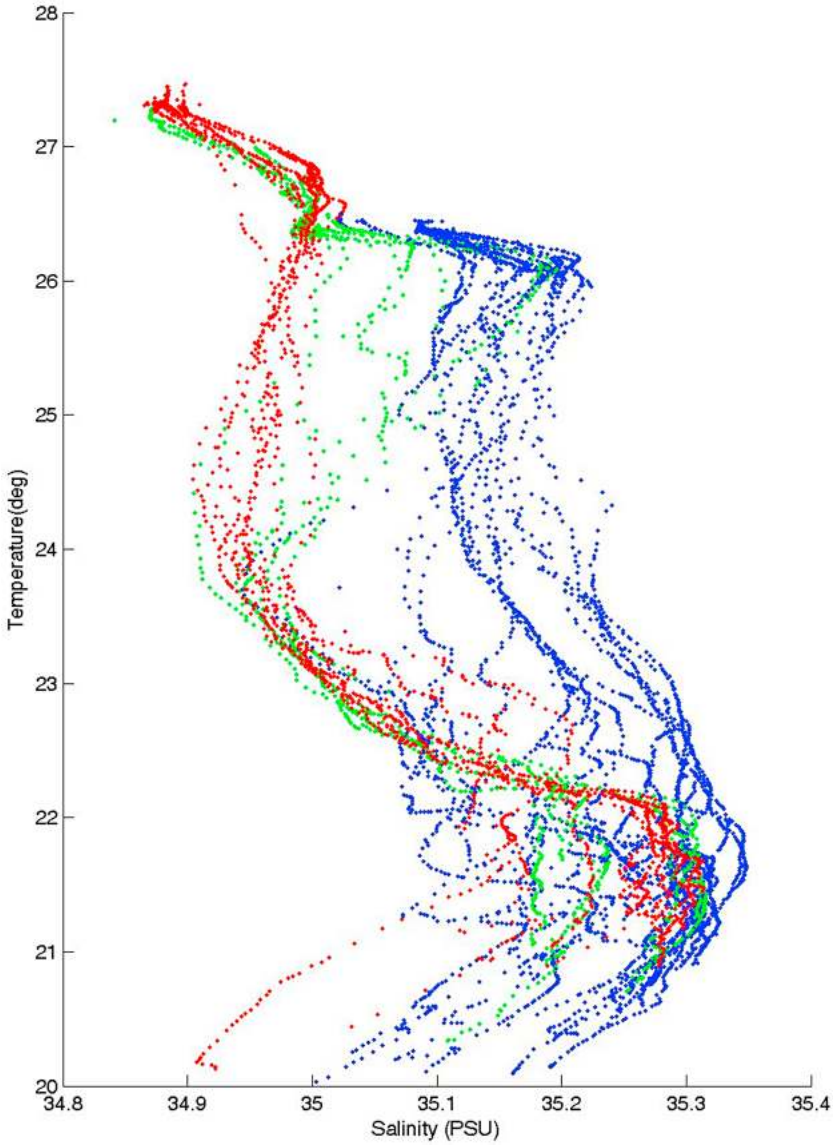

Figure 22. Temperature-Salinity (T-S) plot of R/V *Kilo Moana* CTD data collected from the surface to 150 m. The color coding indicates blue for data collected between YD 242 and 250, green for data collected between YD 250 and 253, and red for the period of YD 253 to 258.

array of 23 radiometric sensors, was used to determine that irradiance collectors of a few millimeters in diameter or less are required to adequately sample observed light flashes resulting from wave focusing. *Darecki et al.* [2011] have shown that some of the brightest light flashes, which can have durations of milliseconds to tens of milliseconds, can be an order of magnitude greater than time-averaged irradiance values. They conclude that intensities of light flashes decrease rapidly as a function of depth and that intensities at longer visible wavelengths are greater than those at shorter wavelengths. Related work by *Gernez et al.* [2011] focused on vertical variability of probability distributions of downward irradiance near the ocean surface under sunny skies. They utilized time series measurements of fluctuations in the underwater downward irradiance at 532 nm (green light) to quantify the nature of the probability distributions of instantaneous irradiance. It was shown that light flashes near the ocean surface result in highly skewed and heavy tailed probability distributions because of surface wave focusing. They suggest several probability distribution models that may be suitable for describing these skewed distributions. At greater depths (e.g., ~10 m for their observational situation) the probability distributions were found to approach a symmetric shape.

[116] During RaDyO, *Lewis et al.* [2011] and *Bhandari et al.* [2011] utilized their newly developed underwater cameras to examine full spherical and polarized downwelling radiance distributions, respectively. The challenges facing these two groups of investigators included the need to measure light intensity changes in response to rapidly changing atmospheric and surface wave conditions over several orders of magnitude in dynamic range. The measurements made by *Lewis et al.* [2011] are noteworthy and valuable in that their fully resolved radiance data can be used to derive all apparent

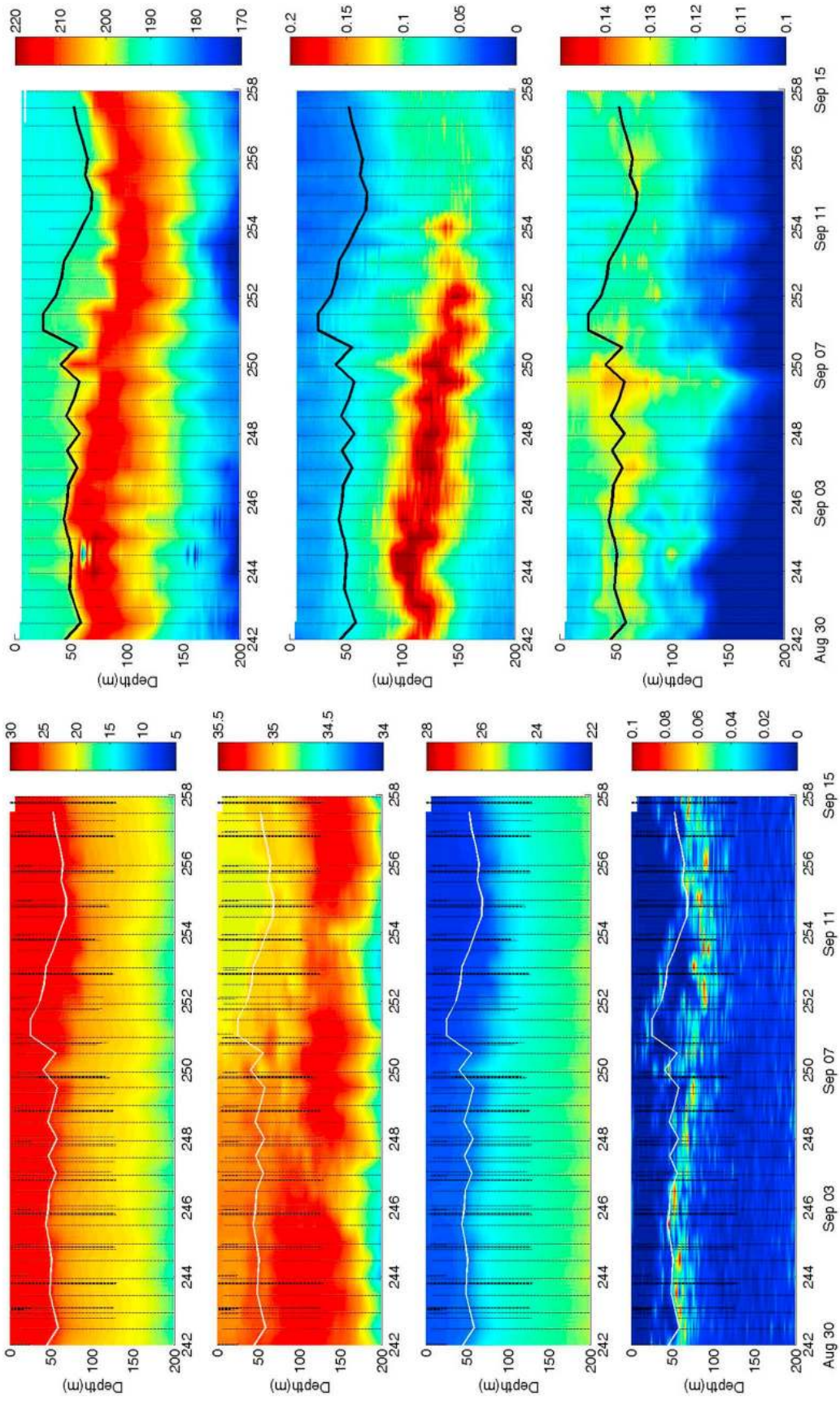

Figure 23. (left) Contour time-depth plots of temperature, salinity, density (σ_t), and stratification, ($d\sigma_t/dz$) to 200 m and (right) dissolved oxygen, chlorophyll a, and beam attenuation coefficient at right.

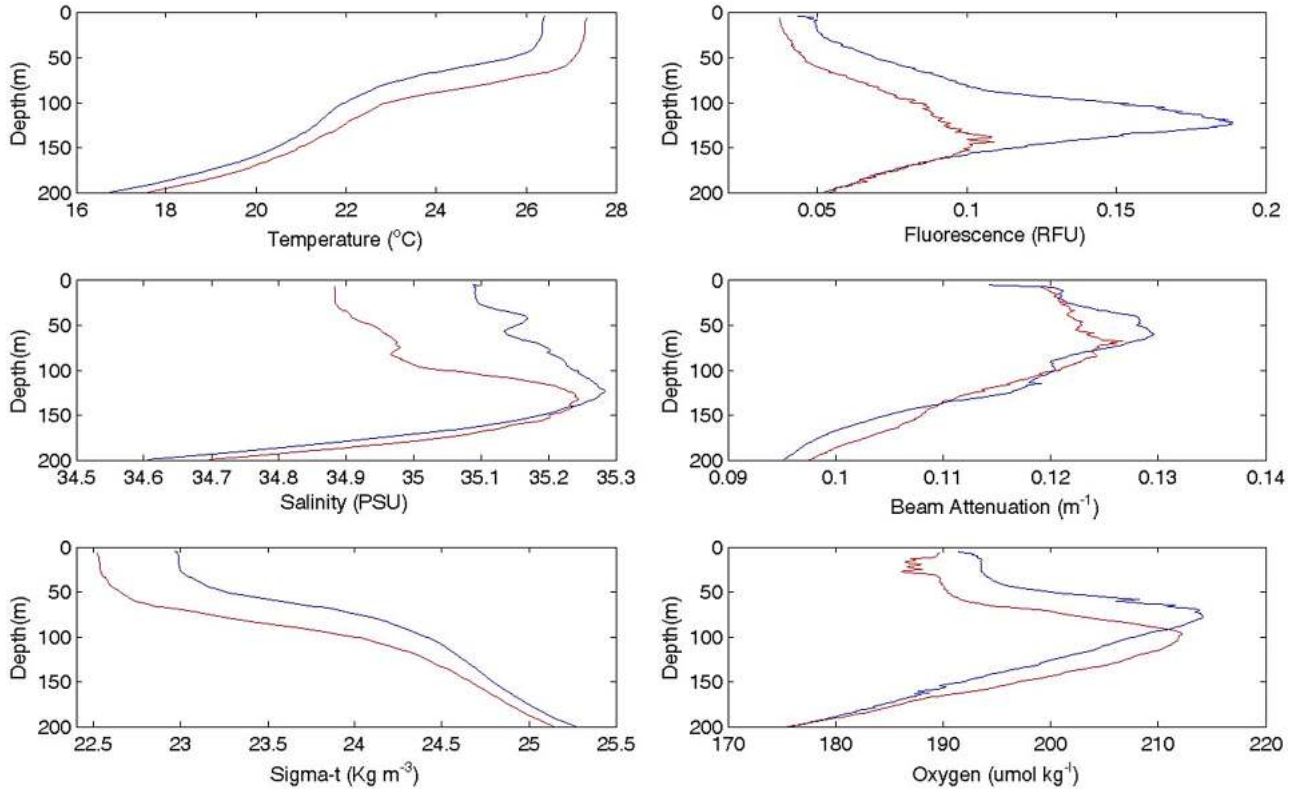

Figure 24. Average vertical profile data (0–200 m, from R/V *Kilo Moana* CTD) for the periods of YD 242–250 in blue and YD 253–258 in red for the following variables: (left) temperature, salinity, density (sigma-t) and (right) chlorophyll fluorescence, beam attenuation coefficient, and dissolved oxygen.

and inherent optical properties as well as phase functions. In particular, they utilized their radiance data sets to compute several irradiances (i.e., upward and downward vector and scalar irradiances). These quantities were further used by *Lewis et al.* [2011] to determine other optically important quantities such as diffuse attenuation coefficients. Importantly, they have demonstrated good agreement between their data sets and those obtained independently by other RaDyO investigators. *Bhandari et al.* [2011] deployed a new camera system called the downwelling polarized radiance distribution camera system (DPOL) from R/P *FLIP* in both the Santa Barbara Channel and off Hawaii during RaDyO. The system, which utilizes a combination of four separate images simultaneously to measure the Stokes vector, measured the downwelling hemisphere of polarized radiance distribution at seven wavelengths in the visible. This distribution is valuable in that it provides the most complete light field description. *Bhandari et al.* [2011] determined that under clear sky conditions, the major source of polarization is refracted skylight close to the sea surface whereas deeper in the water column polarization due to light scattering both increases with depth and dominates.

[117] An important theme of RaDyO concerned under water imaging, which was addressed by *Chang and Twardowski* [2011]. They have computed a key quantity relevant to underwater electro-optical imaging systems called the modulation transfer function (MTF). The MTF is defined as the Fourier transform of the optical point spread function (PSF). The PSF is defined and discussed in detail by *Voss* [1991] who describes it in physical terminology as the image of an unresolved cosine source obtained from a camera and a point source at opposing positions. He indicates that if were there no scattering particles in the medium, the PSF would be a δ-function; however, with scattering the image is blurred. Here, *Chang and Twardowski* [2011] report that imaging parameters were correlated with the characteristics of particle compositions. They also found that optical properties, which were measured in shallow near coastal waters (eutrophic) and deeper offshore (mesotrophic) coastal waters during RaDyO, were strongly affected by atmospheric forcing conditions.

[118] *Moline et al.* [2012] utilized autonomous underwater vehicles (AUVs) to map physical and optical water variability during RaDyO in the Santa Barbara Channel (SBC) and in the open ocean off Hawaii. Their measurements allow data collection at scales and depths unattainable from conventional satellite and aircraft remote sensors. Data collected from a radiometer mounted on an AUV during both field experiments were used to characterize optical constituents by applying bio-optical inversion algorithms. Their results were in good agreement with independent data sets for quantities such as optical absorption.

5.2. RaDyO Modeling Papers

[119] *Carvalho et al.* [2012] and *Dong et al.* [2012] applied atmospheric and oceanic models, respectively, to better define and characterize the SBC atmospheric forcing and oceanic responses for the period of the RaDyO experiment. In this section, *Dong et al.* [2012] applied an automated eddy detection scheme to a 12 year, 3-dimensional

high-resolution numerical oceanic model product. They found a significant percentage of submesoscale eddies, which tended to be ageostrophic, were generated around the islands and headlands along the coastline. Three types of submesoscale eddies were defined on the basis of shape. The eddy fields characterized in this study are valuable for interpreting optical data sets collected during RaDyO in the SBC.

[120] The next three papers concern the challenging problem of simulating radiative transfer across the rapidly changing and complex air-sea interface and within the dynamic and turbulent upper ocean. *Xu et al.* [2012] performed numerical simulations of radiative transfer of natural light in turbulent flows in the upper ocean. They posed the problem for turbulent shear flow which interacted with the sea surface both with and without surface waves. The physical large-eddy simulations were done for fluid motions and transports of temperature and salinity. Inherent optical property (IOP) variability was based on turbulent salinity and temperature fields. They found that the vertical profile of the downward irradiance is governed primarily by the IOP vertical structure with the horizontal variations being attributed to the turbulence. With surface waves, irradiance variability is enhanced via surface deformations caused by wave-turbulence interactions. In a related paper, *Xu et al.* [2011] report on patterns and statistics of light polarization in the water for realistic linear and nonlinear ocean surface wave conditions. Direct simulations of linear and nonlinear surface waves using a higher-order spectral method set the physical conditions for the radiative transfer model, which utilizes a Monte Carlo vector radiative transfer simulation. The authors found (1) that increased roughness of the surface leads to smaller degrees of polarization within Snell's window, (2) variability of the degree of polarization depends strongly upon surface roughness, and (3) nonlinearity of surface waves primarily affects variability of in-water polarizations. They have validated their results using RaDyO data sets collected during the Hawaiian experiment.

[121] The final modeling paper by *You et al.* [2011] also examines polarized light fields under the dynamic ocean surface. These authors developed a hybrid numerical model to efficiently compute and simulate polarized underwater light fields by combining the advantages of 3-dimensional Monte Carlo and matrix operator methods. This model is optimized for the dynamic atmosphere-surface-ocean system in which the temporal variations are limited to the surface while the atmosphere and ocean can be largely considered as static within the time frame of interest. This enables the authors to use a static Monte Carlo model for the computationally intensive radiative transfer calculations in the atmosphere and ocean. These calculations need to be done only once. On the other hand, the interaction between the light fields and the ocean surface is highly dynamic and has to be calculated for each time instance. This interaction is governed by the Fresnel formulae and is rather straightforward. The static and dynamic parts of the system are then coupled using a matrix operator method. The model uses data sets (i.e., optical properties and surface wave slopes) collected during the RaDyO field experiments. Model simulation results for radiance and polarization fields were found to be qualitatively consistent with their observed counterparts. The authors suggest that quantitative agreement would be expected for colocated and synchronized wave-slope and optical property measurements. It is also implied that, given appropriate input data sets, model simulations might be more capable of providing a complete set of spatial, temporal distributions as well as polarization states of the underwater light field comparable with most advanced measuring techniques.

5.3. Other Papers Relevant to the Theme of This Special Section

[122] The final group of papers were not based on the RaDyO program, but have relevance to the section theme. The first two by *Salisbury et al.* [2011] and *Gallegos et al.* [2011] focus on regional studies of optical variability in the upper ocean in the outflow region of the Amazon River (western tropical Atlantic) and Chesapeake Bay, respectively. The last paper by *Szeto et al.* [2011] considers optical differences among four separate ocean basins: the Atlantic, Pacific, Indian, and Southern Oceans. All of these contributions have utilized both satellite remote sensing and in situ observations.

[123] *Salisbury et al.* [2011] documented coherences in space and time of physical and optical properties both within and adjacent to the Amazon River Plume. They report freshened, colored waters coming from the Amazon River with general coherence of salinity and colored dissolved matter absorption (acdm). However, they note spatial patterns of these two parameters which are not overlapping. Following the river plume's trajectory, they observed an inverse relationship between salinity and acdm, suggesting departure from conservative mixing for all observed seasons. Processes contributing to this departure, according to the authors, include areas of enhanced net primary productivity; they suggest the importance of phytoplankton biomass or its remineralization as contributors to the colored dissolved matter (cdm) signal. They also indicate that photo-oxidation of cdm may be important on longer time scales (days to weeks).

[124] *Gallegos et al.* [2011] have utilized a long time series (~25 years) of optical data collected in Chesapeake Bay to examine long-term changes in light scattering in that body of water. Their data sets come from in situ Secchi disk and light attenuation records and remote sensing ocean color satellites. They applied a bio-optical model to these data sets to determine the causes of observed trends in quantities including the Secchi depth, Z_{SD}, and the diffuse attenuation coefficient of photosynthetically active radiation (K_d(PAR)) as well as the product of the two. Their model results suggest a possible cause of decreasing backscatter ratio to be increasing proportions of organic detritus in the Bay. However, the authors also indicate that increasing occurrences of large particle aggregation would be consistent with their model results.

[125] The last paper considers why the world's oceans display significant optical differences. *Szeto et al.* [2011] have examined a large volume of ocean color data collected in situ and assembled by NASA's Ocean Biology Processing Group [*Werdell and Bailey*, 2005]. The work was stimulated by biases that appeared in the SeaWiFS chlorophyll algorithm from ocean to ocean. The authors were able to rule out instrumentation and analytical causes (i.e., artifacts) of the distinctions found among the Atlantic,

Pacific, Indian, and Southern Ocean data sets. The biases are suggested to be attributable to regional differences in absorption properties of detrital matter and phytoplankton. Broader implications concerning the applications of ocean color algorithms to regions are discussed in the authors' conclusions.

[126] **Acknowledgments.** We would like to thank the captains and crews of the R/V *Kilo Moana* and the R/P *FLIP* for their support of our RaDyO field operations in the Santa Barbara Channel and south of Hawaii. Marine technicians Elly Speicher and Dan Fitzgerald provided invaluable support for the R/V *Kilo Moana* operations. Eric Firing and Julia Hummon are thanked for their expert support of the R/V *Kilo Moana* ADCP systems for both field experiments. T. Dickey wishes to thank Steve Ackleson and Joan Cleveland for supporting the Radiance in a Dynamic Ocean (RaDyO) program. T. Dickey also acknowledges support from ONR RaDyO contract N00014-07-1-0732 and grant N000140811178 for his ONR Secretary of the Navy/Chief of Naval Operations Chair in Oceanographic Sciences for Francesco Nencioli, Songnian Jiang, Derek Manov, Jennifer Sirak, and himself. Helen Czerski and David Farmer were supported by ONR grant N00014-06-1-0072. Ken Melville and collaborators were supported by ONR grant N00014-06-1-0048. Dariusz Stramski and collaborators were supported by ONR grants N00014-06-1-0071 and N00014-11-1-0038. The research of the Jet Propulsion Laboratory coauthors was carried out, in part, under contract with the National Aeronautics and Space Administration.

References

Anderson, C. R., M. A. Brzezinski, L. Washburn, and R. Kudela (2006), Circulation and environmental conditions during toxigenic Pseudo-nitzschia australis bloom in the Santa Barbara Channel, California, *Mar. Ecol. Prog. Ser.*, *327*, 119–133, doi:10.3354/meps327119.

Anderson, C. R., D. A. Siegel, M. A. Brzezinski, and N. Guillocheau (2008), Controls on temporal patterns in phytoplankton community structure in the Santa Barbara Channel, California, *J. Geophys. Res.*, *113*, C04038, doi:10.1029/2007JC004321.

Bassin, C. J., L. Washburn, M. Brzezinski, and E. McPhee-Shaw (2005), Sub-mesoscale coastal eddies observed by high frequency radar: A new mechanism for delivering nutrients to kelp forests in the Southern California Bight, *Geophys. Res. Lett.*, *32*, L12604, doi:10.1029/2005GL023017.

Beckenbach, E. H., and L. Washburn (2004), Low frequency waves in the Santa Barbara Channel observed by high frequency radar, *J. Geophys. Res.*, *109*, C02010, doi:10.1029/2003JC001999.

Berry, D. I., and E. C. Kent (2009), A new air-sea interaction gridded dataset from ICOADS with uncertainty estimates, *Bull. Am. Meteorol. Soc.*, *90*(5), 645–656, doi:10.1175/2008BAMS2639.1.

Bhandari, P., K. J. Voss, L. Logan, and M. Twardowski (2011), The variation of the polarized downwelling radiance distribution with depth in the coastal and clear ocean, *J. Geophys. Res.*, *116*, C00H10, doi:10.1029/2011JC007320.

Bird, J. C., R. de Ruiter, L. Courbin, and H. A. Stone (2010), Daughter bubble cascades produced by folding of ruptured thin films, *Nature*, *465*, 759–762, doi:10.1038/nature09069.

Bronson, E. D. (1971), Deep anchoring FLIP, *Mar. Technol. Soc. J.*, *5*(3), 42–44.

Brooks, I. M. et al. (2009), Physical exchanges at the air-sea interface, *Bull. Am. Meteorol. Soc.*, *90*(5), 629–644, doi:10.1175/2008BAMS2578.1.

Carvalho, L. M. V., C. Jones, T. Dickey, C. J. Zappa, Y. Chao, and J. Farrara (2012), Regional and large-scale meteorological conditions during the Radiance in a Dynamic Ocean (RaDyO) Santa Barbara Field Experiment, *Rep. 1*, Santa Barbara Atmos. Sci. Res. Group, Earth Res. Inst., Univ. of Calif., Santa Barbara.

Chang, G., and M. S. Twardowski (2011), Effects of physical forcing and particle characteristics on underwater imaging performance, *J. Geophys. Res.*, *116*, C00H03, doi:10.1029/2011JC007098.

Czerski, H., M. Twardowski, X. Zhang, and S. Vagle (2011), Resolving size distributions of bubbles with radii less than 30 μm with optical and acoustical methods, *J. Geophys. Res.*, *116*, C00H11, doi:10.1029/2011JC007177.

Darecki, M., D. Stramski, and M. Sokolski (2011), Measurements of high-frequency light fluctuations induced by sea surface waves with an Underwater Porcupine Radiometer System, *J. Geophys. Res.*, *116*, C00H09, doi:10.1029/2011JC007338.

Davies-Colley, R. J. (1988), Measuring water clarity with a black disk, *Limnol. Oceanogr.*, *33*, 616–623, doi:10.4319/lo.1988.33.4.0616.

Dera, J. (1992), *Marine Physics*, 516 pp., Elsevier, Amsterdam.

Dera, J., and H. R. Gordon (1968), Light field fluctuations in the photic zone, *Limnol. Oceanogr.*, *13*, 697–699, doi:10.4319/lo.1968.13.4.0697.

Dera, J., and J. Olszewski (1967), On the natural irradiance fluctuations affecting photosynthesis in the sea, *Acta Geophys. Pol.*, *15*, 351–364.

Dera, J., and J. Olszewski (1978), Experimental study of short-period irradiance fluctuations under an undulated sea surface, *Oceanologia*, *10*, 27–49.

Dera, J., and D. Stramski (1986), Maximum effects of sunlight focusing under a wind-disturbed sea surface, *Oceanologia*, *23*, 15–42.

Dera, J. S. S., and D. Stramski (1993), Focusing of sunlight by sea surface waves: New results from the Black Sea, *Oceanologia*, *34*, 13–25.

Dickey, T. (1991), The emergence of concurrent high resolution physical and bio-optical measurements in the upper ocean and their applications, *Rev. Geophys.*, *29*, 383–413, doi:10.1029/91RG00578.

Dickey, T. D., and R. R. Bidigare (2005), Interdisciplinary oceanographic observations: The wave of the future, *Sci. Mar.*, *69*, Suppl. 1, 23–42.

Dickey, T. D., M. R. Lewis, and G. C. Chang (2006), Optical oceanography: Recent advances and future directions using global remote sensing and in situ observations, *Rev. Geophys.*, *44*, RG1001, doi:10.1029/2003RG000148.

Dickey, T. D., F. Nencioli, V. S. Kuwahara, C. Leonard, W. Black, Y. M. Rii, R. R. Bidigare, and Q. Zhang (2008), Physical and bio-optical observations of oceanic cyclones west of the island of Hawai'i, *Deep Sea Res., Part II*, *55*, 1195–1217, doi:10.1016/j.dsr2.2008.01.006.

Dickey, T., G. Kattawar, and K. Voss (2011), Shedding new light on light in the ocean, *Phys. Today*, *64*(4), 44–50.

DiGiacomo, P., and B. Holt (2001), Satellite observations of small coastal ocean eddies in the Southern California Bight, *J. Geophys. Res.*, *106*(C10), 22,521–22,543, doi:10.1029/2000JC000728.

DiGiacomo, P. M., L. Washburn, B. Holt, and B. H. Jones (2004), Coastal pollution hazards in Southern California observed by SAR imagery: Storm water plumes, wastewater plumes, and natural hydrocarbon seeps, *Mar. Pollut. Bull.*, *49*, 1013–1024, doi:10.1016/j.marpolbul.2004.07.016.

Dolin, L. S., and A. G. Luchinin (2008), Water-scattered signal to compensate for the rough sea surface effect on bottom lidar imaging, *Appl. Opt.*, *47*, 6871–6878, doi:10.1364/AO.47.006871.

Dolin, L., G. Gilbert, I. Levin, and A. Luchinin (2006), *Theory of Imaging Through Wavy Sea Surface*, 171 pp., Russian Acad. Sci. Inst. Appl. Phys., Nizhniy Novgorod, Russia.

Dong, C., X. Lin, Y. Liu, F. Nencioli, Y. Chao, Y. Guan, D. Chen, T. Dickey, and J. C. McWilliams (2012), Three-dimensional ocean eddy analysis in the Southern California Bight from a numerical product, *J. Geophys. Res.*, *117*, C00H14, doi:10.1029/2011JC007354.

Dorman, C. E., and C. D. Winant (1995), Buoy observations of the atmosphere along the west coast of the United States, 1981–1990, *J. Geophys. Res.*, *100*(C8), 16,029–16,044, doi:10.1029/95JC00964.

Dorman, C. E., and C. D. Winant (2000), The structure and variability of the marine atmosphere around the Santa Barbara Channel, *Mon. Weather Rev.*, *128*, 261–282, doi:10.1175/1520-0493(2000)128<0261:TSAVOT>2.0.CO;2.

Dorman, C. E., D. P. Rogers, W. Nuss, and W. T. Thompson (1999), Adjustment of the summer marine boundary layer around Pt. Sur, California, *Mon. Weather Rev.*, *127*, 2143–2159, doi:10.1175/1520-0493(1999)127<2143:AOTSMB>2.0.CO;2.

Doron, M., M. Babin, A. Mangin, and O. Hembie (2007), Estimation of light penetration, and horizontal and vertical visibility in oceanic and coastal waters from surface reflectance, *J. Geophys. Res.*, *112*, C06003, doi:10.1029/2006JC004007.

Duntley, S. Q. (1963), Light in the sea, *J. Opt. Soc. Am.*, *53*, 214–233, doi:10.1364/JOSA.53.000214.

Emery, B. M., L. Washburn, and J. A. Harlan (2004), Evaluating radial current measurements from CODAR high-frequency radars with moored current meters, *J. Atmos. Oceanic Technol.*, *21*(8), 1259–1271, doi:10.1175/1520-0426(2004)021<1259:ERCMFC>2.0.CO;2.

Farmer, D. M., S. Vagle, and A. D. Booth (1998), A free flooding acoustical resonator for measurement of bubble size distributions, *J. Atmos. Oceanic Technol.*, *15*, 1132–1146, doi:10.1175/1520-0426(1998)015<1132:AFFARF>2.0.CO;2.

Fisher, F. H., and F. N. Spiess (1963), FLIP–Floating Instrument Platform, *J. Acoust. Soc. Am.*, *35*, 1633–1644, doi:10.1121/1.1918772.

Fraser, A. B., R. E. Walker, and F. C. Jurgens (1980), Spatial and temporal correlation of underwater sunlight fluctuations in the sea, *IEEE J. Oceanic Eng.*, *5*, 195–198, doi:10.1109/JOE.1980.1145467.

Frechette, M., and L. Legendre (1978), Phytoplankton photosynthesis: Response to a simplified stimulus, modeling rapid light fluctuations induced by sea surface waves, *J. Exp. Mar. Biol. Ecol.*, *32*, 15–25.

Friehe, C. A., J. A. Smith, K. F. Rieder, N. E. Huang, J.-P. Giovanangeli, and G. L. Geernaert (2001), Wind, stress and wave directions, in *Wind Stress Over the Ocean*, edited by I. S. F. Jones and Y. Toba,

pp. 232–241, Cambridge Univ. Press, Cambridge, U. K., doi:10.1017/CBO9780511552076.013.

Gallegos, C. L., P. J. Werdell, and C. R. McClain (2011), Long-term changes in light scattering in Chesapeake Bay inferred from Secchi depth, light attenuation, and remote sensing measurements, *J. Geophys. Res.*, *116*, C00H08, doi:10.1029/2011JC007160.

Gernez, P., and D. Antoine (2009), Field characterization of wave-induced underwater light field fluctuations, *J. Geophys. Res.*, *114*, C06025, doi:10.1029/2008JC005059.

Gernez, P., D. Stramski, and M. Darecki (2011), Vertical changes in the probability distribution of downward irradiance within the near-surface ocean under sunny conditions, *J. Geophys. Res.*, *116*, C00H07, doi:10.1029/2011JC007156.

Harms, S., and C. D. Winant (1998), Characteristic patterns of the circulation in the Santa Barbara Channel, *J. Geophys. Res.*, *103*, 3041–3065, doi:10.1029/97JC02393.

Hellerman, S., and M. Rosenstein (1983), Normal monthly wind stress over the world ocean with error estimates, *J. Phys. Oceanogr.*, *13*, 1093–1104, doi:10.1175/1520-0485(1983)013<1093:NMWSOT>2.0.CO;2.

Jaffe, J. S., K. D. Moore, J. McLean, and M. P. Strand (2001), Underwater optical imaging: Status and prospects, *Oceanography*, *14*(3), 64–75, doi:10.5670/oceanog.2001.24.

Janzen, C., N. Larson, and C. Moore (2008), WQM: New instrumentation for coastal monitoring, *Sea Technol.*, *49*(2), 55–58.

Kattawar, G. W., and C. N. Adams (1989), Stokes vector calculations of the submarine light field in an atmosphere–ocean with scattering according to a Rayleigh phase matrix: Effect of interface refractive index on radiance and polarization, *Limnol. Oceanogr.*, *34*, 1453–1472, doi:10.4319/lo.1989.34.8.1453.

Kattawar, G. W., T. J. Humphreys, and G. N. Plass (1976), Radiative transfer in an atmosphere–ocean system: A matrix operator approach, *Proc. SPIE Int. Soc. Opt. Eng.*, *160*, 123–131.

Kessler, R. C., and S. G. Douglas (1991), Numerical study of mesoscale eddy development over the Santa Barbara Channel, *J. Appl. Meteorol.*, *30*, 633–651, doi:10.1175/1520-0450(1991)030<0633:ANSOME>2.0.CO;2.

Kirk, J. T. O. (1994), *Light and Photosynthesis in Aquatic Ecosystems*, 2nd ed., 509 pp., Cambridge Univ. Press, Cambridge, U. K., doi:10.1017/CBO9780511623370.

Kostadinov, T. S., D. A. Siegel, S. Maritorena, and N. Guillocheau (2007), Ocean color observations and modeling for an optically complex site: Santa Barbara Channel, California, USA, *J. Geophys. Res.*, *112*, C07011, doi:10.1029/2006JC003526.

Legendre, L., M. Rochet, and S. Demers (1986), Sea-ice microalgae to test the hypothesis of photosynthetic adaptation to high frequency light fluctuations, *J. Exp. Mar. Biol. Ecol.*, *97*, 321–326, doi:10.1016/0022-0981(86)90250-9.

Levin, I. M., V. V. Savchenko, and V. Y. Osadchy (2008), Correction of an image distorted by a wavy water surface: Laboratory experiment, *Appl. Opt.*, *47*, 6650–6655, doi:10.1364/AO.47.006650.

Lewis, M. R. (2008), Measurement of apparent optical properties for diagnosis of harmful algal blooms, in *Real-time Coastal Observing System Dynamics and Harmful Algal Blooms*, edited by M. Babin, C. S. Roesler, and J. J. Cullen, pp. 207–236, UNESCO Publ., Paris.

Lewis, M. R., J. Wei, R. Van Dommelen, and K. J. Voss (2011), Quantitative estimation of the underwater radiance distribution, *J. Geophys. Res.*, *116*, C00H06, doi:10.1029/2011JC007275.

MacIntyre, F. (1972), Flow patterns in breaking bubbles, *J. Geophys. Res.*, *77*, 5211–5228, doi:10.1029/JC077i027p05211.

McFarland, W., and E. Loew (1983), Wave produced changes in underwater light and their relations to vision, *Environ. Biol. Fishes*, *8*, 173–184, doi:10.1007/BF00001083.

McLean, J. W., and J. D. Freeman (1996), Effects of ocean waves on airborne lidar imaging, *Appl. Opt.*, *35*, 3261–3269, doi:10.1364/AO.35.003261.

Mobley, C. D. (1994), *Light and Water: Radiative Transfer in Natural Waters*, 592 pp., Academic, San Diego, Calif.

Moline, M. A., S. M. Blackwell, C. Von Alt, B. Allen, T. Austin, J. Case, N. Forrester, R. Goldsborough, M. Purcell, and R. Stokey (2005), Remote environmental monitoring units: An autonomous vehicle for characterizing coastal environments, *J. Atmos. Oceanic Technol.*, *22*, 1797–1808, doi:10.1175/JTECH1809.1.

Moline, M. A., D. L. Woodruff, and N. R. Evans (2007), Optical delineation of benthic habitat using an autonomous underwater vehicle, *J. Field Rob.*, *24*(6), 461–471, doi:10.1002/rob.20176.

Moline, M. A., K. J. Benoit-Bird, I. C. Robbins, M. Schroth-Miller, C. M. Waluk, and B. Zelenke (2010), Integrated measurements of acoustical and optical thin layers II: Horizontal length scales, *Cont. Shelf Res.*, *30*(1), 29–38, doi:10.1016/j.csr.2009.08.004.

Moline, M. A., I. Robbins, B. Zelenke, W. S. Pegau, and H. Wijesekera (2012), Evaluation of bio-optical inversion of spectral irradiance measured from an autonomous underwater vehicle, *J. Geophys. Res.*, *117*, C00H15, doi:10.1029/2011JC007352.

Mullamaa, Y.-A. R. (1975), Influence of a disturbed ocean surface on the visibility of underwater object, *Izv. Russ. Acad. Sci. Atmos. Oceanic Phys., Engl. Transl.*, *11*, 199–206.

Munk, W. H. (1950), On the wind-driven ocean circulation, *J. Meteorol.*, *7*(2), 80–93, doi:10.1175/1520-0469(1950)007<0080:OTWDOC>2.0.CO;2.

Nencioli, F., C. Dong, T. Dickey, L. Washburn, and J. C. McWilliams (2010), A vector geometry based eddy detection algorithm and its application to a high resolution numerical model product and high-frequency radar surface velocities in the Southern California Bight, *J. Atmos. Oceanic Technol.*, *27*(3), 564–579, doi:10.1175/2009JTECHO725.1.

Nishimoto, M. M., and L. Washburn (2002), Patterns of coastal eddy circulation and abundance of pelagic juvenile fish in the Santa Barbara Channel, California, USA, *Mar. Ecol. Prog. Ser.*, *241*, 183–199, doi:10.3354/meps241183.

Pinkel, R., J. Sherman, J. Smith, and S. Anderson (1991), Strain: Observations of the vertical gradient of isopycnal vertical displacement, *J. Phys. Oceanogr.*, *21*, 527–540, doi:10.1175/1520-0485(1991)021<0527:SOOTVG>2.0.CO;2.

Plueddemann, A. J., J. A. Smith, D. M. Farmer, R. A. Weller, W. R. Crawford, R. Pinkel, S. Vagle, and A. Gnanadesikan (1996), Structure and variability of Langmuir circulation during the Surface Waves Processes Program, *J. Geophys. Res.*, *101*, 3525–3543, doi:10.1029/95JC03282.

Preisendorfer, R. W. (1976), *Hydrologic Optics*, vol. 1, NOAA, Silver Spring, Md.

Queguiner, B., and L. Legendre (1986), Phytoplankton photosynthetic adaptation to high frequency light fluctuations induced by sea-surface waves, *Mar. Biol. Berlin*, *90*, 483–491, doi:10.1007/BF00409268.

Rainville, L., and R. Pinkel (2006), Baroclinic energy flux at the Hawaiian Ridge: Observations from the R/P *FLIP*, *J. Phys. Oceanogr.*, *36*, 1104–1122, doi:10.1175/JPO2882.1.

Reineman, B. D., L. Lenain, D. Castel, and W. K. Melville (2009), Portable airborne scanning lidar system for ocean and coastal applications, *J. Atmos. Oceanic Technol.*, *26*(12), 2626–2641, doi:10.1175/2009JTECHO703.1.

Robbins, I. C., G. J. Kirkpatrick, S. M. Blackwell, J. Hillier, C. A. Knight, and M. A. Moline (2006), Improved monitoring of HABs using autonomous underwater vehicles (AUV), *Harmful Algae*, *6*(6), 931–943, doi:10.1016/j.hal.2006.03.005.

Rudnick, P. (1967), Motion of a large spar buoy in sea waves, *J. Ship Res.*, *11*(4), 257–267.

Rudnick, P., and R. W. Hasse (1971), Extreme Pacific waves, December 1969, *J. Geophys. Res.*, *76*(3), 742–744, doi:10.1029/JC076i003p00742.

Salisbury, J., D. Vandemark, J. Campbell, C. Hunt, D. Wisser, N. Reul, and B. Chapron (2011), Spatial and temporal coherence between Amazon River discharge, salinity, and light absorption by colored organic carbon in western tropical Atlantic surface waters, *J. Geophys. Res.*, *116*, C00H02, doi:10.1029/2011JC006989.

Schenck, H. (1957), On the focusing of sunlight by ocean waves, *J. Opt. Soc. Am.*, *47*, 653–657, doi:10.1364/JOSA.47.000653.

Schippnick, P. F. (1988), Imaging of a bottom object through a wavy air-water interface, *Proc. SPIE Int. Soc. Opt. Eng.*, *925*, 371–382.

Shifrin, K. S. (1988), *Physical Optics of Ocean Water*, 285 pp., Am. Insti. of Phys., New York.

Siegel, D. A., and T. D. Dickey (1986), Variability of net longwave radiation over the eastern North Pacific Ocean, *J. Geophys. Res.*, *91*, 7657–7666, doi:10.1029/JC091iC06p07657.

Siegel, D. A., and T. D. Dickey (1987), Observations of the vertical structure of the diffuse attenuation coefficient spectrum, *Deep Sea Res.*, *34*, 547–563, doi:10.1016/0198-0149(87)90005-7.

Siegel, E., and A. Lohrmann (2010), Eliminating the blanking distance for acoustic Doppler current profilers, *Sea Technol.*, *51*(2), 33–36.

Skyllingstad, E. D., P. Barbour, and C. E. Dorman (2001), The dynamics of northwest summer winds over the Santa Barbara Channel, *Mon. Weather Rev.*, *129*, 1042–1061, doi:10.1175/1520-0493(2001)129<1042:TDONSW>2.0.CO;2.

Smith, J. A. (1998), Evolution of Langmuir circulation during a storm, *J. Geophys. Res.*, *103*, 12,649–12,668, doi:10.1029/97JC03611.

Smith, J. A., and K. F. Rieder (1997), Wave-induced motion of FLIP, *Ocean Eng.*, *24*, 95–110, doi:10.1016/0029-8018(96)00008-X.

Smith, J. A., R. Pinkel, and R. Weller (1987), Velocity structure in the mixed layer during MILDEX, *J. Phys. Oceanogr.*, *17*, 425–439, doi:10.1175/1520-0485(1987)017<0425:VSITML>2.0.CO;2.

Snyder, R. L., and J. Dera (1970), Wave-induced light-field fluctuations in the sea, *J. Opt. Soc. Am.*, *60*, 1072–1079, doi:10.1364/JOSA.60.001072.

Stramska, M., and T. Dickey (1998), Short-term variability of the underwater light field in the oligotrophic ocean in response to surface waves and clouds, *Deep Sea Res., Part I*, *45*, 1393–1410, doi:10.1016/S0967-0637(98)00020-X.

Stramski, D. (1986), Fluctuations of solar irradiance induced by surface waves in the Baltic, *Bull. Pol. Acad. Sci. Earth Sci.*, *34*, 333–344.

Stramski, D. (1994), Gas microbubbles: An assessment of their significance to light scattering in quiescent seas, *Proc. SPIE Int. Soc. Opt. Eng.*, *2258*, 704–710.

Stramski, D., and J. Dera (1988), On the mechanism for producing flashing light under a wind-disturbed water surface, *Oceanologia*, *25*, 5–21.

Stramski, D., and J. Tegowski (2001), Effects of intermittent entrainment of air bubbles by breaking wind waves on ocean reflectance and underwater light field, *J. Geophys. Res.*, *106*, 31,345–31,360, doi:10.1029/2000JC000461.

Stramski, D., C. R. Booth, and B. G. Mitchell (1992), Estimation of downward irradiance from a single moored instrument, *Deep Sea Res., Part A*, *39*, 567–584, doi:10.1016/0198-0149(92)90089-C.

Stramski, D., G. Rosenberg, and L. Legendre (1993), Photosynthetic and optical properties of the marine chlorophyte *Dunaliella tertiolecta* grown under fluctuating light caused by surface-wave focusing, *Mar. Biol. Berlin*, *115*, 363–372, doi:10.1007/BF00349833.

Sullivan, J. M., M. S. Twardowski, P. L. Donaghay, and S. A. Freeman (2005), Using scattering characteristics to discriminate particle types in U.S. coastal waters, *Appl. Opt.*, *44*, 1667–1680, doi:10.1364/AO.44.001667.

Szeto, M., P. J. Werdell, T. S. Moore, and J. W. Campbell (2011), Are the world's oceans optically different?, *J. Geophys. Res.*, *116*, C00H04, doi:10.1029/2011JC007230.

Terrill, E., and M. Lewis (2004), Tiny bubbles: An overlooked optical constituent, *Oceanography*, *17*(2), 11, doi:10.5670/oceanog.2004.41.

Terrill, E., W. K. Melville, and D. Stramski (2001), Bubble entrainment by breaking waves and their influence on optical scattering in the upper ocean, *J. Geophys. Res.*, *106*, 16,815–16,823, doi:10.1029/2000JC000496.

Thomas, G. E., and K. Stamnes (1999), *Radiative Transfer in the Atmosphere and Ocean*, 517 pp., Cambridge Univ. Press, Cambridge, U. K., doi:10.1017/CBO9780511613470.

Thorpe, S. (1982), On the clouds of bubbles formed by breaking wind waves in deep water and their role in air-sea gas transfer, *Philos. Trans. R. Soc. London, Ser. A*, *304*, 155–210, doi:10.1098/rsta.1982.0011.

Toole, D. A., and D. A. Siegel (2001), Modes and mechanisms of ocean color variability in the Santa Barbara Channel, *J. Geophys. Res.*, *106*, 26,985–27,000, doi:10.1029/2000JC000371.

Twardowski, M. S., J. M. Sullivan, P. L. Donaghay, and J. R. V. Zaneveld (1999), Microscale quantification of the absorption by dissolved and particulate material in coastal waters with an ac-9, *J. Atmos. Oceanic Technol.*, *16*(6), 691–707, doi:10.1175/1520-0426(1999)016<0691:MQOTAB>2.0.CO;2.

Twardowski, M. S., M. Lewis, A. Barnard, and J. R. V. Zaneveld (2007a), In-water instrumentation and platforms for ocean color remote sensing applications, in *Remote Sensing of Coastal Aquatic Waters*, edited by R. Miller, C. Del Castillo, and B. McKee, pp. 69–100, Springer Publ., Dordrecht, Netherlands, doi:10.1007/978-1-4020-3100-7_4.

Twardowski, M. S., H. Claustre, S. A. Freeman, D. Stramski, and Y. Huot (2007b), Optical backscattering properties of the "clearest" natural waters, *Biogeosciences*, *4*, 1041–1058, doi:10.5194/bg-4-1041-2007.

Twardowski, M., X. Zhang, S. Vagle, J. Sullivan, S. Freeman, H. Czerski, Y. You, L. Bi, and G. Kattawar (2012), The optical volume scattering function in a surf zone inverted to derive sediment and bubble particle subpopulations, *J. Geophys. Res.*, *117*, C00H17, doi:10.1029/2011JC007347.

Vagle, S., J. Gemmrich, and H. Czerski (2012), Reduced upper ocean turbulence and changes to bubble size distributions during large downward heat-flux events, *J. Geophys. Res.*, *117*, C00H16, doi:10.1029/2011JC007308.

Voss, K. J. (1991), Simple empirical model of the oceanic spread function, *Appl. Opt.*, *30*, 2647–2651, doi:10.1364/AO.30.002647.

Voss, K. J., and Y. Liu (1997), Polarized radiance distribution measurements of skylight: I. System description and characterization, *Appl. Opt.*, *36*, 6083–6094, doi:10.1364/AO.36.006083.

Walker, R. E. (1994), *Marine Light Field Statistics*, 675 pp., John Wiley, New York.

Walsh, P., and L. Legendre (1983), Photosynthesis of natural phytoplankton under high light fluctuations stimulating those induced by sea surface waves, *Limnol. Oceanogr.*, *28*, 688–697, doi:10.4319/lo.1983.28.4.0688.

Wanninkhof, R. (1992), Relationship between gas exchange and wind speed over the ocean, *J. Geophys. Res.*, *97*, 7373–7382, doi:10.1029/92JC00188.

Wanninkhof, R., and W. R. McGillis (1999), A cubic relationship between CO_2 exchange and wind speed, *Geophys. Res. Lett.*, *26*, 1889–1892, doi:10.1029/1999GL900363.

Wanninkhof, R., K. F. Sullivan, and Z. Top (2004), Air-sea gas transfer in the Southern Ocean, *J. Geophys. Res.*, *109*, C08S19, doi:10.1029/2003JC001767.

Weller, R. A., M. F. Baumgartner, S. A. Josey, A. S. Fischer, and J. C. Kindle (1998), Atmospheric forcing in the Arabian Sea during 1994–1995: Observations and comparisons with climatology and models, *Deep Sea Res., Part II*, *45*(10–11), 1961–1999, doi:10.1016/S0967-0645(98)00060-5.

Werdell, P., and S. Bailey (2005), An improved *in situ* bio-optical data set for ocean color algorithm development and satellite data product validation, *Remote Sens. Environ.*, *98*(1), 122–140, doi:10.1016/J.Rse.2005.07.001.

Wijesekera, H. W., W. S. Pegau, and T. J. Boyd (2005), Effect of surface waves on the irradiance distribution in the upper ocean, *Opt. Express*, *23*, 9264–9267.

Winant, C. D., and C. E. Dorman (1997), Seasonal patterns of surface wind stress and heat flux over the Southern California Bight, *J. Geophys. Res.*, *102*, 5641–5653, doi:10.1029/96JC02801.

Wolk, F., H. Yamazaki, L. Seuront, and R. G. Lueck (2002), A new free-fall profiler for measuring biophysical microstructure, *J. Atmos. Oceanic Technol.*, *19*, 780–793, doi:10.1175/1520-0426(2002)019<0780:ANFFPF>2.0.CO;2.

Woolf, D. K. (1997), Bubbles and their role in gas exchange, in *The Sea Surface and Global Change*, edited by P. S. Liss and R. A. Duce, pp. 173–206, Cambridge Univ. Press, Cambridge, U. K., doi:10.1017/CBO9780511525025.007.

Woolf, D. K. (2005), Parameterization of gas transfer velocities and sea-state dependent wave breaking, *Tellus, Ser. B*, *57*, 87–94, doi:10.1111/j.1600-0889.2005.00139.x.

Wurl, O., L. Miller, R. Roettgers, and S. Vagle (2009), The distribution and fate of surface-active substances in the sea-surface microlayer and water column, *Mar. Chem.*, *115*(1–2), 1–9, doi:10.1016/j.marchem.2009.04.007.

Wurl, O., L. Miller, and S. Vagle (2011), Production and fate of transparent exopolymer particles in the ocean, *J. Geophys. Res.*, *116*, C00H13, doi:10.1029/2011JC007342.

Xu, Z., D. K. P. Yue, L. Shen, and K. J. Voss (2011), Patterns and statistics of in-water polarization under conditions of linear and nonlinear ocean surface waves, *J. Geophys. Res.*, *116*, C00H12, doi:10.1029/2011JC007350.

Xu, Z., X. Guo, L. Shen, and D. K. P. Yue (2012), Radiative transfer in ocean turbulence and its effect on underwater light field, *J. Geophys. Res.*, *117*, C00H18, doi:10.1029/2011JC007351.

You, Y., P.-W. Zhai, G. W. Kattawar, and P. Yang (2009), Polarized radiance fields under a dynamic ocean surface: A three-dimensional radiative transfer solution, *Appl. Opt.*, *48*, 3019–3029, doi:10.1364/AO.48.003019.

You, Y., D. Stramski, M. Darecki, and G. W. Kattawar (2010), Modeling of wave-induced irradiance fluctuations at near-surface depths in the ocean: A comparison with measurements, *Appl. Opt.*, *49*, 1041–1053, doi:10.1364/AO.49.001041.

You, Y., G. W. Kattawar, K. J. Voss, P. Bhandari, J. Wei, M. Lewis, C. J. Zappa, and H. Schultz (2011), Polarized light field under dynamic ocean surfaces: Numerical modeling compared with measurements, *J. Geophys. Res.*, *116*, C00H05, doi:10.1029/2011JC007278.

Yu, L., and R. A. Weller (2007), Objectively analyzed air-sea fluxes for the global ice-free oceans (1981–2005), *Bull. Am. Meteorol. Soc.*, *88*, 527–539, doi:10.1175/BAMS-88-4-527.

Zaneveld, J. R. V., and W. S. Pegau (2003), Robust underwater visibility parameter, *Opt. Express*, *11*(23), 2997–3009, doi:10.1364/OE.11.002997.

Zaneveld, J. R. V., E. Boss, and A. Barnard (2001a), Influence of surface waves on measured and modeled irradiance profiles, *Appl. Opt.*, *40*, 1442–1449, doi:10.1364/AO.40.001442.

Zaneveld, J. R. V., E. Boss, and P. A. Hwang (2001b), The influence of coherent waves on the remotely sensed reflectance, *Opt. Express*, *9*(6), 260–266, doi:10.1364/OE.9.000260.

Zaneveld, J. R. V., M. S. Twardowski, M. Lewis, and A. Barnard (2005), Radiative transfer and remote sensing, in *Remote Sensing of Coastal Aquatic Waters*, edited by R. Miller and C. Del-Castillo, pp. 1–20, Springer-Kluwer Publ., Dordrecth, Netherlands.

Zappa, C. J., M. L. Banner, H. Schultz, A. Corrada-Emmanuel, L. B. Wolff, and J. Yalcin (2008), Retrieval of short ocean wave slope using polarimetric imaging, *Meas. Sci. Technol.*, *19*, 055503, doi:10.1088/0957-0233/19/5/055503.

Zappa, C. J., M. L. Banner, H. Schultz, J. Gemmrich, R. Morison, D. A. LeBel, and T. Dickey (2012), An overview of sea state conditions and air-sea fluxes during RaDyO, *J. Geophys. Res.*, *117*, C00H19, doi:10.1029/2011JC007336.

Zhai, P.-W., G. W. Kattawar, and P. Yang (2008a), Impulse response solution to the three-dimensional vector radiative transfer equation in atmosphere–ocean systems. I. Monte Carlo method, *Appl. Opt.*, *47*, 1037–1047, doi:10.1364/AO.47.001037.

Zhai, P.-W., G. W. Kattawar, and P. Yang (2008b), Impulse response solution to the three-dimensional vector radiative transfer equation in atmosphere–ocean systems. II. The hybrid matrix operator–Monte Carlo method, *Appl. Opt.*, *47*, 1063–1071, doi:10.1364/AO.47.001063.

Zhang, X., M. Lewis, and B. Johnson (1998), Influence of bubbles on scattering of light in the ocean, *Appl. Opt.*, *37*(27), 6525–6536, doi:10.1364/AO.37.006525.

Zhang, X., M. Twardowski, and M. Lewis (2011), Retrieving composition and sizes of oceanic particle subpopulations from the volume scattering function, *Appl. Opt.*, *50*, 1240–1259, doi:10.1364/AO.50.001240.

Zibordi, G., D. d'Alimonte, and J. F. Berthon (2004), An evaluation of depth resolution requirements for optical profiling in coastal waters, *J. Atmos. Oceanic Technol.*, *21*, 1059–1073, doi:10.1175/1520-0426(2004)021<1059:AEODRR>2.0.CO;2.